CENTER FOR
MACHINE PERCEPTION

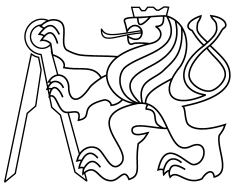

CZECH TECHNICAL
UNIVERSITY IN PRAGUE

PhD THESIS

ISSN 1213-2365

Light Propagation in Transparent Polyhedra

Vladimír Smutný

smutny@cmp.felk.cvut.cz

PhD Thesis CTU–CMP–2014–11

August, 2014

Thesis Advisor: Ing. Tomáš Pajdla, Ph.D.

PhD Program: Electrical Engineering and Information Technology
Branch of Study: Artificial Intelligence and Biocybernetics

.

The author was supported by
The Grant Agency of the CTU Prague under
Project SGS10/193/OHK3/2T/13 and by
The Technology Agency of the Czech Republic under Project
Center for Applied Cybernetics TE01020197.

Research Reports of CMP, Czech Technical University in Prague, No. 11, 2014

Published by

Center for Machine Perception, Department of Cybernetics
Faculty of Electrical Engineering, Czech Technical University in Prague
Technická 2, 166 27 Prague 6, Czech Republic
fax +420 2 2435 7385, phone +420 2 2435 7637, www: http://cmp.felk.cvut.cz

Acknowledgements

I would like to express my special appreciation and thanks to my advisor Dr. Tomáš Pajdla.

Special thanks go to Prof. Václav Hlaváč, founder and head of the Center for Machine Perception both for the atmosphere, support, and last but not least for his suggestions on the thesis manuscript. It was really invaluable.

I would like to thank Prof. Mirko Navara and Dr. Libor Špaček for careful reading and comments on the thesis manuscript as well as all the members of the Center for Machine Perception, that contribute to the warm and productive atmosphere that dominates the CMP environment.

A special thanks go to my wife for her support and all the sacrifices she has made on my behalf. My grateful thanks go to my mother and father for their continuous support, both passed away shortly before I finished my thesis.

Abstrakt

Výroba šperkařských i bižuterních kamenů je významným průmyslem. Tento průmysl se neobejde bez hodnocení kamenů během vývoje jejich tvaru, jejich výroby ale i hotových výrobků. Počítačové vidění je přirozený nástroj pro řešení těchto úkolů.

Šperkové kameny jsou z podstaty své výroby konvexními mnohostěny. Vybroušené kameny jsou většinou z průhledného materiálu, někdy zcela čirého, jindy zabarveného a částečně pohlcujícího procházející světlo.

Práce vychází ze dvou přístupů, které jsem vyvinul v minulých letech. První přístup bere za svůj vstup geometrický model šperkového kamene doplněný o fyzikální vlastnosti, především index lomu materiálu. Počítačový model takového kamene je osvětlen rovnoběžným svazkem světla a počítačovou simulací jsou vypočteny geometrické a radiometrické parametry světelných svazků vystupujících z kamene. Na těchto svazcích jsou pak počítány různé příznaky (charakteristiky) hodnotící kámen nebo je grafické zobrazení vystupujících paprsků hodnoceno člověkem.

Druhý přístup vychází z toho, že výsledky výše uvedené simulace lze porovnat s reálně provedeným experimentem. Rozdíly mezi simulovanými a měřenými výsledky ukazují na rozdíly mezi modelem kamene a jeho skutečným tvarem.

Tato dizertační práce přispívá k oběma těmto přístupům. Na simulační straně úlohy je model doplněn o prostředí pohlcující světlo. Modelované kameny tak mohou být nejen z průhledného nepohlcujícího, čirého materiálu, ale mohou být za dodržení průhlednosti i z barevných, světlo pohlcujících materiálů. Barevné průhledné kameny jsou ve šperkařství i bižuterii běžné a významně se tak rozšiřuje okruh modelovaných kamenů.

Studium optických jevů na oblých hranách kamene zvyšuje věrnost matematického modelu kamene. Kromě toho pomáhá řešit základní problém výše uvedeného druhého přístupu to jest problém korespondence simulovaných a fotografovaných stop světelných svazků. Výsledky jevů na oblých hranách jsou simulovatelné v programech a pozorovatelné na fotografiích, takže umožňují hledat korespondence realisticky složitých kamenů.

Šíření svazku paralelních paprsků kamenem ve tvaru mnohostěnu lze reprezentovat grafem. Struktura grafu se zavedenými atributy dovoluje vyšší stupeň porozumění a zároveň inspiruje při vývoji programů pro simulaci šíření svazků v kameni.

Zcela nová je metoda nasvícení počítačového modelu ze všech stran najednou. Tato metoda odstraňuje nevýhody jak metod založených na metodě sledování paprsku z počítačové grafiky tak na simulacích šíření svazků. Zdroj světla ze všech směrů najednou je zde popsán vhodným matematickým modelem. Navržená metoda umožňuje modelovat jen jevy na prvním povrchu, na který dopadá světlo ze zdroje. Pokračovat s tímto přístupem při dalších odrazech uvnitř kamene je principiálně možné, ale úloha se stává matematicky velmi obtížnou. Navržený přístup je ale zcela nový a otevírá prostor pro další výzkum. Metoda navíc prakticky zcela řeší problémy simulování kamenů, které mají velmi vysoký koeficient absorpce světla nebo jsou průsvitné.

Abstract

Production of gemstones and fashion jewelry stones is a multi-billion dollar industry. The evaluation of cut stones during their design, manufacturing, and sale is necessary. Computer vision is a natural tool for this evaluation.

Cut gemstones are, due to their manufacturing process, convex polyhedra. They are manufactured mostly from clear or absorptive transparent material.

This thesis advances two methods we have developed previously. The first approach starts with the geometrical model of the jewelry stone complemented with the material refraction index. A computer model of the stone is illuminated by a beam of parallel rays and computer simulation computes geometric and radiometric parameters of the exiting beams. The features and statistics are calculated on the simulation results. These features are used for stone evaluation or simulation results that can be presented to experts.

The second approach compares the result of the above simulation with physical experiments. The differences between simulated and laboratory experiments manifest the differences between the stone model and its actual physical shape. The computer model of the stone can be modified according to these differences.

This thesis contributes to both approaches. The simulation of the light beam propagation is extended to enable modeling of light absorbing materials. Hence, it is possible to model stones made from not only clear, but also light absorbing transparent materials to color transparent stones, which are common fashion jewelry stones. These contributions have significantly extended the range of the stones which can be modeled.

Methods for reconstructing the actual shape of a stone by comparing simulations with experimental results requires solving the correspondence problem. The thesis contributes to the solution of this problem by defining features which can be extracted during the simulation as well as in experimentally acquired images.

The collimated light beam propagation in polyhedral stones can be represented by a graph. It gives further insight into the problem as well as a tool for implementing the beam-tracing simulation software.

A completely new approach developed in this thesis is the method for simulating omnidirectional illumination. The light source coming from all directions is described here by a mathematical model. Although the proposed method enables the modeling only of reflection and transmission during the first incidence, it is possible to extend it to other reflections/transmissions in the stone. Unfortunately the task becomes mathematically difficult and calls for further investigation. Nevertheless, our approach opens the space for further interesting research since it removes the sampling issues of the previous methods based on ray-tracing and beam-tracing. Furthermore, our method completely solves the simulation of stones which are translucent or which have the high absorption coefficient.

Contents

Chapter 1

Introduction, Motivation

This Ph.D. thesis studies the principles, which can be utilized in machine inspection of cut glass stones used in fashion jewellery (bijouterie) industry. It is motivated by problems appearing in design, the analysis and inspection of manufactured gemstones. The principles summarized and understood in the thesis can be also utilized while designing new shapes of cut stones with desired optical properties.

The core question asked and answered in the thesis is how the light propagates and acts while passing trough a single cut stone and what patterns it exhibits in observed images. The topic is challenging from the image analysis point of view because it deals with almost transparent objects. On the other hand, the application domain in fashion jewellery industry brings constraints allowing to design and implement algorithms which can be deployed in real applications.

The thesis deals with cut stones used in the fashion jewellery from the shape, geometry, optics and radiometry points of view. The jewelry stones are designed and manufactured to provide appearance and optical effects pleasant to humans. The designer can choose only shape and material.

Diamonds have been cut to convex polyhedron shape of various time-proven forms. Examples of historic diamond cuts are shown in Fig. 1.1. Various forms of cut are in use now.

The glass stone is a finely ground piece of glass which is a convex polyhedron also in one of the time-proven forms. There are two main distinctions with respect to diamond cuts. First, the cut glass stones are produced industrially in large batches. Second, unlike diamonds, where the weight loss of the raw mineral while cutting is of big concern, the glass material itself is not so valuable.

The machine cuts used for glass stones are sometimes almost as sophisticated as for gemstones but they are simpler in most cases yielding a mass produced components. The example of the shape is named machine cut chaton (or simply the chaton or the rhinestone). See Fig. 1.2.

The thesis studies the underlying physical/optical phenomena, which (a) influence the jewellery shape and brilliance; (b) explain how one can asses the manufacturing quality of a particular stone by capturing the image of the light pattern reflected from the stone. The thesis provides the related theoretical optical, radiometric and image analysis background. It also suggests the novel analysis procedure. The work

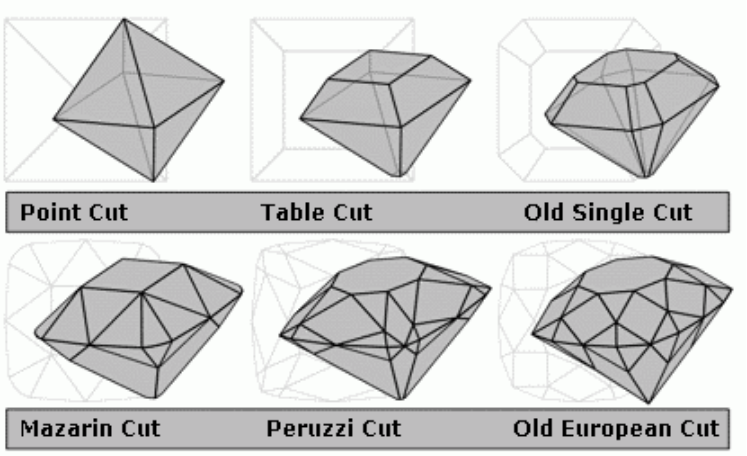

Figure 1.1: Examples of historic diamond cuts dating before M. Tolkowsky's guidelines from 1919 [170]. Source [174].

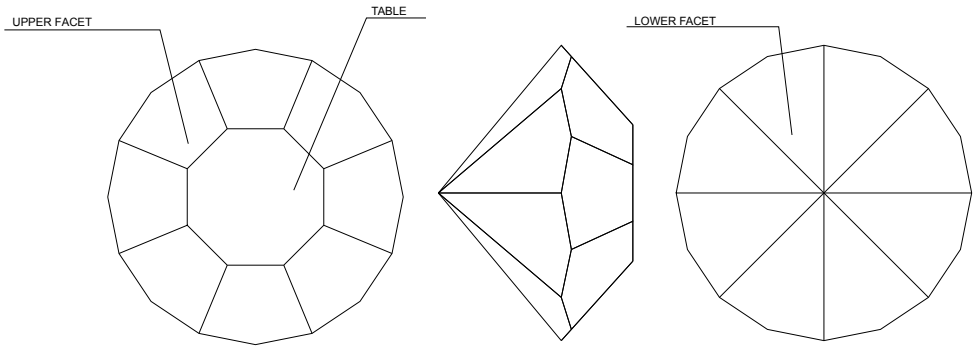

Figure 1.2: Chaton shape cut commonly used for glass stones.

deals with various material-based and other properties of cut stones too. Their understanding leads to procedures enabling assessing the production quality using image analysis and, consequently, enabling design/production of machines and the quality control procedures/instruments.

Knowledge of optics is needed for understanding reflection, refraction, and dispersion of incoming visible light and related image formation. The knowledge from geometric and wave optics is sufficient here. Knowledge from radiometry is needed too. It enables explaining how the image is formed.

Computer vision deals predominantly with opaque objects. The brightness (image intensity) of a particular infinitesimal surface patch depends on the direction to the light source, type of the illumination, direction to the viewer, patch orientation and its reflective properties (albedo). The properties of different materials are expressed as the Bidirectional Reflectance Distribution Function (BRDF). BRDF describes the brightness of an elementary surface patch for a specific material, a distant point light

source, and viewer directions as a ratio between a measured radiance reflected from a surface caused by irradiance from a certain direction. The influence of the phase is neglected for simplicity.

This thesis deals with special transparent objects designed intentionally to provide pleasant percepts to humans from reflections and refractions. The underlying theory has been much less studied. The thesis contributes to it.

1.1 Towards a model of cut stones

1.1.1 Terminological note

Let me start with a terminological note before I introduce several basic concepts. Cut stones are from diverse materials, which can be of natural origin like various precious or semi-precious gemstones or of artificial origin: glass, cubic zirconia (ZrO_2), moissanite (SiC), or diamond. The most important physical characteristics are the index of refraction and dispersion from the point of view of this study.

I use the term glass when I want to emphasize the physical properties of the cut stone material, mainly refraction index and dispersion. However, similar approach can be applied to other materials. On a few occasions, when numerical results are presented, the term glass means really glass material with refraction index around 1.5.

1.1.2 Stone and its mathematical model

The geometric model of the transparent object (a cut stone) is a polyhedron in most cases. The concept of the cut stone is modeled as a polyhedron equipped with additional physical properties like its material, refraction index, dispersion, absorption coefficient, etc. I use the term facet for the sides of the polyhedron.

The mathematical model of the cut stone, which we will use, can be described using the following concepts:

- **Convex polyhedron.** The raw natural or artificial stone is polished typically on the planar grindstone. Consequently, the resulting facet is almost planar. The polyhedron is convex as it is impossible to cut the concave shape by the planar section of the grindstone.

  Sometimes the grindstone has a cylindrical shape, where the diameter of the cylinder is much larger than the size of the facet. The ratio of their dimensions is in the order of hundreds. The planarity of the facet is an important quality factor as we will see later.

- **Index of refraction.** The index of refraction around the stone is the index of refraction of the air, which is 1.000277 under standard conditions. I set it to 1 in the model. The index of refraction of the stone interior is constant and known. The industrial manufacturer is familiar with the material used for manufacturing and can measure the index of refraction quite accurately on the sample designed for that purpose.

Figure 1.3: Fashion jewelry stones which are typical examples of interesting transparent objects. Photo courtesy of Preciosa a.s. [148].

- **Dispersion.** The dispersion of light which is caused by the dependence of the stone index of refraction on the light wavelength is considered when needed.
- **Optical quality surface.** The stone facets are polished to the optical grade where the roughness of the surface is much lower than the wavelength of the visible light.
- **Zero absorption.** The stone interior is completely transparent without any macro defects and light attenuation.

This idealized model of the cut stone will be relaxed in two directions later on:

- **Non-zero absorption.** The completely transparent medium of the stone interior is replaced by the absorbing medium with known absorption.
- **Rounded edges.** The straight line intersection of the facets is replaced by the smooth transition of the surface from one facet to the other one.

Those relaxations of the model allow to model very wide range of real stones and quantify their properties.

1.2 Gemstone properties valued by their users

1.2.1 Subjective human perception of cut stones

The evolution of mankind has made human eyes and brain particularly sensitive to the time derivatives of the light falling onto the photoreceptor cells, to the spatial derivatives of the light as well as to saturated light colors.

This fact is used in the jewelry industry. Even slowly moving jewelry stones produce fast moving relatively intensive, narrow, beams of light. Jewelry stones reflect and refract the light falling on their surface. The light, which is returned to human viewer, occurs in many discrete beams that fall into observer's eyes. The relative motion of the light source, stone and observer's eyes stimulate the observer's eyes by short pulses of light. These flashes are sometimes almost monochromatic. Jewelry stones exhibit this desired flash effect for diverse light sources.

A typical jewelry cut stone has a front part and the back part. The back part is inserted into the stone holder or often attached to the dress. It is assumed that the light is entering from the front side.

The attention mechanism of the human observer is naturally attracted by flashes to the direction of the incoming light. This turns the attention to the person wearing a piece of jewelry with a cut stone, which is the desired effect. The beauty, the user value and consequently the market price of the cut stones originates from this fact. The more intense, more narrow, and more numerous beams occur, the higher is their value.

Another enhancing feature of the above mentioned optical effects and its perception by a human is provided by beams of various colors. The color rays are produced either by absorbing part of the light spectrum in color jewelry stones or by dispersion of the light by refraction.

1.2.2 Objective assessment of the subjective perception of cut stones

The gemologists and jewelry cut stones manufacturers try to quantify the above described subjective effects in such a way which can be measured, analyzed, compared, and negotiated with customers. The ultimate aim of the objective assessment labeling the stone with the scalar score allowing gemologists to assess the market value of each stone. In the manufacturing plants, the quality control personnel together with production engineers attempt manufacturing cut stones products as perfect as possible for the given cost.

The origin of the above mentioned beams is the following. The rooms where the jewelry is worn are usually illuminated by a large number of highly localized light sources, e.g. crystal chandeliers with many individual incandescent light bulbs (or even candles in the past). Already this type of lamps produce many individual almost point sources of light. Notice that the fashion jewelry shops are illuminated by point sources, currently either halogen lamps or LED sources.

The light beam from the individual light source travels a relatively long distance and falls onto a gemstone. As the distance between the light source and the stone is in the range of meters and the size of the stone cut facet is in millimeters at most, one can approximate the illumination by collimated beams.

The light beam is partly reflected back by the stone facet and partly refracted into the stone interior. The refracted light beam in the stone interior is reflected inside the stone several times. The number of reflections can be infinite in principle.

The stones are preferentially made of materials with high index of refraction. The refraction from the air to the cut stone, e.g. glass, happens always. The refraction

from material to air requires having the incident angle lower than the critical angle for the given material. The critical angle for glass is $30 - 45°$, for cubic zirconia is $28°$, for diamond is $23°$, and for moissanite is only $22°$. The light falling onto the facet from the stone interior under larger angle undergoes total reflection, where all the energy remains in the material. The total reflection is frequent and in some cases intentional, e.g. at the bottom part of the cut stone.

Each time the beam hits the facet under the angle lower than the critical angle, part of the energy is reflected back to the stone and part of the energy is refracted out of the stone. When the beam hits two or more facets at the same time, each facet reflects part of the beam to different directions thus forming new beams.

The refraction at the entrance facet of the stone and refraction at the exit of the beam from the cut stone also involves dispersion, which means that parallel rays of different wavelengths become nonparallel after refraction. This effect depends on the light beam wavelength and dispersion of the materials. The dispersion thus produces colored beams. The color beams in this case are not distinct, non-overlapping separate beams but rather each original ray of white light produces a continuous pencil of rays with continuously varying wavelengths.

Summary of the effects multiplying the number of beams in this scenario:

1. The number of light sources in the scene (e.g. chandeliers, small light bulbs,. . .).
2. The number of stone facets reflecting the light.
3. Bouncing of beams inside the stone, new refracted beams are produced at some bounces.
4. Beam split when a beam falls onto two or more different facets.

The stone is not a light amplifier, so the only energy which is exiting the stone can be the energy of incident beams. The refracted beams from the stone have only fractions of the original incident beam energy.

Further the beam energy can be lost by several effects:

1. Absorption in the absorbing medium. The absorbing medium causes exponential decrease [76] in the beam intensity depending on the length of the beam travel in the absorbing medium and properties of the medium.
2. The non-polished surfaces of the stone cause spreading of the beam energy into large solid angle, the beam is no more close to the collimated and all user effects associated with the gemstone are lost.
3. The beam which is trapped between two or three facets having the internal angles lower than $90°$ end up in the edge(s) between facets. The edge between facets is not ideally sharp in the practical case. The incoming beam energy is spread at the edge spread over a large solid angle. The energy of the beam is lost for the stone wearer. Actually the edges with the internal angle between neighboring facets lower than $90°$ are very rare or non-existent in the jewelry industry.

1.3 Organization of the thesis

The contribution of the thesis is summarized in Chapter 2. The broader state of the art related to the reconstruction of transparent objects is presented in Chapter 3. The overview of our past activities and results is given in Chapter 4. The terminology and used concepts of physics are introduced in Chapter 5. The thesis contribution is described in four chapters. The representation of the collimated light beam propagation in the stone by a graph is presented in Chapter 6. The extension of the simulation model for absorbing transparent materials is described in Chapter 7. The optical effects on the stone edges, which simplifies the correspondence problem in the stone shape reconstruction task, are analyzed in Chapter 8. The novel approach for the returned light evaluation considering an omnidirectional source of light is described in Chapter 9.

Chapter 2

Contribution

The contributions of this thesis are related to modeling how collimated light beams propagate in transparent jewelry cut stones of a polyhedral shape.

The thesis extends the existing models [145, 83, 152] in several directions:

1. It offers a novel and systematic view on the beam-tracing approach of light propagation simulation.

2. The material of the modeled stones can be light absorbing.

3. The polyhedral shape of stones is extended to polyhedra with rounded edges.

4. The radiometric evaluation of the stone properties is extended beyond discrete ray-tracing [152] and beam-tracing [145] models to a novel integral model of light propagation.

2.1 Light paths as a graph

The collimated beam propagation in a polyhedral cut stone is studied from a standpoint dealing with new beam formation. New beams can appear as the result of the first interaction, i.e. by beams splitting while interacting with multiple stone facets at once. This first interaction is geometrical, generated by the shape of stone. The second interaction generates new beams by reflecting and refracting the plane wave of the beam on the planar facet. The second interaction has a physical origin. It is modeled by the laws of optics. See Fig. 6.1.

The proposed method arranges newly generated beams into a graph. The graph is a tree for a single illuminating beam and a forest for multiple beams. The graph has a regular structure. The layer of beams originating in splitting interleaves with the layers of beams originating in reflection and transmission. Attributes describing geometry and radiometry are assigned both to nodes and to edges.

The graph model gives better insight into the physics of collimated beam propagation in jewelry cut stones.

2.2 Light propagation in an absorbing medium

The beam propagation model in transparent stones was extended by modeling of light absorption in the stones. The contribution of thesis is in the derivation of analytic expressions enabling the calculation of the radiant flux of attenuated beams by the light absorption in stones. Also proposed is a methodology for simulating light propagation in convex light absorbing media bounded by planar surfaces. The model is taking fully into account the polarization caused by reflection and refraction on planar facets.

We assume absorbing transparent medium, which propagates planar light waves without deformation. The medium is attenuating, which means that planar waves remain planar, but their amplitudes decrease exponentially [76] while traveling in the medium. The medium does not scatter light.

The enhanced model enables the computation of radiometric properties of beams propagating in color stones that constitute an important commodity in the jewelry industry. The derived formulae calculate the radiant flux of the collimated beams formed in the collimated beam illuminated stone. The calculated radiant flux can be used for evaluating cut design quality characteristics, e.g. dispersed-color light return (DCLR) [152] and light return [93].

2.3 Optical effects on the stone edges

The model of polyhedral stones proposed in [145] proved to be insufficient to describe effects visible in the experiments with real stones illuminated by collimated beams of light. The contribution of the thesis is in extending this model by incorporating rounded edges of the stone.

The reflection and refraction of collimated beams on rounded edges produce rays lying on a conical surface of revolution. This fact is proven under very general and realistic assumptions about the shape of rounded edges.

Additionally analysis is given that demonstrates that each rounded edge produces protrusions on the beam traces on the screen.

We introduce methods that enables incorporating the simulation of the edge rays into the simulation model. The proposed technique was implemented and demonstrated in simulations of practical stone shapes.

The extensions enable an improved simulation of collimated beam propagation through stones with rounded edges. In particular, the extension enables matching beam traces obtained experimentally with the simulated traces. This matching was intractable for realistic stone shapes before, e.g. for chatons [83]. The edge ray traces enables the design of features for solving the correspondence problem.

2.4 Reflection and refractions on the first surface of a stone

We introduce a novel approach to theoretical evaluation of stone cuts. Unlike previous ray-tracing and beam-tracing approaches, our method for calculating stone parameters is related to the radiometric efficiency of the stone. The light return [93], DCLR [152], and similar parameters can be evaluated by the proposed method.

Our method avoids sampling the ray or the beam space while simulating the light propagation and lets the user define his requirements. The evaluation of the resulting elliptic integrals [71] is a well a studied problem [88].

The contribution of this thesis is mainly in problem formulation and solving elementary steps in this direction. The formulation and solution of more intricate tasks is a topic for future research.

Chapter 3

Work of Others

The transparent object reconstruction has become topical among computer vision researchers lately. The main reason for the interest is that transparent objects involve many challenges not tackled/solved by the previous research. This chapter summarizes the state of the art related to the thesis topic from a broader perspective. The more specific works of others are discussed and referred to in Chapters 7-8.

3.1 Transparent objects reconstruction

A good overview of the transparent object reconstruction methods can be found in [102, 103]. Authors of [102, 103] classify the reconstruction problem into the subclasses according to optical properties of reconstructed objects. Their classification is based on the properties of the objects material and object surface.

There are two main optical properties of the objects to which the measurement method design should respond. These are optical property of the object material and optical property of the object surface.

The **object material** taxonomy according to its optical behavior, from the point of view of physics [85], is:

1. **Metallic** materials are opaque in visible light. They are typical examples of reflective materials in the combination with a smooth (polished) surface. The material can absorb some wavelengths to change color of reflected light (e.g. the copper).

2. **Dielectric–scattering** materials are usually composed of transparent media filled with particles, on which the light scatters. The quantity of particles determines the degree of the scatter. Only slightly scattering materials are considered translucent.

3. **Dielectric–transparent** materials do not scatter light. Transparent materials can involve absorption of light such as in tinted glass.

The **object surface** can be classified according to its smoothness, where unevenness size is compared to the wavelength of the light used to illuminate the object:

1. **Matte** is a surface with micro-structure rough enough to reflect the incident light in all directions. The intensity of the reflection in the direction given by the law of reflection is negligible.

2. **Glossy** surfaces reflect the light according to the law of reflection partially and diffuse it into other directions also partially.

3. **Optically smooth** surfaces are such that Fresnel equations describe the propagation of the light well.

The quantitative condition for a surface being smooth is Rayleigh criterion. The mechanical surface roughness, needed for evaluating Rayleigh criterion, is difficult to measure directly in the ranges, in which surfaces appear smooth. Optical methods such as Bidirectional Reflectance Distribution Function (BRDF) measurements are used for measuring of the optical smoothness. We will not define matte and glossy surfaces more exactly here, as we are not interested in such surfaces in our work.

The object from the point of this thesis view can be represented as a Cartesian product of the object material and the surface.

Computer vision is often interested not in a single object but in a scene, where multiple objects can be falling into several different categories.

We are mainly concerned with objects with optically smooth surface made of dielectric–transparent material. We allow absorption of light in material. We assume that the index of refraction inside the material is constant, the material and the surface are isotropic. Some parts of the surface can be made fully reflective by applying metallic coating.

The classification of the scenes or objects presented in [102, 103] is not complete. There is still further research needed to fully cover reconstructions of all types of scenes.

A very important article in the field of reconstruction of transparent and specular objects is [110, 109]. They contributed to the classification of light–path triangulation problems as follows: Let us have N viewpoints, K points on the scene surfaces, where reflection or refractions happen along a single ray, and M points defining the properties of light source of ray. Fig. 3.1 shows the meaning of the variables. Kutulakos presented classification of (N, K, M) triples, attributed the solvability to them, and assigned a classical solution to them if it exists.

The proposed classification is not complete. For example, polarization is not involved. Also a ray from illumination, described in Kutulakos work as passing through M points, can have a different parametrization, e.g. lying on the straight line, such as in [126]. Although not complete, the idea of classification of computer vision methods according to geometry of rays forming the image is the first key contribution. The second Kutulakos et al. contribution is the demonstration of reconstruction of specular and transparent object. The second contribution is explicated in the coming Section 3.7.

Kutulakos et al. [110, 109] also proved solvability or insolvability of several (N, K, M) problems. A more general classification covering all known computer vision methods is still an open problem.

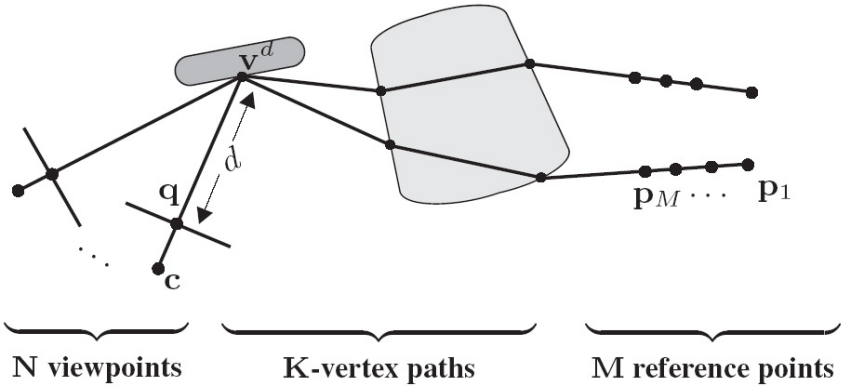

Figure 3.1: Geometry of the image formation for study of tractability of several reconstruction problems. [110]

The article by O'Toole and others [144] does not deal directly with the reconstruction of transparent objects. However, it is closely related to the study of individual rays in a scene. The authors call their method Primal-Dual coding as they use one panel with the controlled transparency for illumination and another one for masking the pixels in camera for exposure. They designed the system, which illuminates and observes the scene along the same set of rays. Further, the light passing from the light source to the scene as well as the light passing from the scene to the camera can be controlled (blocked) on the level of individual pixels. The basic setup uses a single exposure image, which is actually composed of many "sub-exposures", in which some of the rays from the light source and/or some of the rays to the camera can be blocked. The blocking is done via two LCD panels, where individual pixels are programmed to be opaque. Any combination of "pixel" rays can be used for the illumination while any combination of pixels can be exposed via the coding masks.

The authors show that by combining (that is by time multiplexing) various sets of illumination rays and various sets of exposed pixels the different images of the scene can be constructed. These images may show different components of the image, e.g. the image without specular reflections. In this way, it is possible to get in just one exposure the image of the light, which is reflected directly by the scene to the camera or to get the image composed from inter-reflections entirely, etc. The method can be used in various specialized applications like to illuminate only the pixels in certain depth or to perform con-focal photography. The authors show only a small sample of possible coding schemes for analyzing various scene situations. Although the method requires a complicated hardware, one can see a lot of industrial applications where such approach can be groundbreaking. The setup is shown in the Fig. 3.2.

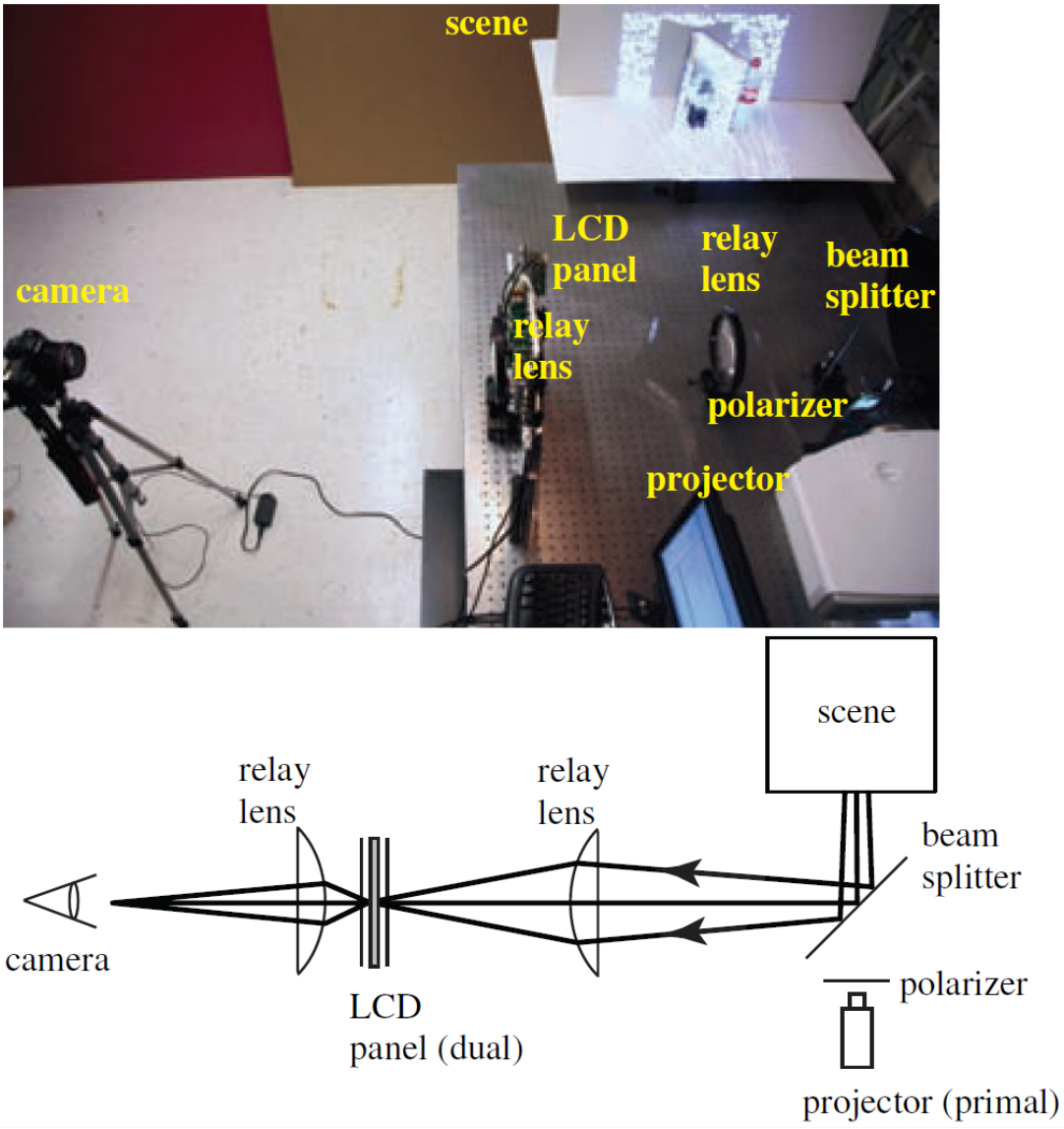

Figure 3.2: The setup of the Primal-Dual coding method. The primal code bitmap is used in the first LCD projector which illuminates only selected parts of the scene. The dual code is sent to the second LCD which allows light to pass from the scene only to the certain pixels. The camera in this setup only integrates incoming light over the sequence of applied codes [144]

.

3.2 Elimination of transparent objects in front of the object of interest

Early works [128, 129, 136, 130, 131, 72] tried to eliminate the influence of transparent or translucent objects. One can consider the camera lens as transparent object. The radial distortion elimination is one example. Another example is the impact of fog on the image formation. Nayar [136, 130, 131] is particularly active in this field. They studied various optical phenomena of weather influence on the captured image and tried to use it for solving classical computer vision tasks like the depth estimation.

Murase [128, 129] studied the more advanced task. He tried to eliminate the distortion of the image of the rigid object submerged in water resulting from the refraction on the water rippling surface. He used the optical flow to estimate distortions caused by the water in a statistical manner and reconstructed the image of submerged object later.

A sequence of input images allows estimation of parameters of water surface motion. Information about the water surface enables eliminating its influence to the image of the submerged object.

Agarwal et al. [72] studied similar setup but with different approach and different results. They assumed a moving rigid scene behind a static rigid transparent object and a static camera. The method, which builds on the optical flow, was able to reconstruct the mapping between a planar scene and the image in the presence of transparent object. The mapping describes which part of the scene plane is projected to which part of the image when transparent object is placed between them. The output of the method is this mapping; the method does not produce the explicit reconstruction of the transparent object shape.

3.3 Reconstruction of transparent or specular objects by avoiding their transparency or specularity

The following methods convert a difficult problem of reconstruction of transparent objects into a well known reconstruction of opaque objects. They actually do not contribute to the theory of transparent objects. On the other hand, the approach can be very useful in practice when conditions for their application are satisfied.

3.3.1 Painting of transparent or specular objects

When the transparent objects are either painted or sprayed with dust particles, many active and passive methods developed for opaque objects with diffuse surface can be used. The overview can be found in [87, 78]. This approach is often not acceptable in practice as it can be considered destructive.

3.3.2 Scanning from heating

A different way how to avoid transparency can be a shift of the used radiation wavelength into the regions, in which the material is not in fact transparent. The

method [91, 90] reconstructs glass or plastic objects using a thermal radiation in the wavelength around 10 μm. The objects made from glass or acrylic, which are transparent in visible light, are highly absorbing when illuminated by the light of this wavelength.

While reconstructing, the laser beam heats up the point on the object surface. The projection of the hot point is found in the image captured by a thermal-camera. The visible surface of the object is reconstructed point by point while the laser beam is scanning over the surface. The physical properties of the scanned material important for the method behavior are carefully analyzed. See the results in Fig. 3.3. The drawbacks of this method are the cost of the equipment and the slow data acquisition.

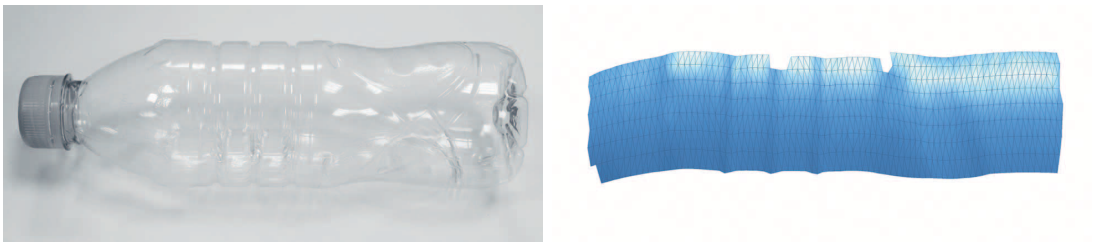

Figure 3.3: A transparent object (left) and its reconstructed model obtained by scanning from heating. [91]

3.3.3 Scanning by UV light induced fluorescence

Meriaudeau et al. [120, 151] used a simple system with a point or line laser in UV band with scanning over the transparent object. The fluorescing point is observed by the camera in the visible light. The method requires special properties of the transparent material, that is its fluorescence. Its precision is characterized by the mean deviation error of about 0.1 mm, which allows generating accurate 3D models of transparent objects made from specific materials. See Fig. 3.4.

3.4 Volumetric methods

3.4.1 Tomography

The tomography assumes that the observed object is made of absorbing material while the index of refraction is the same for the object and surrounding media. Adaptation of tomography for objects transparent in the visible light was demonstrated by Trifonov in [171]. Immersing transparent objects into liquid with identical (or at least similar) index of refraction eliminates refractions on the object surface. Such fluids exist for glass and transparent plastics, although they are mostly toxic. The absorption of the light (i.e. the absorption coefficient of the material) in the liquid or in the object or in both of them should not be identical. The reconstruction uses standard tomographic methods. The object example and its model are shown in Fig. 3.5.

Another application of tomography-like method in visible light is capturing the shape of smoke or flames as presented in [98]. The light was emitted by the hot soot

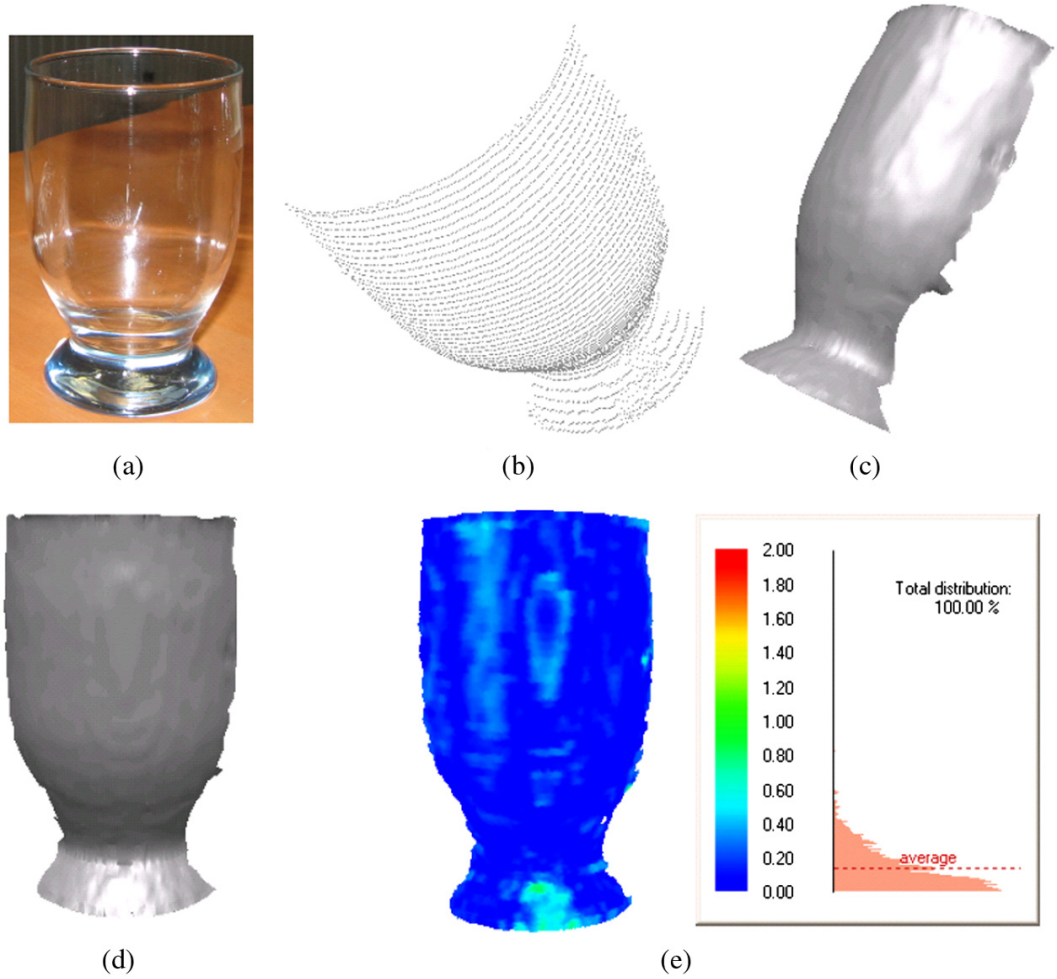

Figure 3.4: A transparent object (top left) and its reconstructed model obtained by scanning UV laser where the fluorescent spot was observed by camera in visible light. [151]

particles, thus the amount of light was proportional to the soot density. Refraction of emitted light was neglected. They used only few images, for example two. The ambiguity in the data is reduced by the assumption that the reconstructed object is the most compact and connected. See Fig 3.6.

Flowing water can be captured in real time [101]. The method falls into the tomography category. A fluorescent light emitted from water is used as a source of information about the presence of material. See Fig. 3.7. The emission is explored here instead of absorption. The difference to tomography method is that the light is refracted in the scene, so standard tomography reconstruction cannot be used. The task is formulated as a photo-consistency optimization of input images with the model. The task is solved by the level set method.

Figure 3.5: A transparent object (left) and its model obtained by the tomography. [171]

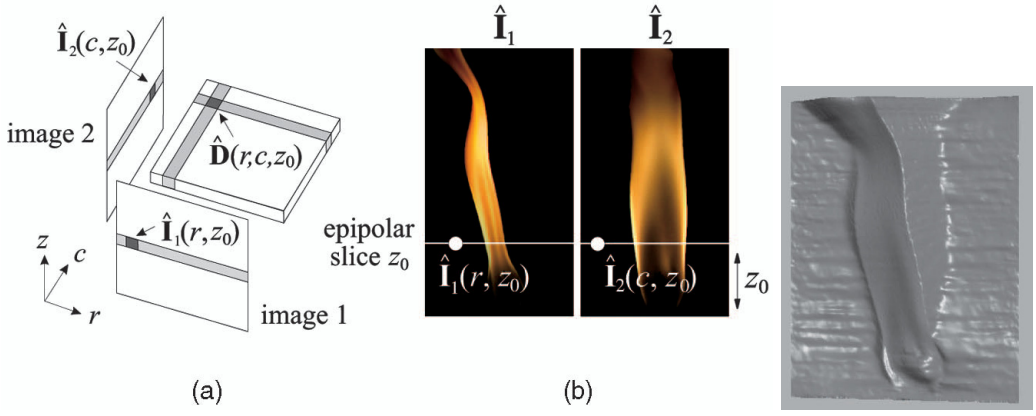

Figure 3.6: The reconstruction of flames using the density sheet decomposition. (a) Viewing geometry with two orthographic cameras observing density function. (b) Two input images. Right: flame model from the novel view. [98]

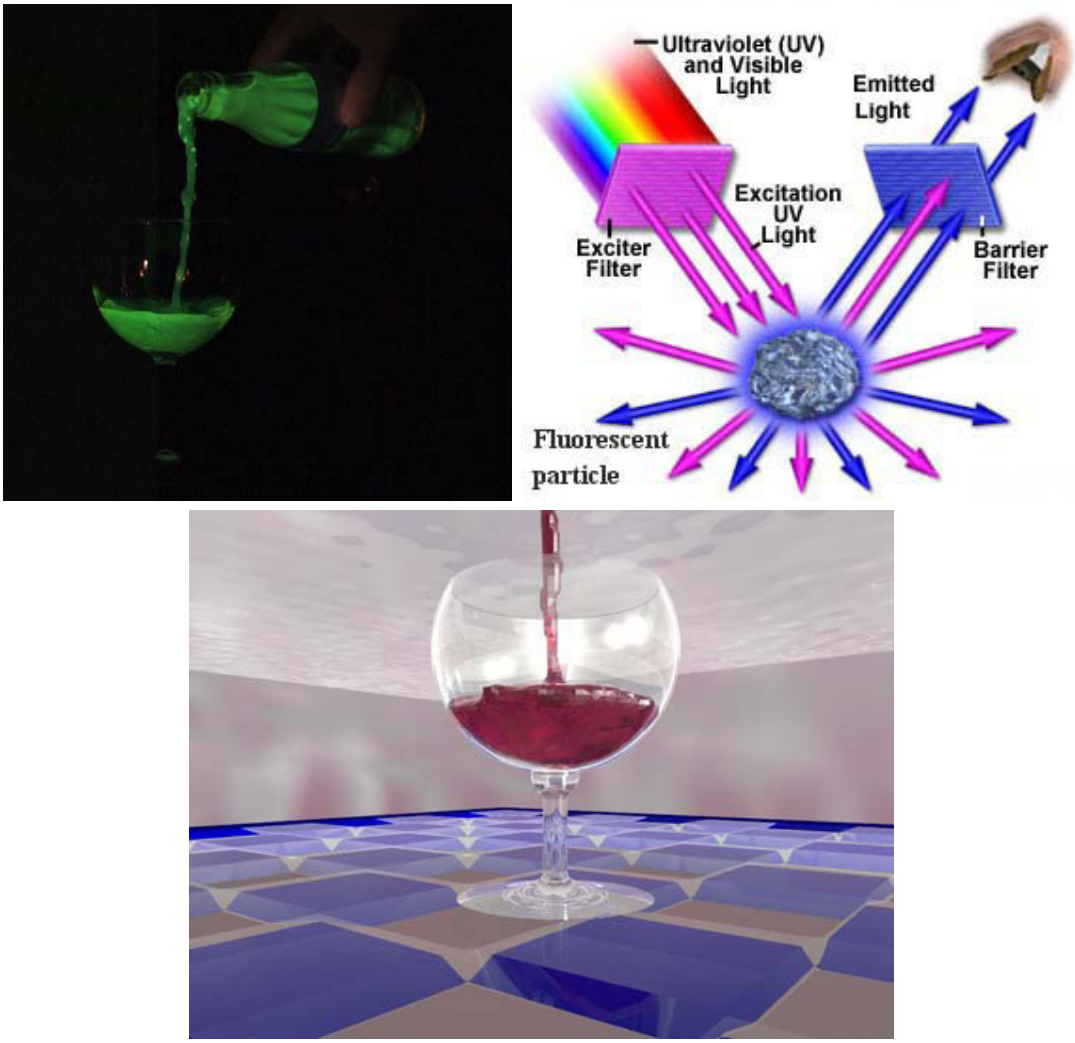

Figure 3.7: The reconstruction from the emitted light. Upper left: The water with dissolved fluorescent agent illuminated by an ultraviolet light. Upper right: The principle of capturing the emitted light. Bottom: Reconstructed surface used in a virtual scene. [101]

3.4.2 Translucent media reconstruction

Gu et al. [96] presented the method for reconstructing a volumetric model of translucent media (see Fig. 3.8). The method models the following physical effects: The light ray with the known position in space enters the reconstructed scene. It is attenuated by absorption and scatter while it propagates straightly through the scene. It is supposed to scatter in the currently modeled voxel. The scattered light ray is falling into the camera, while being attenuated on its way through the media. The amount of attenuation and scatter in the voxel is supposed to be proportional to the density of the material in the voxel. The method estimates the material density in each voxel in order to optimize the agreement between measurements (images) and modeled measurement. The method supposes a low density media like smoke, where double scattering is negligible.

The method uses theory of compressive sensing [89] to reconstruct volumetric data from only few images.

The programmable light projector is used as the source of light. Several different patterns of light (e.g. 24) are projected and corresponding images are captured. Compressive sensing method allows reconstructing the volumetric model of the object.

3.5 Interferometric methods

A completely different approach is used by the laboratory equipment which uses optical (mostly interferometric) measurement of surfaces. System [177] is an extension of the scalar interferometric distance measurement to capture 2–D range data. The method accuracy, which goes down to nanometers, is way ahead of traditional computer vision methods in terms of the obtained scene model accuracy but lacks the speed of most computer vision methods.

3.6 Surface orientation measurement exploring polarization

Saito et al. [156] describe a method for estimating surface orientation by analyzing the degree and orientation of polarization. The surface reconstruction is obtained by integration of surface normals. The refraction index of the material is known. The method uses isotropic spherical non-polarized light source (see Fig. 3.9) to produce specular reflections on most of the surface. As transparent objects have no diffuse reflection, light coming to the camera is modeled by the specular reflection. The method neglects light, which is refracted on the surface, which passes through the object and then (perhaps after several internal reflections) is refracted out to the camera. Experimental results do not show bias caused by this effect but it can be due to the suitable shape of the object they used.

The work was extended by Miyazaki and Ikeuchi in [123, 121, 122]. They assume a known shape of a back side of the object and the known index of refraction of the object. They optimize the agreement between measured polarization and rendered polarization using 3–D model of the reconstructed object. The experimental setup

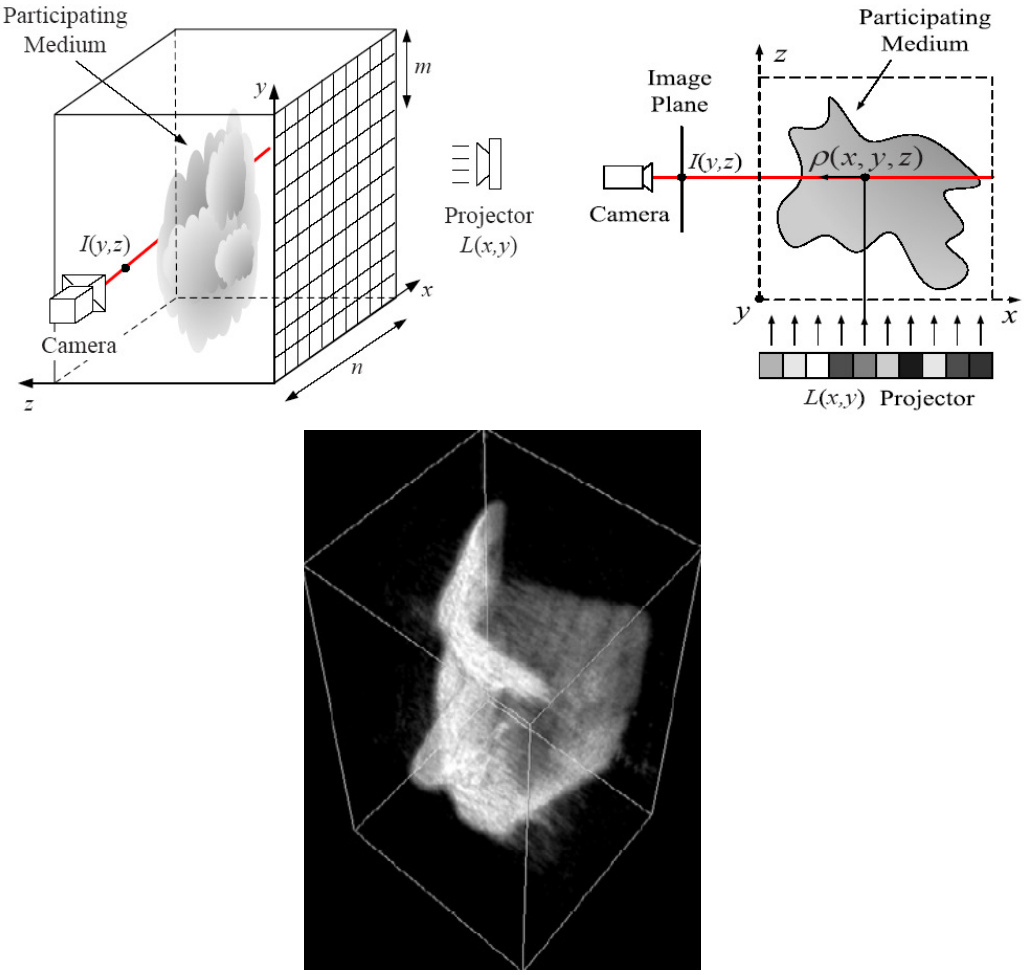

Figure 3.8: Compressive sensing reconstruction. Image formation geometry (top), reconstructed model (bottom). [96]

(see Fig. 3.9) is demanding and several images are needed to estimate polarization. See Fig. 3.10 for results.

Another method uses the polarization caused by the reflection on the transparent object and it is presented by Meriaudeau [120]. The method uses active illumination in a thermal IR region.

3.7 Triangulation of the surface points

The method [135, 134, 132, 133] is recovering the positions of surface points from the reflection on the surface. The method works for transparent, translucent, and opaque materials with smooth, glossy, or rough surfaces. The method (see Fig. 3.11) is based on exhaustive scanning of the surface by a laser and simultaneous exhaustive positioning of sensor, searching for diffuse or specular reflection on the surface.

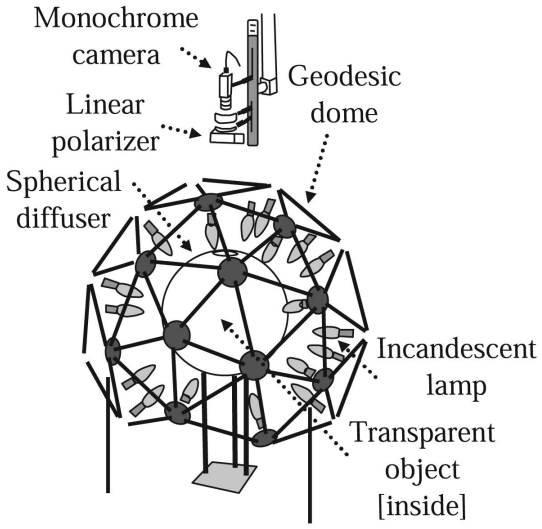

Figure 3.9: Reconstruction of a transparent object using information about the polarization state of the image. The image capturing setup aims to produce diffuse light from all directions. [122]

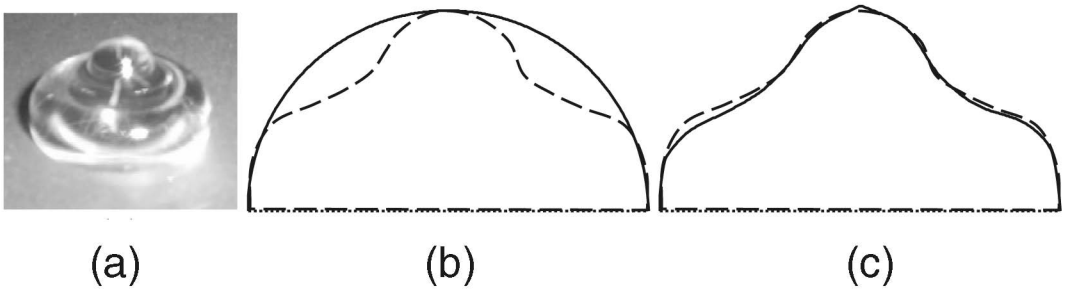

Figure 3.10: Reconstruction of a transparent object using information about the polarization state of the image. (a) photo of the object, (b) initial value of the shape (solid), true surface (dashed), (c) result of reconstruction (solid). [122]

The disadvantage of the method, though not mentioned by authors, is its very low speed. The method is probably not able to handle complicated scenes with transparent objects, where multiple reflections or refractions happen. Authors demonstrate the method on thick plane parallel plates, which are important industrial products, of course.

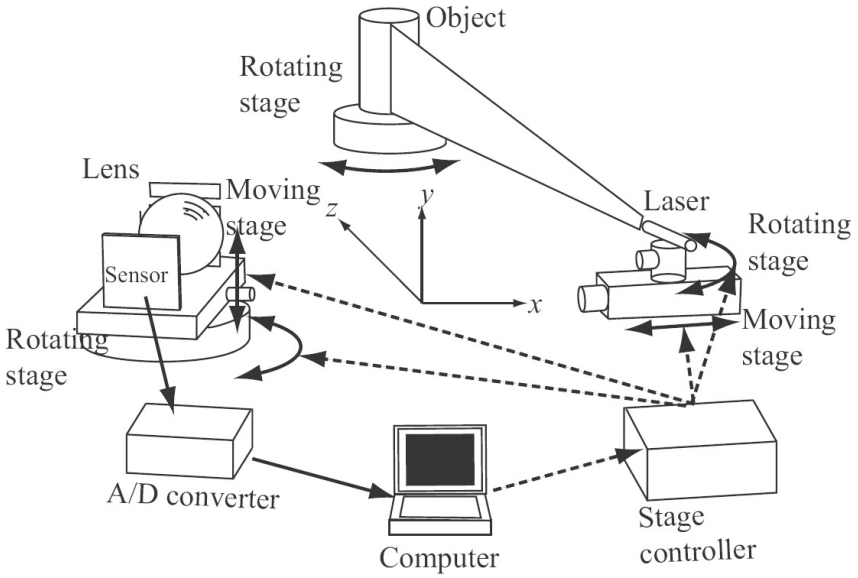

Figure 3.11: Reconstruction of a transparent object using a range finder and an exhaustive search. The image capturing setup. [132]

Tarini et al. show in [169] a slightly modified approach. The setup and the results are demonstrated in Fig. 3.12. They aim at measuring specular surfaces without a diffuse component, e.g. mirrors. In this sense, they are more restrictive than Narita [135, 134, 132, 133]. On the other hand, the data acquisition process needs far fewer images. This improvement is reached in two ways. The source of light based on a coded pattern allowing to decrease the number of images. On the other hand, there is a lack of knowledge about the direction of light emanating from the light source. The light source is omnidirectional and thus the unknown light direction has to be compensated by the optimization step seeking the surface depth. The method can be classified under the shape from distortion.

The method uses a flat panel display as a source of light. The different patterns projected on the display allow to identify for each pixel in the camera the point on the display, which is reflected in the scene. There is one dimensional ambiguity in depth in the pixel. This ambiguity is solved iteratively by assuming continuity of the surface via minimization of the so called coherence.

The second contribution of the work [110, 109] is the demonstration of reconstruction of specular and transparent object classified in this paper as $(1, 1, 2)$ and $(3, 2, 2)$ according to [110], see Fig. 3.13. Authors used LCD monitor as a source of light.

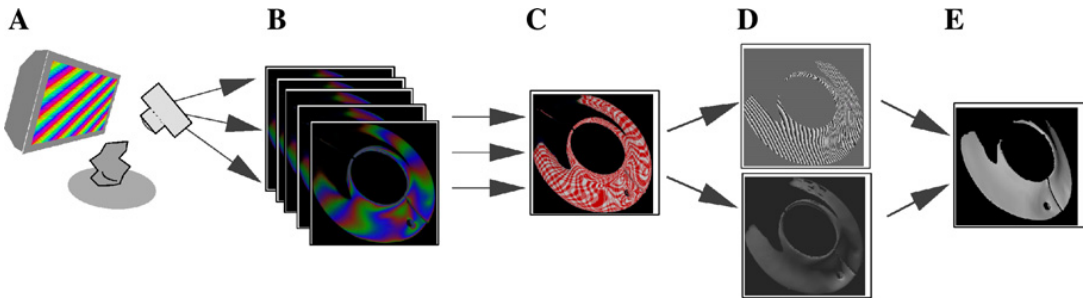

Figure 3.12: Shape from distortion, the data acquisition setup and results. (A) shows the setup where several patterns are displayed on a computer monitor and reflected by the object. Corresponding images (B) are captured. From these images, the map (C) between the computer monitor and image coordinates is obtained as the light from monitor is reflected by the object to the camera. Normals and depth (D) are obtained in the optimization step. The result is shown in E. [169]

They reconstructed two objects: the flat mirror as an example of specular object and the cut stone of the transparent object, see Fig. 3.14.

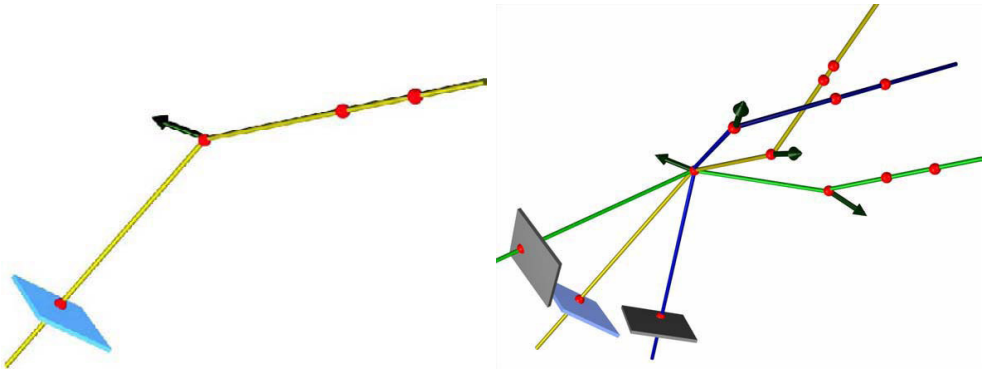

Figure 3.13: Triangulation principle for the light path triangulation. Left image shows a specular surface illuminated by a known ray and observed by one camera, $(1, 1, 2)$ setup. The right image shows three cameras observing one front surface point and three illumination rays with three back surface points ($(3, 2, 2)$ setup). [110]

Kutulakos et al. used a flat panel displaying different patterns. As they used it in two different positions, illumination rays were defined. One camera for specular surfaces and three cameras for transparent surfaces are sufficient for the successful reconstruction.

Tarini's work [169] was extended by Yamazaki et al. [175]. Besides considering specular objects, they worked out the rays trajectory through transparent object with just two refractions and known index of refraction. They used the structured illumination using a flat panel display in two positions. The proper decoding of the sequence of patterns allows obtaining the viewing ray as well as the illumination ray for each pixel in the camera. In the optimization step, they were looking for such

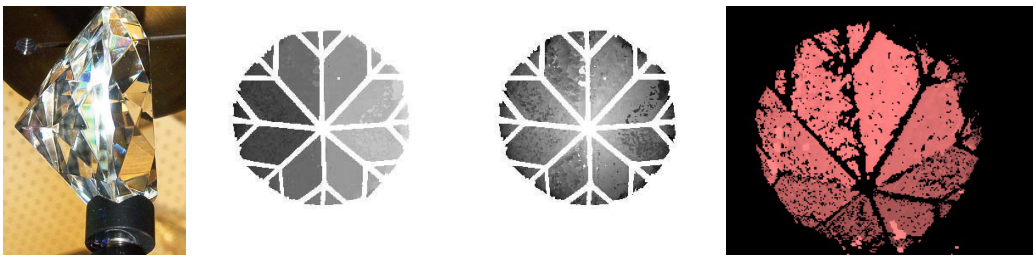

Figure 3.14: Reconstruction of the transparent object in $(3, 2, 2)$ category. From left: the object to be reconstructed, its normal slant map, depth map, oblique view on the model. [110]

positions of the surface points along the viewing and illumination rays which are compatible with the stereo images acquired. The front and back surface refractions observed in stereo images should have identical depth and normal. This method would be classified according to [110] as $(2, 2, 2)$. See Fig. 3.15.

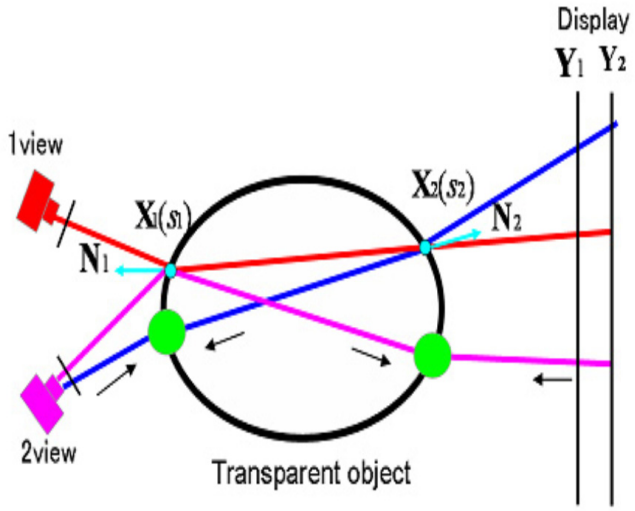

Figure 3.15: Reconstruction of a transparent object using the structured back illumination. The principle of the method, two cameras observe transparent object with structured light back illumination which allows identifying the illumination ray. The optimization searches for compatibility of the depth and the normal of both front and back surface. [175]

Although their work is theoretically sound, the accuracy of practical results is not very encouraging due to the sensitivity to data. It seems that the regions, where background texture is only slightly distorted in captured images, cannot be recovered due to uncertainty of the position of intersection of almost parallel lines. Regions where the background texture is highly distorted are not reconstructed accurately due to under-sampling. See Fig. 3.16.

Ben-Ezra and Nayar in [77] reconstructed the shape of a rigid transparent object

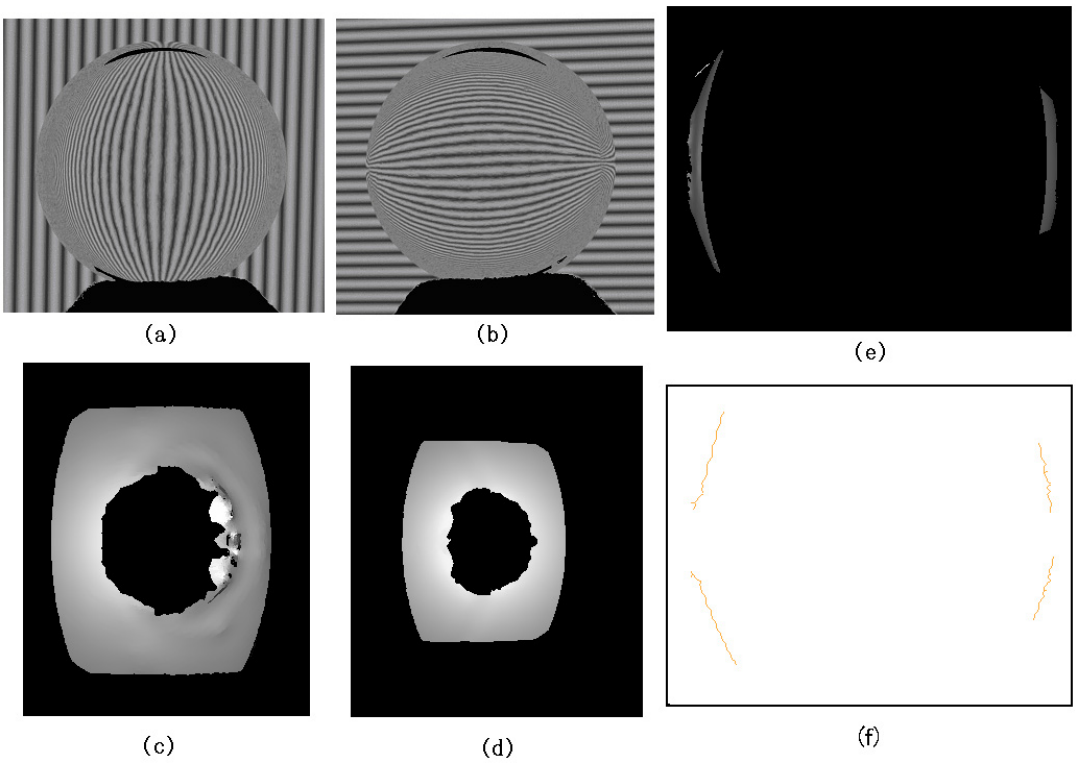

Figure 3.16: Reconstruction of a transparent object using the structured back illumination. (a) and (b) are input images, (c) and (d) are visualizations of the front and the back of a reconstructed surface, (e) is a side view of the resulting model, (f) a planar cut through the resulting model (the front is on the left side). [175]

in front of a rigid opaque scene captured by a moving camera. They assumed a rigid scene far behind a rigid transparent object while the camera was moving close to the transparent object. Assuming a large distance between the transparent object and the background enables reconstructing the transparent object shape. Their method can be classified according to [110] as $(N, K, 2)$.

They formulated the task as the optimization problem with a parameterized model of the object (superquadric in this case). The knew viewing rays (see Fig. 3.17) from the set of calibrated images. The rays should pass through the object in such a way that illuminating rays are parallel. A non-parallelism of rays is minimized in the procedure. The results are shown in Fig. 3.18.

A similar approach was presented by Morris and Kutulakos in [125, 127] and called the Dynamic refraction stereo. The method basically extends the stereo problems to the situation where the opaque object is observed through the single refractive surface. As the method uses only two images from two viewpoints, it can be easily used for a dynamic scene allowing reconstruction of the moving object, in this case a water surface.

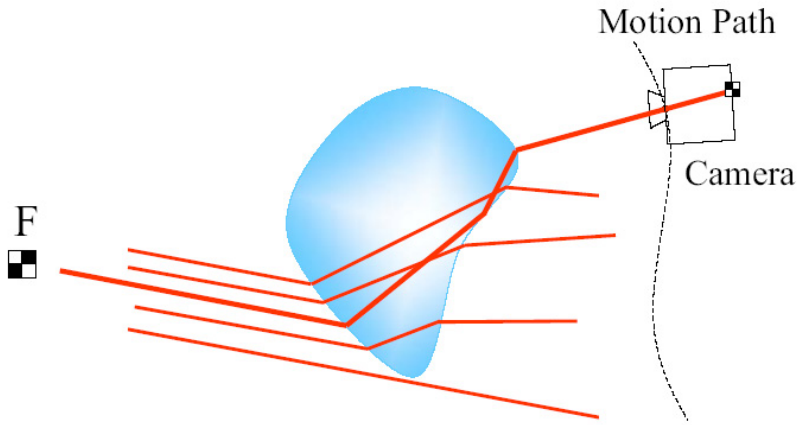

Figure 3.17: Reconstruction of a transparent object from the camera motion. As the background is far from the object, different viewing rays observing the same part of the background should be parallel. [77]

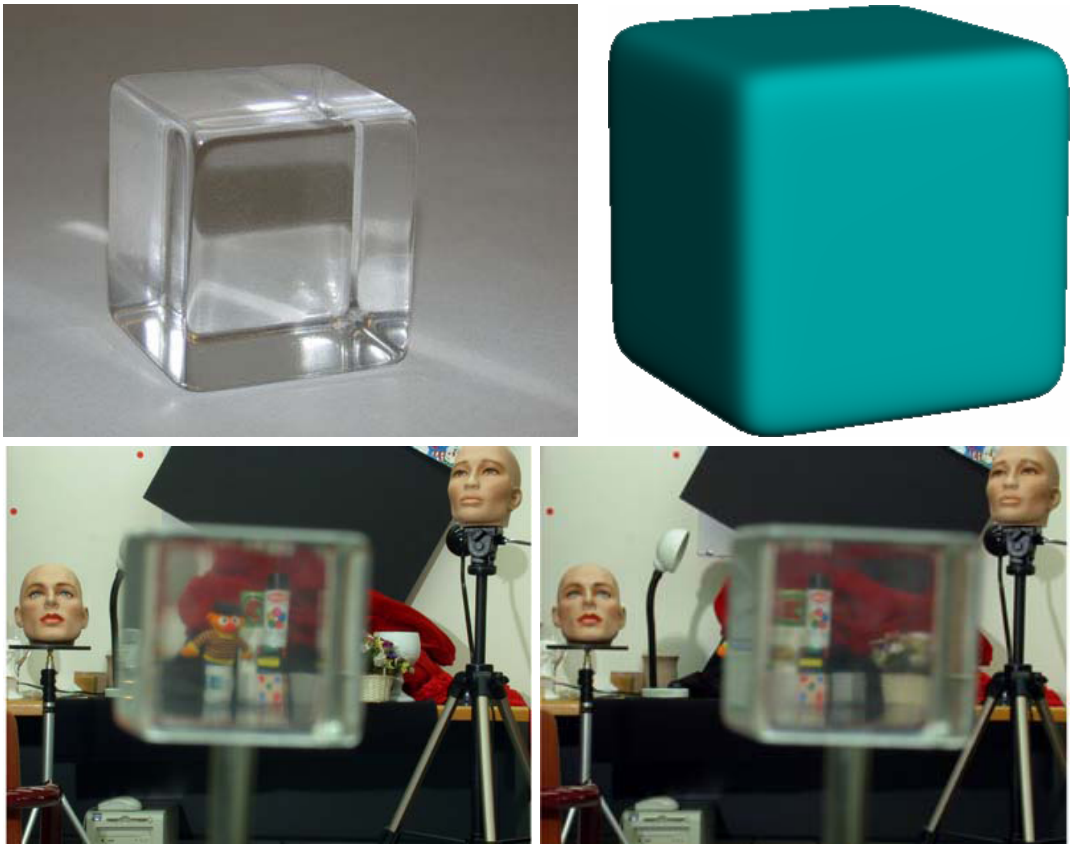

Figure 3.18: Reconstruction of a transparent object using moving camera. (From the top left) the true shape of the transparent object, the reconstructed model, examples of input images. [77]

3.8 Scatter trace photography

A powerful method was presented by Morris and Kutulakos in [126]. The method tries to reconstruct all surface points of specular and diffuse objects even in the presence of transparent materials and complicated optical effects inside them, as well as on their back side. The assumptions about the objects are quite general. The method relies on the scatter trace data which is a set of images of the scene captured while the light sources are moved in the space, or more precisely, they are positioned in two or three dimensional lattice. Authors proved that certain rules held for the data captured in this way and that the first point on the ray from camera pixel intersecting the object can be reconstructed. Authors also presented methods to decrease the number of images captured during data acquisition phase significantly using the line instead of point light sources and Hadamard codes [161] for projecting many line sources at a time. Experimental results for the simple object are shown in Fig. 3.19.

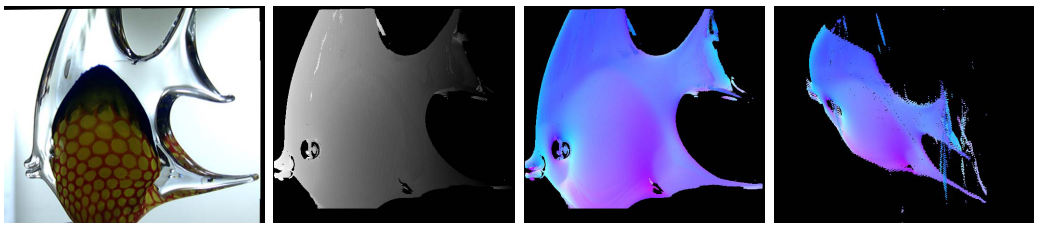

Figure 3.19: Photo of a transparent object (from left), depth map, normal map, and visualization of captured model obtained by the scatter trace method. [126]

Somewhat similar approach was used by Ma et al. [113]. The method captured intensity images behind the object at two different planes. Under strict assumptions about the source of light (collimated light) and properties of the transparent object (absorption, ...), they can reconstruct the 3–D shape of the transparent object. For each relative position of the object and light/camera setup, the method computed a two dimensional projection of the 3–D refractive index field. More positions can provide the data for tomographic reconstruction of the transparent object. The example of the data is shown in Fig. 3.20.

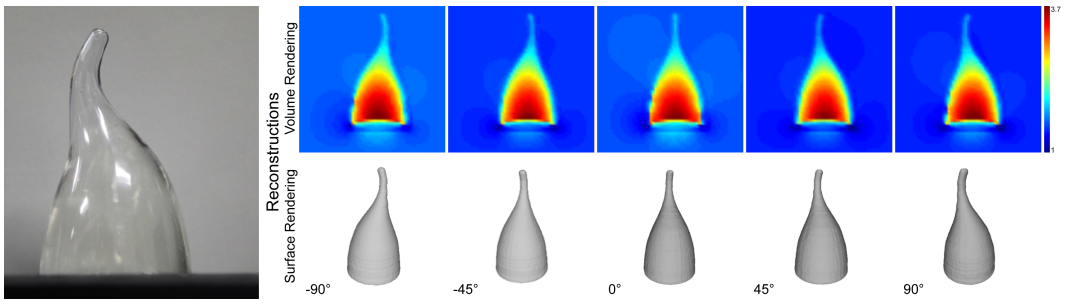

Figure 3.20: 3–D reconstruction of a transparent object. Seven pairs of images were captured to obtain the reconstruction. [113]

3.9 Analysis of the cut stones appearance

Cut gemstones and artificial stones are of wide interest to both experts and the general public. As their cost is a very important characteristic, there is a specialized industry for evaluating their financial value. The aim is to evaluate the cut gemstone price based on the objective criteria starting from physical qualities such as their weight, up-to the more subtle quantities such as fire or brilliance.

The information about such systems is mostly found in patent literature and specialized journals. The Gemological Institute of America is one of the institutions hosting such efforts as can be documented by plenty of patents by Ilene Reinitz, T. Hemhill, James Shigley, Jose Sasian, etc.

Their work consists mainly of translating many terms used in gemology such as fire and brilliance into the exactly defined physical quantities, which can be measured on physical samples or calculated from computer models. They use ray tracing methods of computer graphics for evaluating these quantities on the computer models. They also try finding the function of the variables which can be used for estimating the value of a particular stone. In a simpler version, they just present the calculated values of the quantities to the expert.

Typical patent publications from this field are patents [154, 155] by Reinitz et al. They define, e.g. dispersed color light return (DCLR) as

$$D = \sum_{\lambda} \sum_{r_i} A_i \sigma_i W_i \,, \tag{3.1}$$

where D is a DCLR, first sum is over all wavelengths (λ), second sum is over all rays involved r_i, A_i is an area of the ray, σ_i is 1 when the power density of the ray is above threshold and 0 otherwise, W_i is the weighting factor depending on the angular position of the ray.

The overall exactness of the approach is not high as it is influenced by several factors:

- One can observe this approach only in more or less marketing materials in the specialized but not scientific journals or in the patent literature, which has its own and limited language.

- Generally, the knowledge is considered a 'know how' by the authors so they avoid exact description of what they really do (see Fig. 3.21).

- Computer graphics-based methods are mostly used as the tool, which visualizes the result into bitmaps, uses "sample-based" ray tracing methods, etc. These approaches just approximate the calculations of exact variables.

More patents are mentioned in Chapter 4.

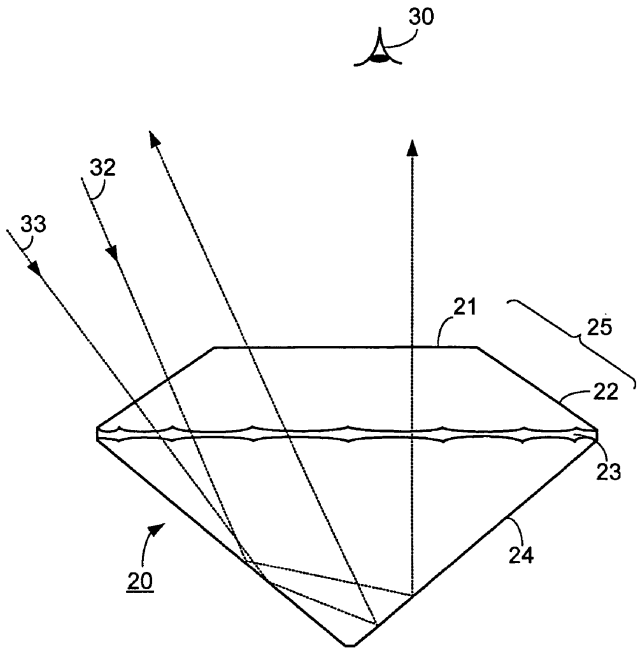

Figure 3.21: Typical image from the patent literature, the ideas regarding physical setup is easily extracted from the literature, the underlying mathematical ideas are either hidden or presented in very complicated manner which effectively prevents their presentation. [160]

3.10 Detection of transparent objects for manipulation purposes

The transparent objects are frequently present in robotics scenes. For example in household scenes, the presence of glasses, bottles, jars etc. should be either avoided, i.e. considered as obstacles, or even manipulated. The required accuracy of determining the position is not high. It is typically limited by the sensors available for detection. Some methods avoid exact reconstruction of transparent objects and just try to detect regions of space where the simple Lambertian model is not satisfied and where the measurements from several directions are not compatible.

Klank [106] used a time of flight camera, which is not capable to measure directly the surface of the transparent, specular objects. As the rays are refracted by the transparent material, they offer highly deformed shape of the opaque background. Such reconstructions from several viewpoints are inconsistent and contours of the transparent objects can be approximately reconstructed. The input data for the method are shown in the Fig. 3.22.

The similar approach is used by Lysenkov et al. [112]. They used Kinect range finder which again failed on transparent objects. The scene analysis started with the range image where transparent objects are typically not measured. They recognized the types of the objects in the scene from the color image (cups, glasses) using the

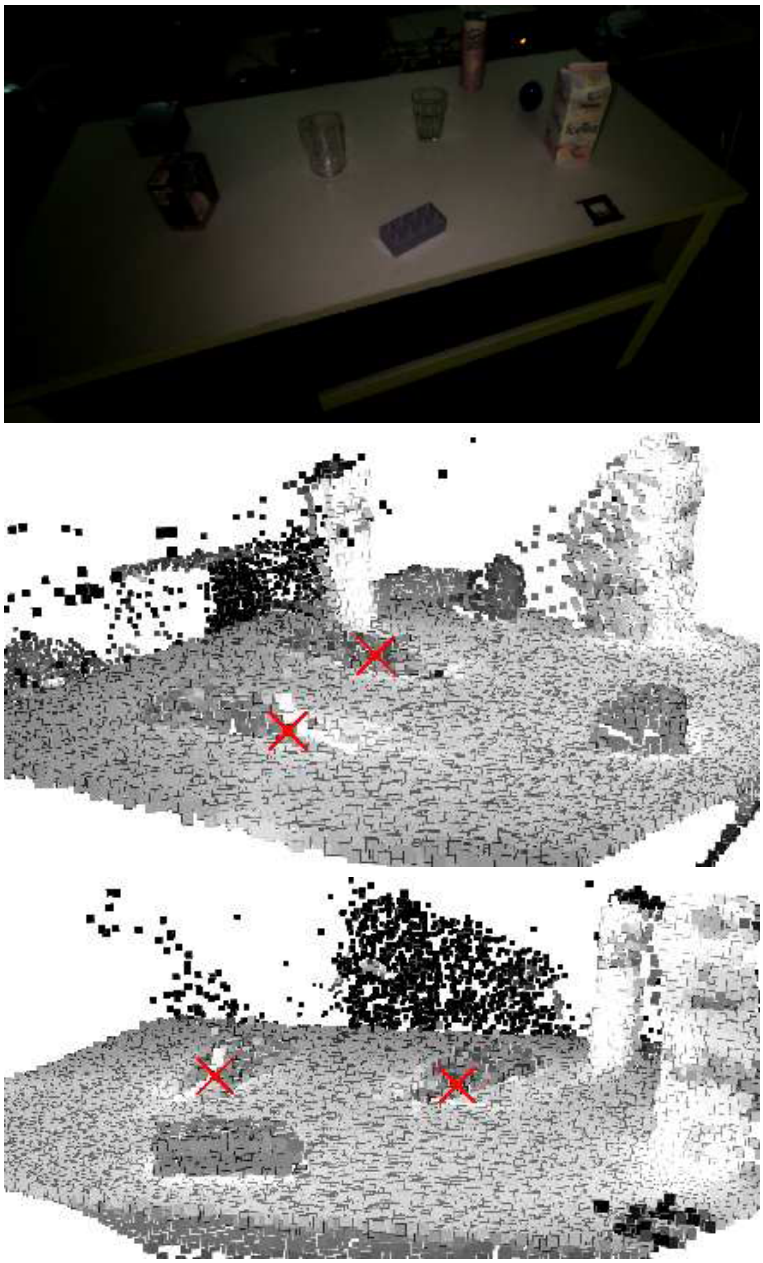

Figure 3.22: Top: The image from the ordinary camera. The transparent cups are standing in the middle. Middle and bottom: The left and right images from Time of Flight camera do not measure the shape of the glasses but they also do not measure correctly the shape of background. The surface behind the transparent cup seems to be closer than its real position in the scene. The cups are labeled by red crosses. The inconsistencies between these two images can be recovered to obtain the information sufficient for grasping the plastic cup. [106]

information from the beforehand prepared database. The pose of the recognized objects was estimated using some prior knowledge like the cup is standing on the desk, etc. The input images from the Kinect sensor and the determined positions of the transparent objects are shown in the Fig. 3.23.

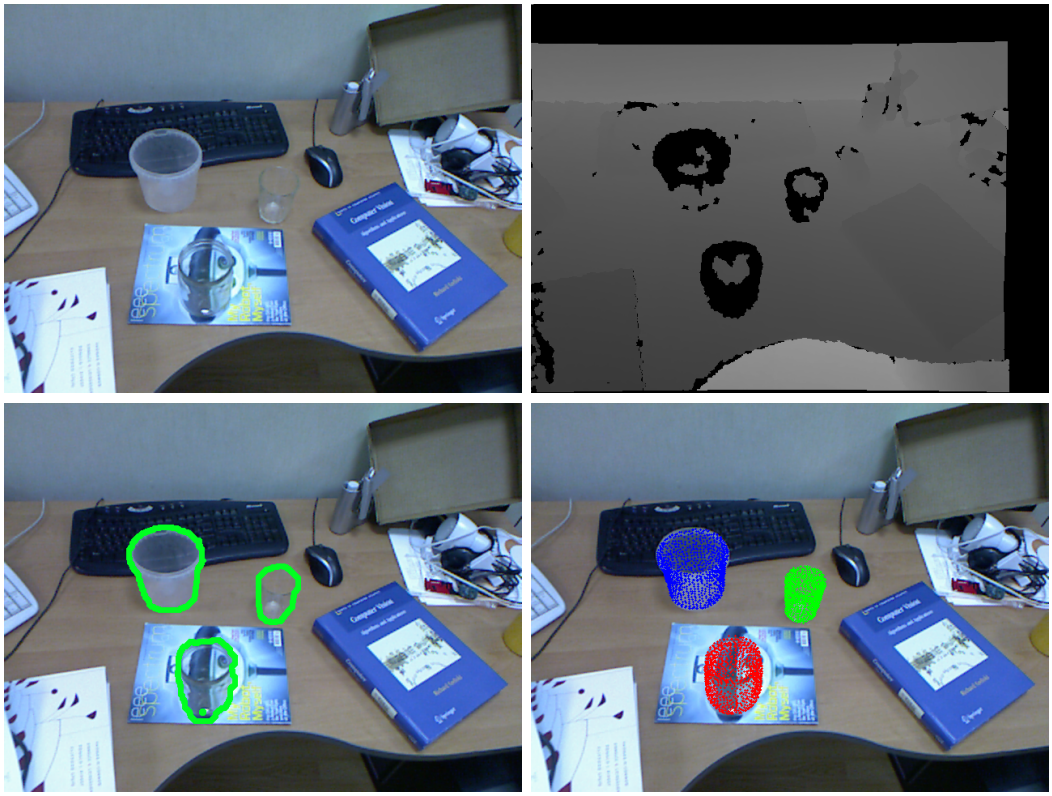

Figure 3.23: The scene with transparent objects. Top left is RGB image and top right is the depth image from the Kinect sensor. In the bottom left, is the segmented image of transparent objects. Bottom right shows the estimated pose of the transparent image as projected to the color image of the scene. [112]

The Kinect data from several views of a static scene were used by Alt et al. [73]. The inconsistencies, that is the depth data which cannot be matched to the data from another view by Euclidean transformation, were detected. Very rough estimate of the transparent part of the scene was then built.

3.11 Conclusions

Although the papers presented here refer to themselves as dealing with transparency, they mostly do not deal with it:

1. **Painting of objects** is a good engineering solution but it cannot be used in many applications [87, 78].

2. **Change of the wavelength** [91, 90] to make an object non-transparent is also an engineering solution.

3. **Observing hot particles** [98] offers impressive results but with very limited applicability in general situations.

4. **Adding agents for photo-luminescence, phosphorescence or chemiluminescence** [101] can be used only under special conditions.

5. **Translucent objects** [96] are a broad class of objects but they are not transparent.

6. **Interferometry** [177] relies on the first surface reflections.

7. **Mirroring objects** [169] can be reconstructed by method which is a modification of that for objects without diffuse component of reflected light.

The reconstruction of transparent objects can be solved in different ways:

1. **Tomography** based on Radon transform [171],

2. **Analysis of polarization** [156, 123, 121, 122] allows to reconstruct objects assuming the known shape of the back side of object.

3. **Laser range finding using exhaustive scanning** [135, 134, 132, 133] is a modification of the standard method for objects without a diffuse component of the reflected light.

4. **Direct triangulation** [110, 109] is useful when we have full knowledge about incident and exiting rays and the number of reflections or refractions is limited.

5. **Triangulation and optimization** [175, 77] relaxes the assumptions needed for direct triangulation, the optimization step allows to solve unconstrained problem.

6. **Scatter trace photography** [126] seems to be one of the most general methods regarding the class of objects it can handle. Lot of data are captured to allow reconstruction.

Chapter 4

Our Previous Work

This chapter provides an overview of our practical, industrial efforts related to the thesis. The R&D work was motivated by the industrial demand and spanned over several years. The outcome was a series of machines designed, produced, and explored in the industrial mass production of jewelry cut glass. These activities stimulated also a more theoretical striving, which are presented in coming chapters of the thesis.

We were motivated in our design of measurement methods by the scenario sketched in Fig. 4.1. The products are manufactured according to the object model in a human controlled world. Such a model is usually a CAD drawing. The object is fabricated by a manufacturing procedure. This object is checked by a measurement process and the results are measurements. The measurement process can be modeled too, which yields modeled measurements. The discrepancy between the measurements and the modeled measurements provides a feedback which can be explored, e.g. for improving the:

1. **Measurement process** adjustments. The agreement of the measurement process with expectations or results of independent methods is optimized here. A new or an improved measurement process is being developed. The measurement model is often improved simultaneously.

2. **Object model** adjustments. The discrepancy is minimized by modifying object model parameters. The result of this process is the object model, which matches the given object best.

3. **Realization parameters** adjustment. One can minimize the discrepancy by adjusting the manufacturing process so that object is manufactured according to object model with the high fidelity.

Our previous work can be divided into two main directions. The first direction is directly related to understanding the light propagation in transparent objects such as cut stones in the jewelry industry. We studied light propagation aspects in the stone. We also dealt with calculating the physical variables correlating with the market value of stones. The work was inspired by [153]. We significantly extended the original idea [145, 82]. We also studied, how to change the shape of stones to obtain better

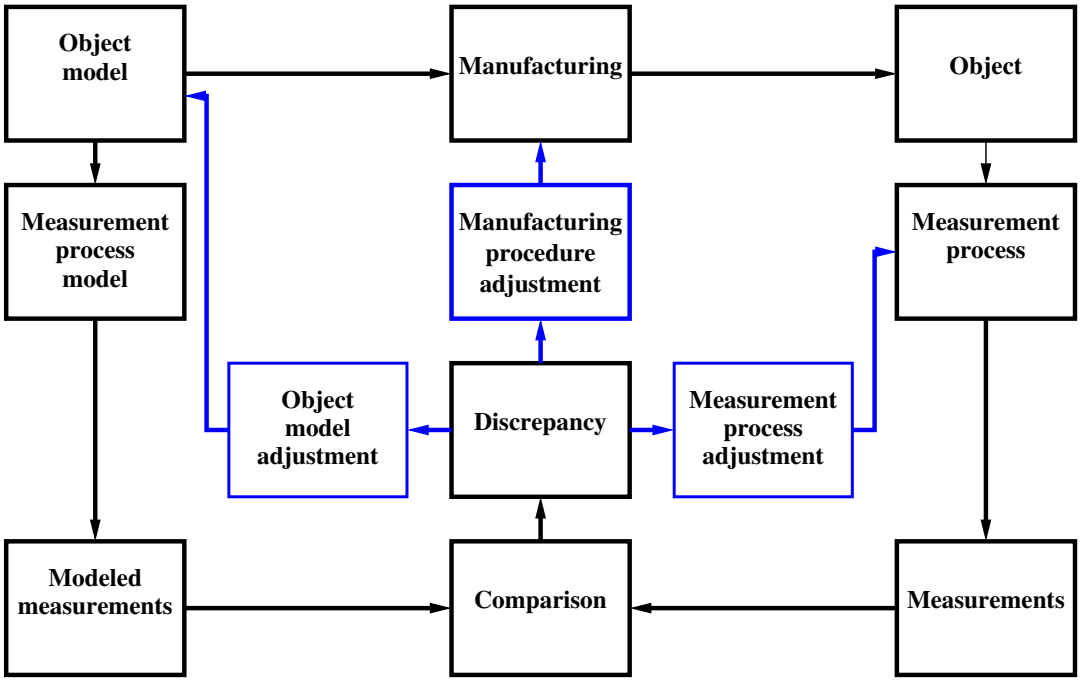

Figure 4.1: Scenario of measurement in a human controlled world, e.g. in the industry.

optical properties. We were able to increase the variable "fire" of the diamond shape cut of cubic zirconia stones. We developed a tool enabling the manufacturer to design the "star" cut [149, 107].

In the second direction, the optics of the vision system is designed intentionally to avoid rays passing through objects, see Sec. 4.5.

4.1 Modeling of light passing through cut stones

We modeled the path of the collimated light beam through a convex polyhedron of the known shape and the index of refraction [145], see Fig. 4.2. The size of screen is assumed large compare to stone size. The developed system can model multiple wavelengths at the same time.

The extended version of the work [82] enables a powerful visualization of the beam propagation through the stone and its analysis as well, see Fig. 4.3. The work also incorporates polarization effects.

Assuming the collimated light beam and the convex polyhedron allowed the efficient implementation of the light propagation. The modeling output is a set of collimated light beams exiting the modeled object including its complete path through the object. Each output beam is accompanied by the information about the sequence of facets which refracted or reflected it, the last facet it passes through, the direction of the beam, the beam intensity, and its polarization. See Fig. 4.4.

The model of the transparent polyhedron and light passing through the object is based on the following assumptions:

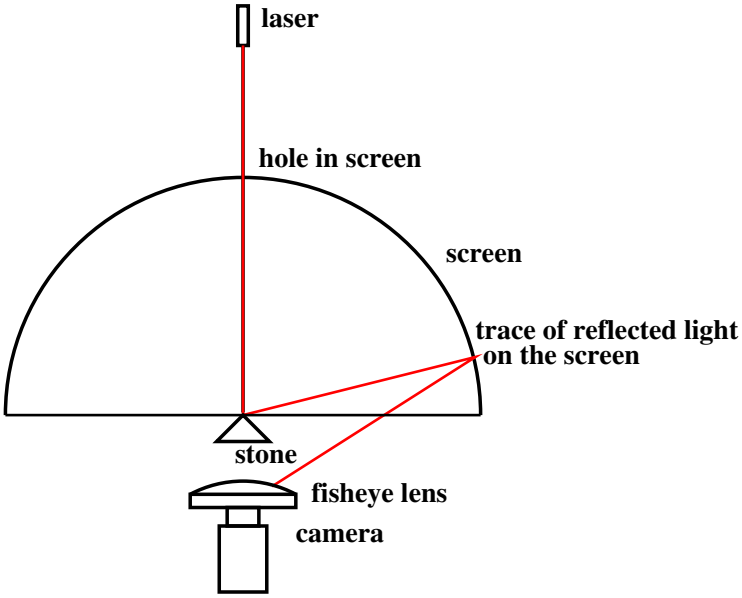

Figure 4.2: The scenario of the forward task simulation. The collimated beam, produced by a laser here, is incident to the stone. The light beam is many times reflected on/in the stone and refracted to/from the stone. Many lower intensity beams are produced. Those beams fall onto the hemisphere of the screen, which is observed by the camera. The arrangements of the screen and the camera can be different, e.g. planar screen, the screen above or bellow of the stone, ... [145]

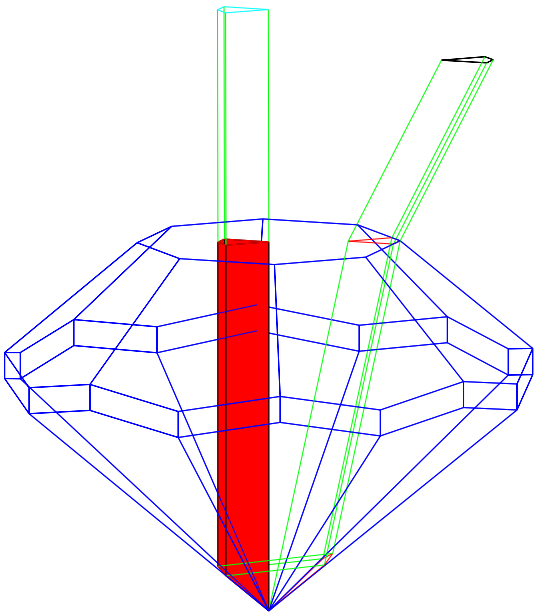

Figure 4.3: Visualization of the beam path through the object. The object is the polyhedron. The beam is a pencil of collimated light rays. The image is three-dimensional and can be manipulated in MatLab SW package. [83]

1. The object is **transparent** with the known index of refraction. Several discrete light wavelengths can be modeled at the same time. The system cannot model light with continuous wavelengths. This is a principal assumption. It is related to difficulties in modeling continuous processes digitally.

2. The studied object is represented by the **polyhedron**. This is a principal restriction of the approach. We would like to slightly relax this assumption in the future work.

3. The object is **convex**. This is not a principal restriction but it allows to speed up calculations. The extension of the approach to non-convex objects is possible. The cut stone of our interest are convex anyway because of the grinding process involved.

4. The **environment** has known a index of refraction for each used wavelength. The air is the most common environment.

5. The entering and the exiting light is modeled by a **collimated beam** with a polygonal cross-section and the uniform light intensity. The light beam is represented by its cross-section (polygon in space), direction (vector in space), intensity, wavelength (index of refraction of the object material), state of the polarization (Stokes vector).

The system reflects the physics of the light propagation accurately within the field of geometric optics, wave optics of planar waves, and radiometry. When real properties of objects are considered, the system simplifies the reality mainly in the following aspects:

1. **Planarity**
   Planarity of surface polygons is generally restrictive. Our intention is to relax this assumption slightly by assuming, e.g. a spherical surface with a low curvature.

2. **Sharp edges between faces**
   Experiments showed that it is difficult to manufacture very sharp edges when the objects are very small.

3. **Smoothness of the surface**
   Our model does not reflect scratches or the surface micro-structure. Current observations do not indicate that assumption about smoothness of the surface is a real restriction.

The modeling of the light trajectory in transparent objects, presented in this section, is a forward task. The light source is known and light propagates on each surface involved according to Fresnel equations, see Sec. 5.4. Polarization is solved by the Mueller calculus, see Sec. 5.5.

4.2 Calculating appearance of transparent objects

We made an excursion into to the field of computer graphics in [107]. Using the standard tool POVRay [147] we modeled jewelry stones and the particular illumination setup. We created an optimization algorithm which optimizes appearance of the stone by changing its shape [149].

The system calculates the image of the stone under the special illumination using POVRay. Its image is compared to the image required. The difference is minimized by changing a set of parameters which define the shape of the stone. Standard non-linear optimization is used.

The "star" visible in stones is a proof of the stone high quality. The "star" appearance is very sensitive to the shape of the stone and the curvature of its facets.

The similar approach was patented by Sasian et al. in [160, 157, 158, 159] in the same year. Sasian uses the model of the stone and certain arrangement of lights for ray tracing views on the stone. The visualizations are used later for evaluating the gemstones by humans, similarly to our work. Sasian proposes the ray tracing simulation only in the forward direction for the determining stone cut appearance and quality. We used it in the feedback to design required appearance.

The automatic evaluation of the proposed shapes of the cut developed by Blodgett et al. [79, 80, 81, 172] enables the feedback for designing optimized cuts for a particular material. For the cut grade evaluation, the system compares the evaluation of the particular set of cut stones provided both by human experts and by the computer simulation. Blodgett uses features adopted from the human description of the stone. The similar approach was used by Verboven [173] for evaluation of the stone clarity.

4.3 Evaluating the impact of the facet surface modification

The modifications of the facet optical properties can have both positive and negative effects on the stones appearance. The negative impact is studied in our work [164], which analyzes the effects of laser marking of some facets. The study was written on the request of the industrial customer and its content is confidential.

The positive influence of the surface modification is presented in patents by Maltezos and Scherer in [115, 116]. They propose the fine grating or structuring of some facets to improve fire and scintillation of the stones.

4.4 Reconstruction of polyhedral objects using strong prior model

We deal with the forward task, which calculates the propagation of light in known objects. The inverse task finds object shape having the information about light exiting the object under the known illumination. The inverse task is ill-posed similarly to many other computer vision tasks.

We attempted to solve the inverse task using the strong prior model in [83]. The task is the following. Assume a CAD model of a polyhedral object. The collimated beam of light illuminates the object. The exiting beams are measured (see Fig. 4.4). The experimental setup is shown in Fig. 4.5 and 4.6. The path of the light through a cut stone is modeled. Exiting beams are calculated using the forward task. We assume that the difference between the measurement and the modeled measurement is caused by the difference between the object shape and the model. We attempt to adjust model parameters using the optimization algorithm, which provides the best match between the measurements and the modeled measurement.
This approach generates many questions:

1. What is the (best) criterion for evaluating the agreement of the physical and the computer simulation?

2. How to optimize hundreds of parameters efficiently while having a relatively slow algorithm evaluating the criterion?

3. How to match spots of light on the screen to the list of outputting beams of the computer model? This is an instance of the correspondence problem. The number of outputting beams is rather large. Due to the sensitivity of the direction of the beam to the object parameters, the geometrical position of the spots is not sufficient for solving this correspondence.

   We have contributed to the correspondence problem at Chapter 8.

4.5 Measurement of transparent and translucent objects via optical elimination of transparency

The understanding of light propagation in transparent objects significantly helped us in developing machines, which handle transparent objects, measure their dimensions and shape, inspect their quality, and classify them accordingly.

One approach to measuring dimensions of transparent objects is to eliminate the transparency using a specially designed optics.

A transparent object is placed between the telecentric source of light and the camera equipped with a telecentric lens. Only rays which are parallel to the optical axis at the output of the object will pass to the camera. In such an optical setup, the light passing around the object will result in a bright part of the image. Most of the object will appear dark in the image. Certain parts of the transparent object will still enable the light to pass. The example is the part of the object consisting of two parallel planes. See Fig. 4.7.

4.5.1 MesCut

MesCut [139] is a system for measuring 2D dimensions of cut stones from a single view (see Fig. 4.8). The system uses telecentric illumination described above. The input image is bright in regions around the stone and dark inside the projection of the stone. Some rays passing through the stone are parallel to the optical axis and thus reach the

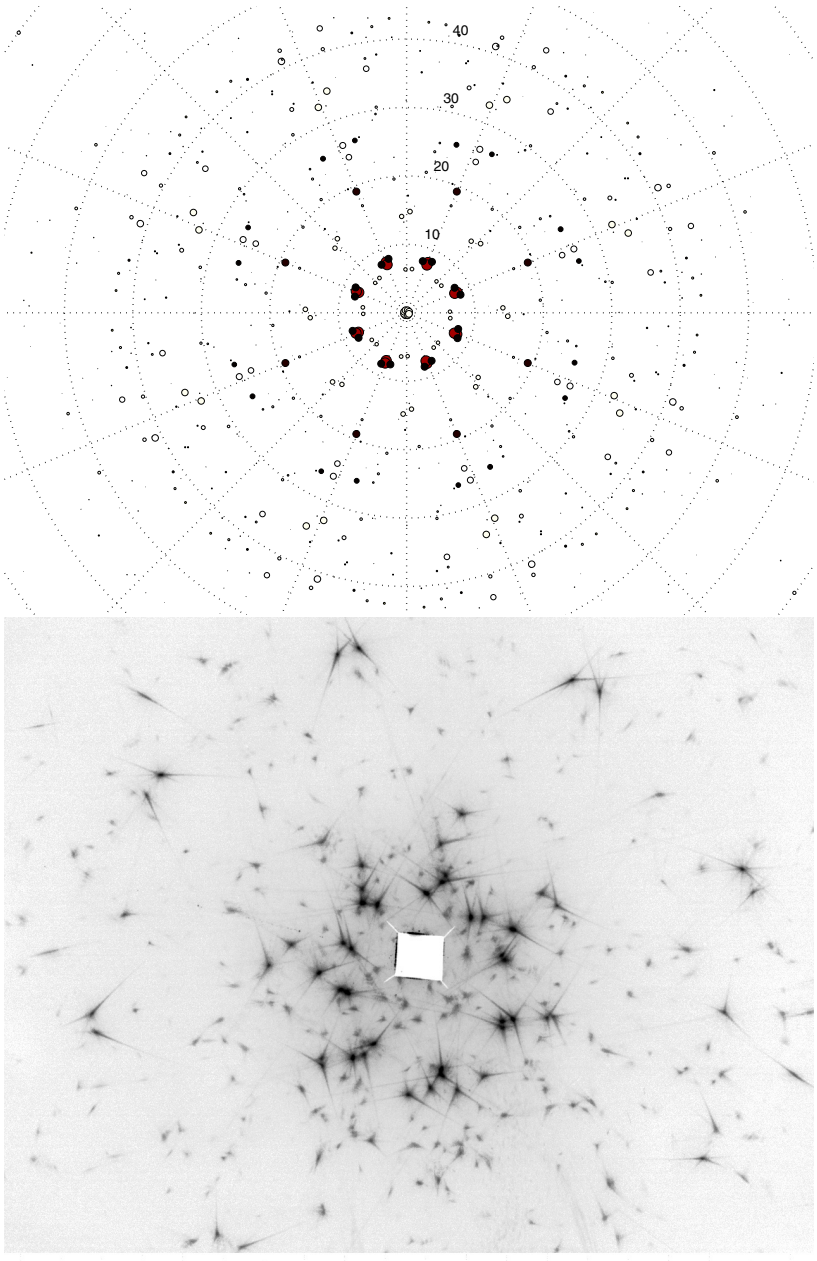

Figure 4.4: Top: The visualization of the modeling result, in which the light beam propagates trough the polyhedral object (chaton). The chaton is a relatively simple stone with just 17 facets. The figure shows output beams, their intensity (coded as the inverse brightness of spots), their cross-section area (coded as the area of spots). The results are drawn in polar coordinates, where the radius codes the elevation and the angle codes the azimuth of the output beam. All exit beams with up to 10 internal reflections are shown. Bottom: The experiment with the chaton. The image shows the beams coming from the object illuminated by the laser. The image brightness is inverted for the better impression of the human observer. The center of the image is physically masked out disabling the direct laser light to hit the camera chip. Compare to the Top. [83]

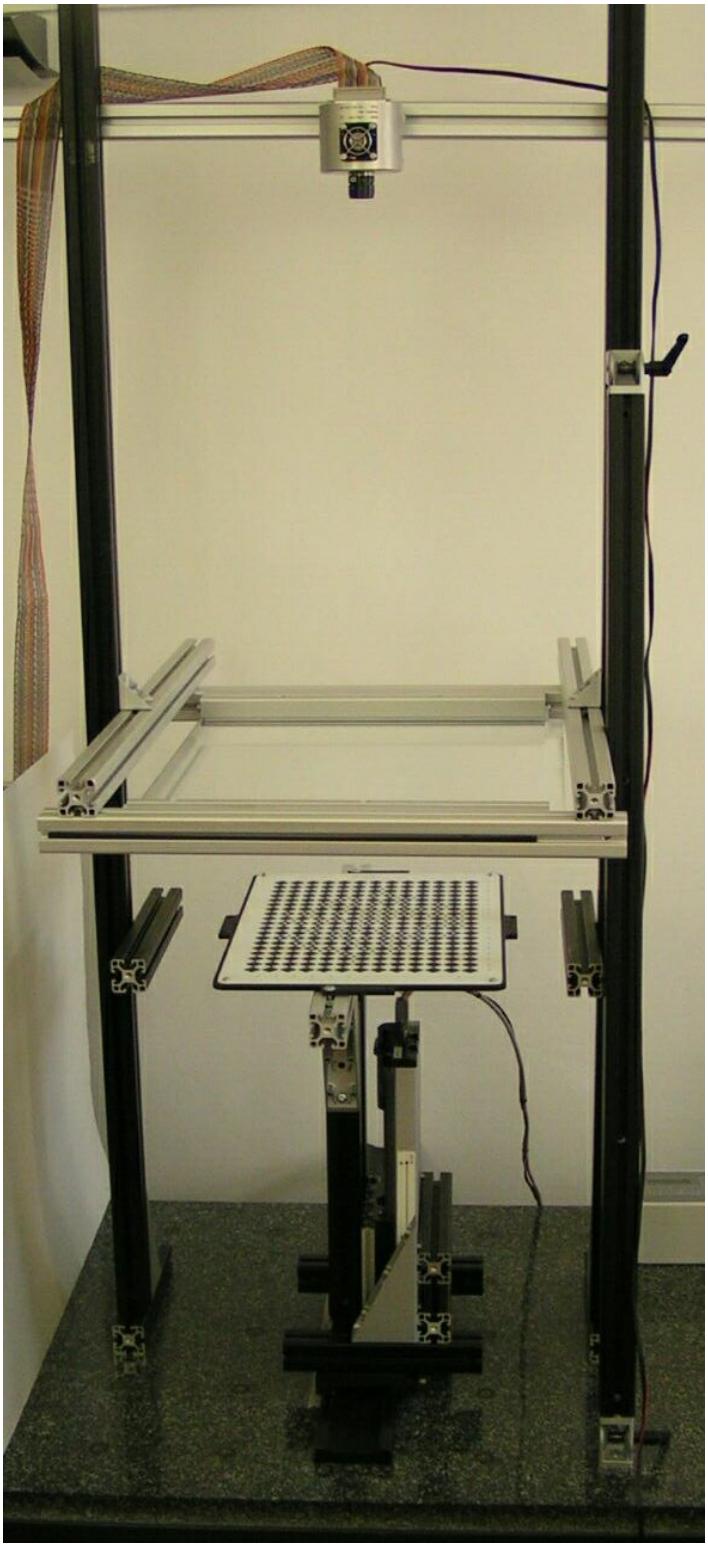

Figure 4.5: Experimental setup for capturing the output beams coming from the object illuminated by the laser beam. The overall setup during calibration. [83]

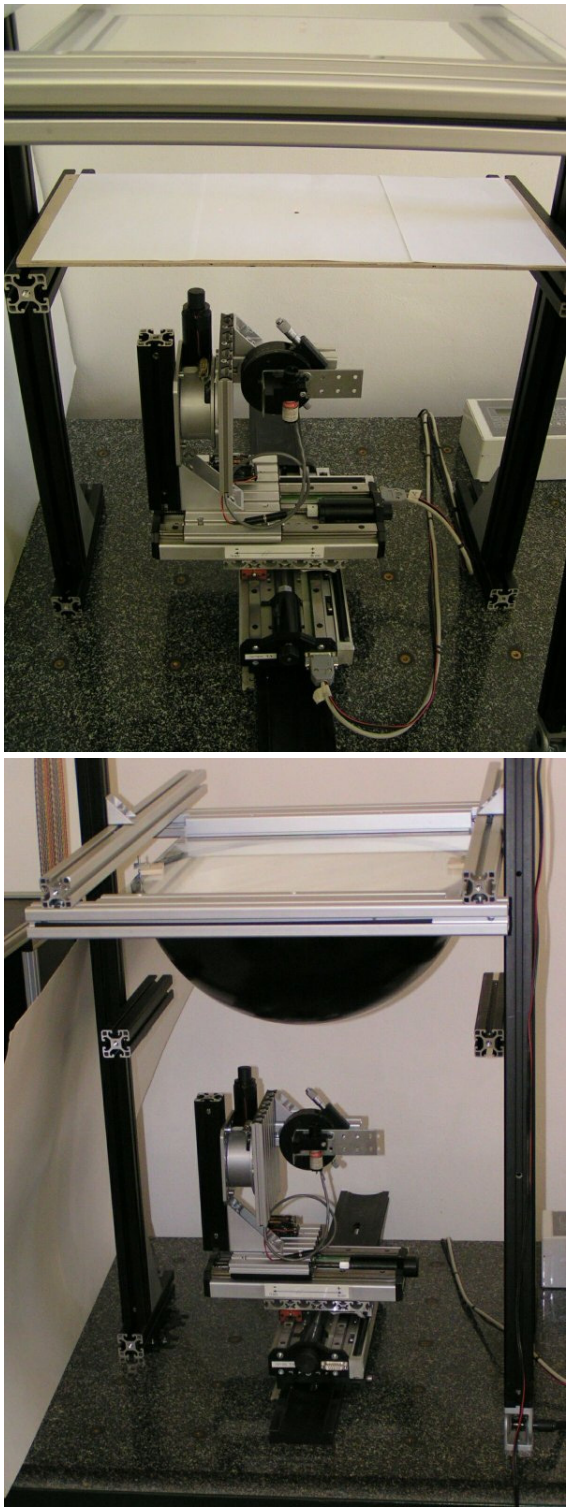

Figure 4.6: Experimental setup for capturing the output beams coming from the object illuminated by the laser beam. Top: The laser mounted on the adjustment table in the bottom part; the planar screen in the middle, glass for placing the object in upper part. Bottom: half spherical screen. [83]

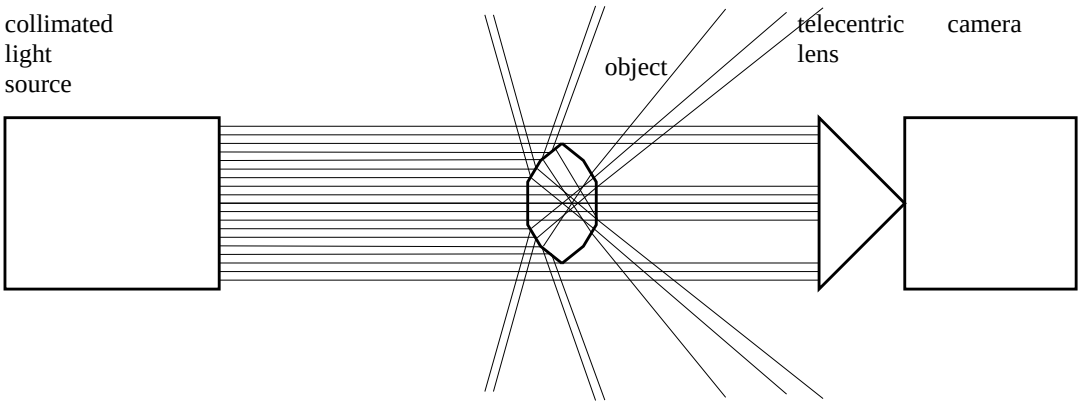

Figure 4.7: Telecentric optics. Using telecentric optics, most rays from the light source are reflected or refracted out by the object or the screen out by the lens aperture.

camera chip. The processing of a profile projector image allows the highly accurate dimensions measurement. The accuracy measurement of angles between facets and edges is lower due to their short length.

The 2D measurement is sufficient in this application for assessing the overall shape of the stone due to the special orientation of the object during measurement. The orientation is ensured by a mechanical holder.

4.5.2 SortCut

SortCut system, also developed by Neovision, is similar in handling of transparency using telecentric optics. The images of a measured stone (see Fig. 4.9) are captured from several angles and important dimensions are recovered. The system can measure and sort up to 15 stones per second. The mechanical positioning of the stones is again essential for measuring meaningful 3D dimensions out of 2D projections.

4.5.3 Helios

Helios [138] system goes farther in the recovery of the 3D shape of polyhedral objects from sequence of 2D images (see Fig. 4.10). The polyhedral transparent or opaque object is placed into the telecentric optics as above. It is rotated around known axis of rotation and some hundreds of images with known rotation angle are captured. Basically the projections of polyhedron edges are measured in individual images. The complete 3D shape of polyhedron is then recovered from captured data.

4.5.4 GlassDrop

GlassDrop [137] system uses different approach for measuring the glass shape (see Fig. 4.11). The measured glass is hot and thus radiating in the visible spectrum. A camera captures the image of the hot glass. The contour of the drop projection is measured in the image. The glass shape is supposed to be radially symmetrical.

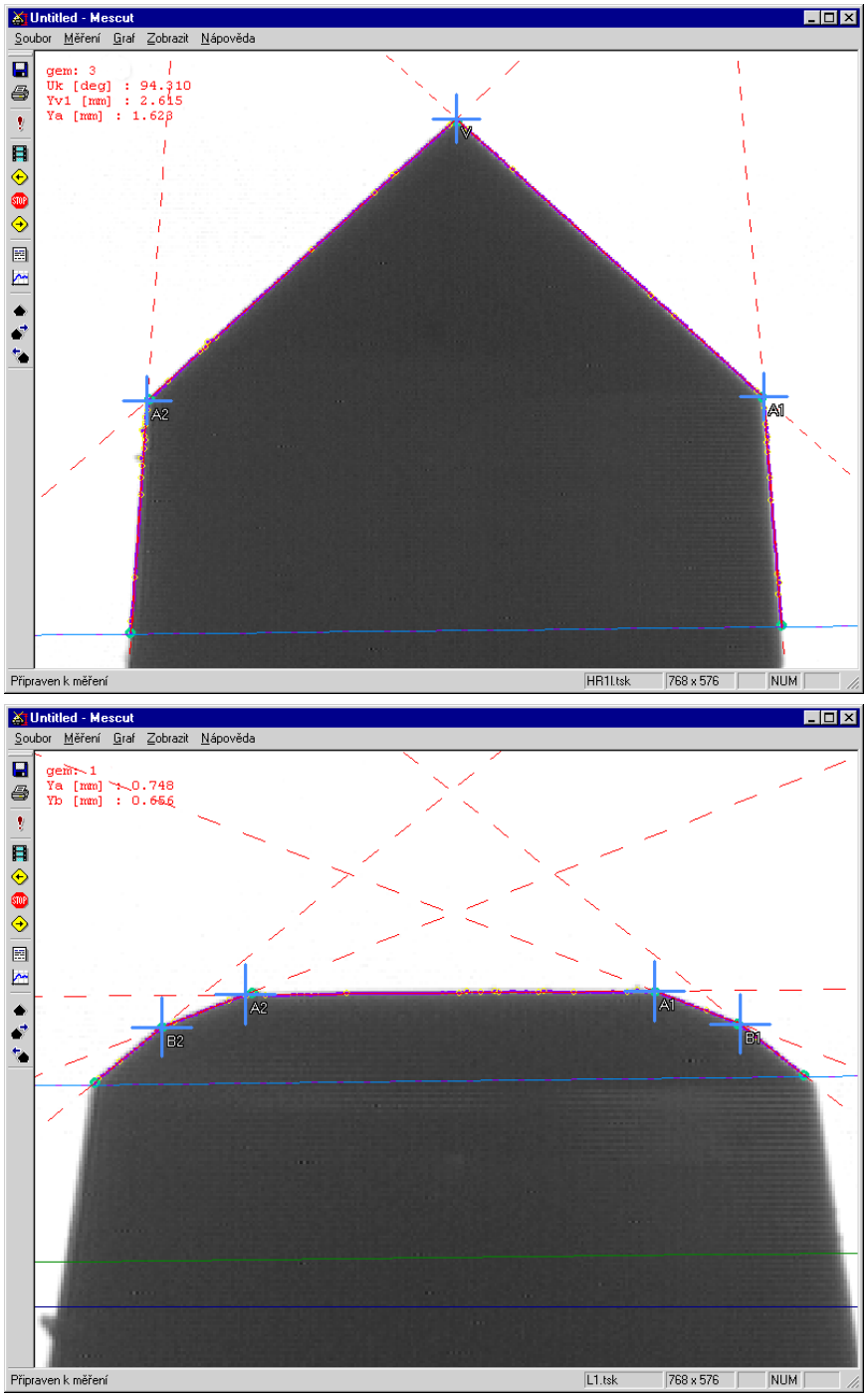

Figure 4.8: Processed images from MesCut system. Courtesy of Neovision s.r.o. [139].

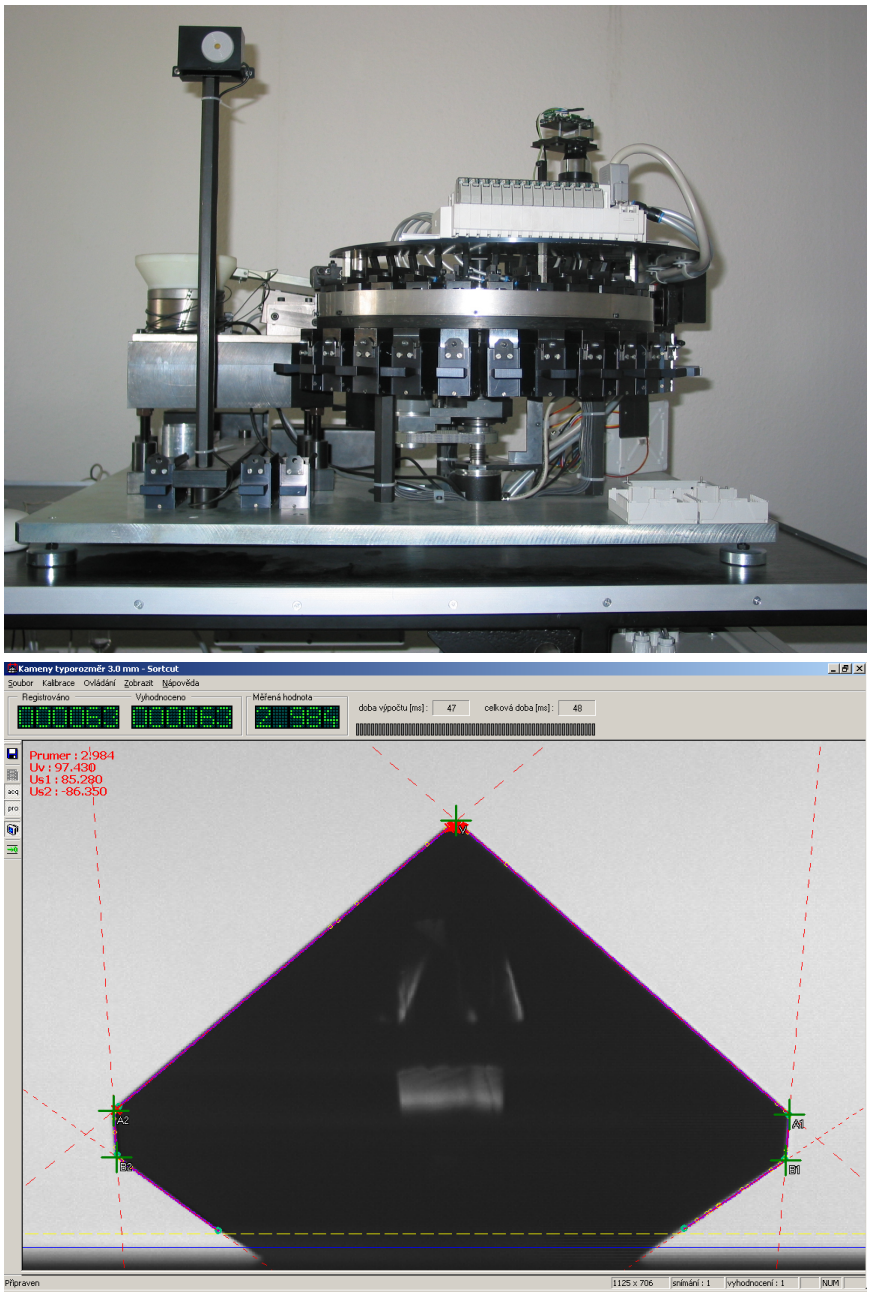

Figure 4.9: SortCut machine. Processed image from SortCut system. Courtesy of Neovision s.r.o. [140].

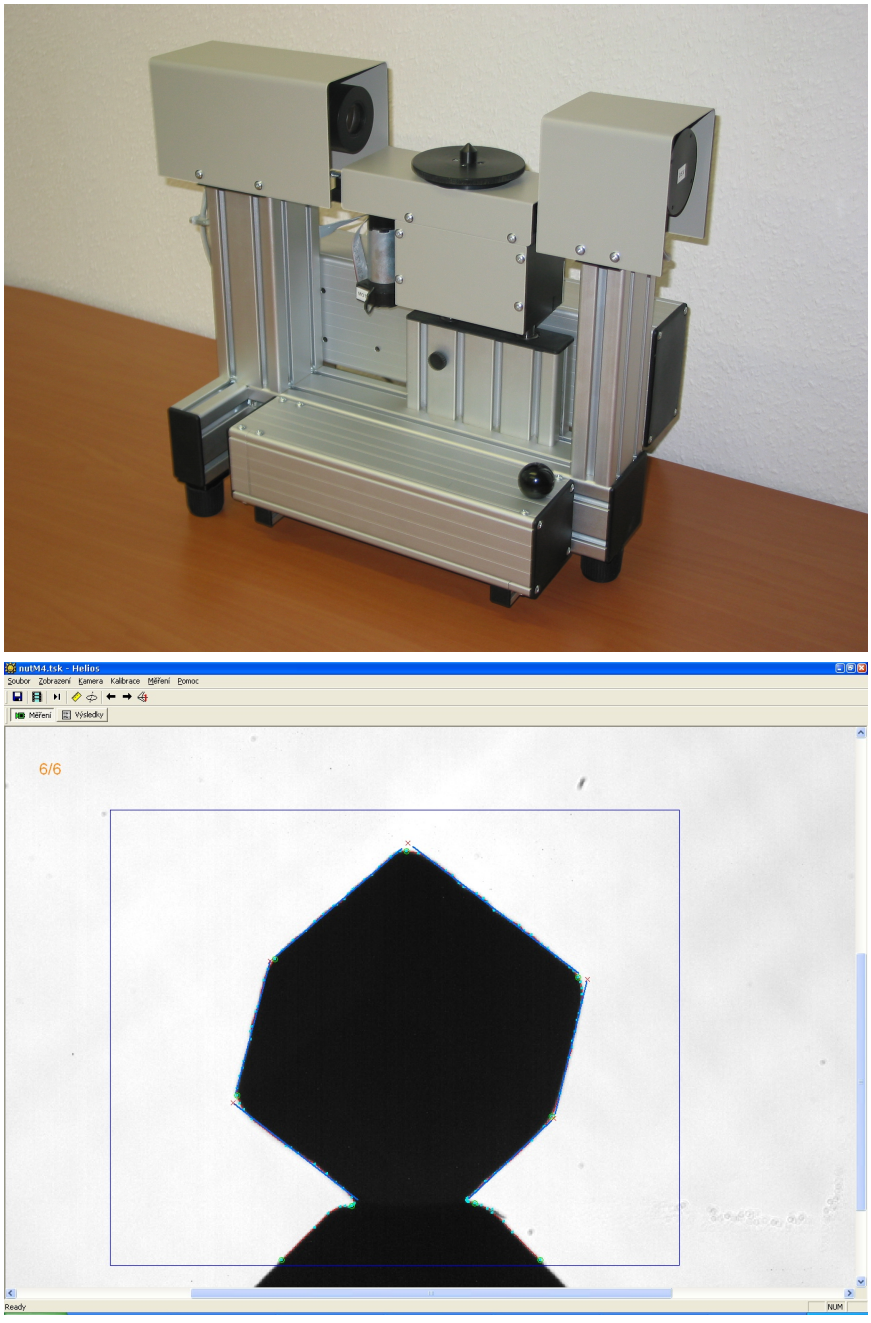

Figure 4.10: Helios measuring machine. A processed image from Helios system. Courtesy of Neovision s.r.o. [138].

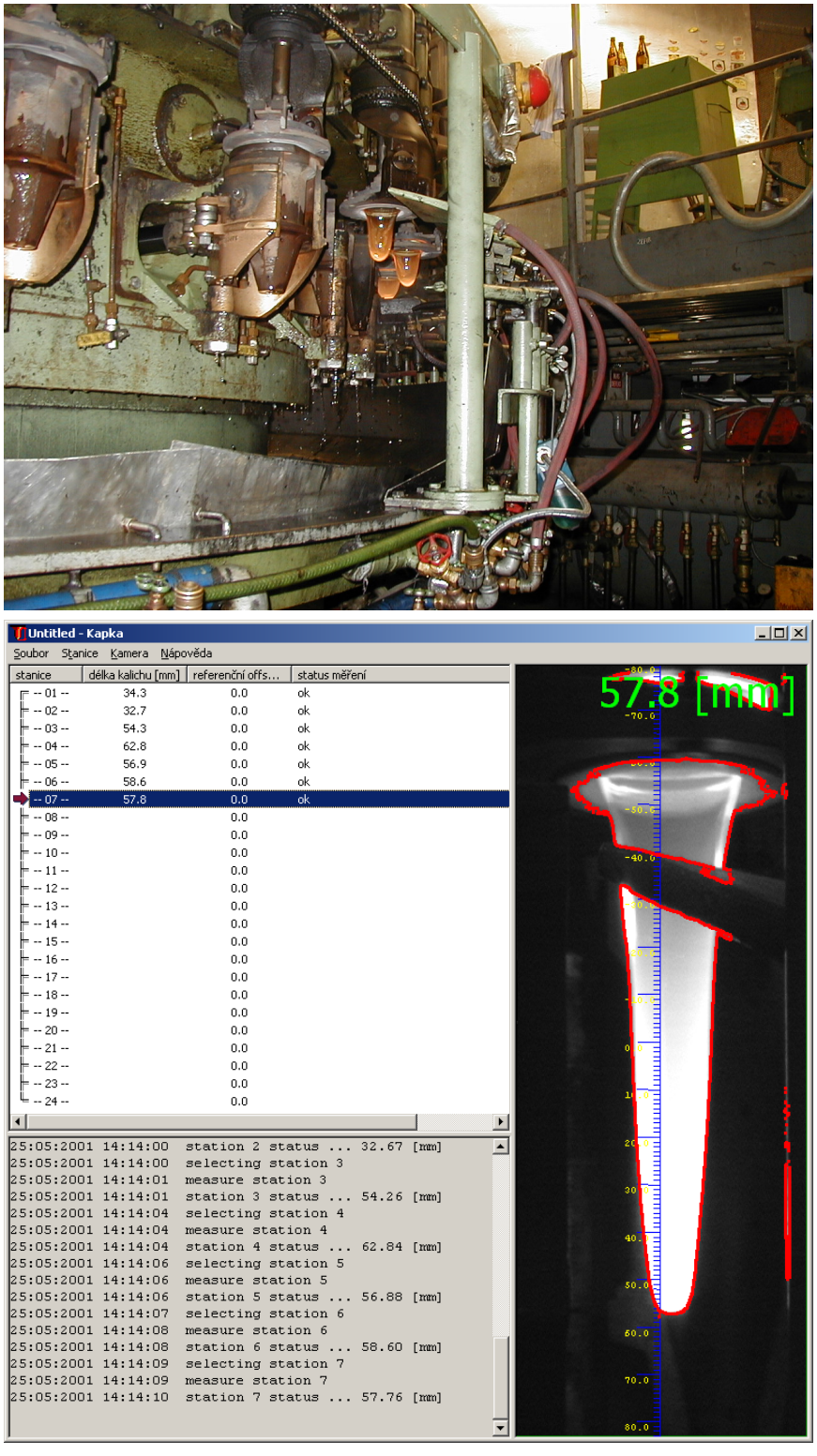

Figure 4.11: Machine for manufacturing drinking glasses. Processed image from Glass-Drop system. Courtesy of Neovision s.r.o. [137].

Chapter 5

Theoretical Background and Notation

This chapter provides the terminology and concepts, which will be used in thesis. The concepts listed and reviewed here were taken from the established literature [85, 76, 94].

5.1 Terminology

Ray - an oriented line in the direction of light propagation specified by:

- a direction vector of a unit length,
- a point on the ray,
- a Stokes vector [85] describing the intensity and polarization state of the ray.

Beam - a compact convex set of collimated (parallel) rays with a polygonal cross-section, called base, specified by:

- a direction vector of a unit length,
- coordinates of the base vertices,
- a Stokes vector describing the intensity and polarization state of the beam.

Facet - a planar convex polygon specified by:

- coordinates of the polygon vertices,
- a normal vector of a unit length,
- refraction indices on both sides of the facet.

Stone - a convex polyhedron bounded by facets. It is described by:

- facets,
- refraction index of the stone material.

Screen - a surface, on which the beams emitted from a stone fall. The screen can have various geometry, it can have planar, hemispherical, or other shape.

Trace - a light spot on the screen caused by beam or ray exiting from the stone.

Incident ray vector: $\vec{v}_i = \begin{pmatrix} v_{ix} \\ v_{iy} \\ v_{iz} \end{pmatrix}$, $\|\vec{v}_i\| = 1$.

Reflected ray vector: $\vec{v}_r = \begin{pmatrix} v_{rx} \\ v_{ry} \\ v_{rz} \end{pmatrix}$, $\|\vec{v}_r\| = 1$.

Transmitted (refracted) ray vector: $\vec{v}_t = \begin{pmatrix} v_{tx} \\ v_{ty} \\ v_{tz} \end{pmatrix}$, $\|\vec{v}_t\| = 1$.

Facet normal vector: $\vec{n} = \begin{pmatrix} n_x \\ n_y \\ n_z \end{pmatrix}$, $\|\vec{n}\| = 1$.

5.2 Concepts from optics

We use the following concepts from physics. We consider a planar wave of light. The light is not coherent. The reflection and refraction occurs on planar surfaces.

The properties related to energy of the light wave are represented by the amplitude of its electric vector. The Stokes vector of electric amplitudes is used for polarized light. When we consider the power of light incident on the facet or stone, we use radiometric variables like the irradiance and the radiant flux. The radiant flux for the polarized light is arranged into Stokes vector of corresponding radiant fluxes.

We assume the surrounding material (typically air) and the stone material being dielectric materials.

We assume monochromatic light as the refraction index depends on the light wavelength. The dependency of the refraction index on the light wavelength is called dispersion and this relationship is not known explicitly in applications but it is measured experimentally. One can assume a constant refraction index when dealing with white light or sum the results over different wavelengths in case of non-monochromatic light.

5.3 Reflection and refraction on a facet

The formulae bellow can be found in [76].

The equation of light propagation at a boundary (reflection or refraction) is given by Snell's law [76]. The $\vec{v}_i$ stands for the incident beam. The $\vec{v}_o$ stands for the transmitted or reflected ray. The surface normal vector is labelled $\vec{n}$. We assume that

all vectors have unit size

$$\|\vec{n}\| = 1\,, \tag{5.1}$$
$$\|\vec{v}_i\| = 1\,, \tag{5.2}$$
$$\|\vec{v}_o\| = 1\,. \tag{5.3}$$

η_i is the refraction index of the material where incident rays propagate, η_o is the refraction index of the material where exiting rays propagate. The following condition holds [76]

$$\eta_i \vec{n} \times \vec{v}_i = \eta_o \vec{n} \times \vec{v}_o\,, \tag{5.4}$$
$$\sigma(\vec{n} \cdot \vec{v}_i)(\vec{n} \cdot \vec{v}_o) > 0\,, \tag{5.5}$$
$$\sigma = 1 \cdots \text{refraction}\,, \tag{5.6}$$
$$\sigma = -1 \cdots \text{reflection}\,. \tag{5.7}$$

Equation 5.4 defines the relationship between the normal of the surface and the incident and the reflected/transmitted ray. The relationship does not define orientation of $\vec{v}_o$ uniquely. The orientation is determined by inequality 5.5. Note that for the reflected ray one has to use $\eta_i = \eta_o$ as the incident and reflected rays are in the same material.

The both terms refracted and transmitted label the rays or beams which pass through the interface between two materials. We use them as synonyms. The index labeling refracted rays, beams, or waves is t.

5.4 Fresnel formulae

A planar light wave falling onto a planar interface between two dielectric media with different refraction indices undergoes both reflection and refraction. We also suppose that surfaces have optical quality, i.e., they are smooth within the fraction of the light wavelength. The intensity of the reflected and refracted wave can be described by Fresnel formulae [85]. The formulae describe separately what happens to the wave with the polarization in the plane of incidence and in the plane perpendicular to the plane of incidence.

The refraction indices η_1, η_2 belong to the first and second media separated by the surface, respectively. The incident angle θ_i and transmitted ray angle θ_t (see Fig. 5.1) are connected by Snell's law of refraction

$$\frac{\sin\theta_i}{\sin\theta_t} = \frac{\eta_1}{\eta_2}\,. \tag{5.8}$$

Let $E_\parallel$ be the amplitude of the incident light component with the electric vector parallel to the incidence plane. Let $E_\perp$ be the amplitude of the component perpendicular to the incidence plane. The notation for the reflected and transmitted light is $R_\parallel$, $R_\perp$, $T_\parallel$, $T_\perp$. The amplitudes of the reflected and transmitted light for dielectric media can be calculated by the Fresnel formulae as follows

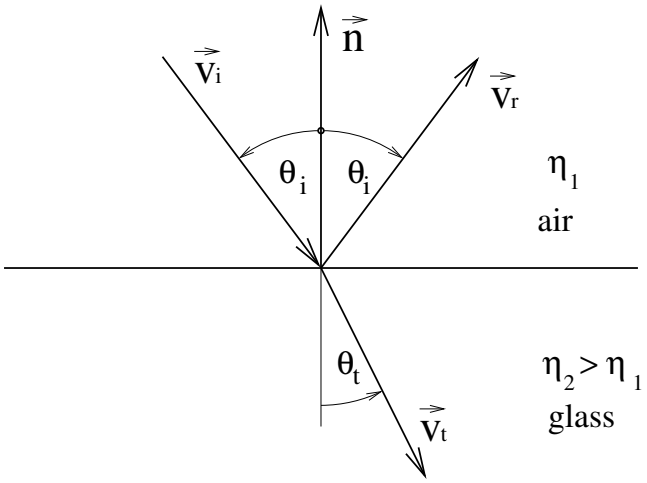

Figure 5.1: Reflection and refraction on a specular surface. The situation for the ray incident from air is shown here. The similar scheme can be drawn for the ray incident from the glass.

$$R_{\parallel} = \frac{\eta_2 \cos\theta_i - \eta_1 \cos\theta_t}{\eta_2 \cos\theta_i + \eta_1 \cos\theta_t} E_{\parallel}\,, \tag{5.9}$$

$$R_{\perp} = \frac{\eta_1 \cos\theta_i - \eta_2 \cos\theta_t}{\eta_1 \cos\theta_i + \eta_2 \cos\theta_t} E_{\perp}\,, \tag{5.10}$$

$$T_{\parallel} = \frac{2\eta_1 \cos\theta_i}{\eta_2 \cos\theta_i + \eta_1 \cos\theta_t} E_{\parallel}\,, \tag{5.11}$$

$$T_{\perp} = \frac{2\eta_1 \cos\theta_i}{\eta_1 \cos\theta_i + \eta_2 \cos\theta_t} E_{\perp}\,. \tag{5.12}$$

One can define reflection and refraction coefficients as

$$r_{\parallel} = \frac{R_{\parallel}}{E_{\parallel}} = \frac{\eta_2 \cos\theta_i - \eta_1 \cos\theta_t}{\eta_2 \cos\theta_i + \eta_1 \cos\theta_t}\,, \tag{5.13}$$

$$r_{\perp} = \frac{R_{\perp}}{E_{\perp}} = \frac{\eta_1 \cos\theta_i - \eta_2 \cos\theta_t}{\eta_1 \cos\theta_i + \eta_2 \cos\theta_t}\,, \tag{5.14}$$

$$t_{\parallel} = \frac{T_{\parallel}}{E_{\parallel}} = \frac{2\eta_1 \cos\theta_i}{\eta_2 \cos\theta_i + \eta_1 \cos\theta_t}\,, \tag{5.15}$$

$$t_{\perp} = \frac{T_{\perp}}{E_{\perp}} = \frac{2\eta_1 \cos\theta_i}{\eta_1 \cos\theta_i + \eta_2 \cos\theta_t}\,. \tag{5.16}$$

5.5 Mueller calculus

Light rays undergo multiple reflections in stones. Reflected beams are partially or fully polarized even when the incident light is not polarized. The Fresnel formulae

calculate separately the coefficient for light polarized in the plane of incidence and in the plane perpendicular to the plane of incidence. Calculation of the irradiance of the reflected beam has to respect that the planar facets of stones are oriented arbitrarily with respect to the incident light polarization. An efficient representation of the reflection and refraction effect on the irradiance and the polarization of the ray is based on the Mueller calculus [165, 94].

Mueller calculus represents each optical object by a single matrix. It can be used only for the incoherent light. The light polarization state is described by Stokes vector [94, 150]

$$\vec{s} \;=\; \begin{pmatrix} E_\perp E_\perp^* + E_\parallel E_\parallel^* \\ E_\perp E_\perp^* - E_\parallel E_\parallel^* \\ E_\perp E_\parallel^* + E_\parallel E_\perp^* \\ \mathrm{i}\,(E_\perp E_\parallel^* - E_\parallel E_\perp^*) \end{pmatrix}, \tag{5.17}$$

where asterisks denote complex conjugation and i stands for the imaginary unit.

The Stokes vector describes the polarized light by four coordinates. The first coordinate is the irradiance of the light. The second coordinate is the difference in irradiances between vertically and horizontally polarized light. The third coordinate is the difference between polarization in the planes rotated by 45° and −45°, respectively, from the incident plane. The last coordinate is the difference between the right and the left circular polarization. The detailed definition including sign conventions can be found in [76].

Mueller calculus allows to calculate the Stokes vector of the light manipulated by the optical component, e.g. polarization filter, as a product of Stokes vector of the light before the change and Mueller matrix characterizing the optical component:

$$\vec{s_o} \;=\; M\vec{s_i}\,. \tag{5.18}$$

The reflection, refraction, or the impact of other types of filters on the planar wave (=beam of collimated rays) can be represented by multiplying the Stokes vector by Mueller matrix. One can describe the composition of several filters by

$$\vec{s_o} \;=\; M_N \ldots M_2 M_1 \vec{s_i}\,. \tag{5.19}$$

5.5.1 Reflection

The Mueller matrices for basic optical components (mainly polarization filters) are described in literature. The reflection on the planar surface can be represented by Mueller matrix as well [94]

$$M_R = \frac{\tan^2\theta_-}{2\sin^2\theta_+} \quad \cdot$$

$$\begin{pmatrix} \cos^2\theta_- + \cos^2\theta_+ & \cos^2\theta_- - \cos^2\theta_+ & 0 & 0 \\ \cos^2\theta_- - \cos^2\theta_+ & \cos^2\theta_- + \cos^2\theta_+ & 0 & 0 \\ 0 & 0 & -2\cos\theta_+\cos\theta_- & 0 \\ 0 & 0 & 0 & -2\cos\theta_+\cos\theta_- \end{pmatrix}, \tag{5.20}$$

where $\theta_+ = \theta_i + \theta_t$ and $\theta_- = \theta_i - \theta_t$.

5.5.2 Total reflection

The above Mueller matrix for the reflection holds both for the external reflection (incident light is in the optically less dense medium, e.g. air) as well as for the internal reflection (incident light is in the optically more dense medium, e.g. glass). It does not hold for the total reflection situation. The total reflection happens in the optically dense medium (internal reflection, $\eta_2 < \eta_1$) when incident angle θ_i is larger than critical angle θ_c [85]

$$\theta_i \geq \theta_c = \arcsin\frac{\eta_2}{\eta_1}\,. \tag{5.21}$$

Mueller matrix for total reflection has the form [94]

$$M_{Rt} = \begin{pmatrix} 1 & 0 & 0 & 0 \\ 0 & 1 & 0 & 0 \\ 0 & 0 & \cos\delta & -\sin\delta \\ 0 & 0 & \sin\delta & \cos\delta \end{pmatrix}, \tag{5.22}$$

where δ is the difference between the phase delay of the wave with the parallel polarization and the phase delay of the wave with the perpendicular polarization. Using Fresnel formulae and properly handling complex values of the reflection coefficients, it is possible to derive (while introducing new variables η_{12}, $\delta_\parallel$, $\delta_\perp$) the following relationships

$$\eta_{12} = \frac{\eta_2}{\eta_1}\,, \tag{5.23}$$

$$\delta_\parallel = \operatorname{argtan}(2\eta_{12}^2\cos\theta_i\sqrt{\sin^2\theta_i - \eta_{12}^2}, \eta_{12}^4\cos^2\theta_i - \sin^2\theta_i + \eta_{12}^2)\,, \tag{5.24}$$

$$\delta_\perp = \operatorname{argtan}(2\cos\theta_i\sqrt{\sin^2\theta_i - \eta_{12}^2}, \cos^2\theta_i - \sin^2\theta_i + 1)\,, \tag{5.25}$$

$$\delta = \delta_\parallel - \delta_\perp\,. \tag{5.26}$$

The argtan function with two arguments is the four quadrant argtan equal to arg function $\operatorname{argtan}(b,a) = \arg(a + \mathrm{i}b)$ [1] .

5.5.3 Transmitted light

The transmitted light can be calculated using Mueller matrix for transmission

$$M_T = \frac{\sin 2\theta_i \sin 2\theta_r}{2\sin^2\theta_+ \cos^2\theta_-} \begin{pmatrix} \cos^2\theta_- + 1 & \cos^2\theta_- - 1 & 0 & 0 \\ \cos^2\theta_- - 1 & \cos^2\theta_- + 1 & 0 & 0 \\ 0 & 0 & 2\cos\theta_- & 0 \\ 0 & 0 & 0 & 2\cos\theta_- \end{pmatrix} . \tag{5.27}$$

The Mueller matrices in the standard form represent the standard position of the filter. When the filter or optical component is rotated around the axis of light propagation relative to the standard position, one can use the rotation matrices to calculate Mueller matrix of the component rotated around the axis of the light propagation [165]:

$$M(\omega) = R(-\omega) M R(\omega) , \tag{5.28}$$

$$R(\omega) = \begin{pmatrix} 1 & 0 & 0 & 0 \\ 0 & \cos 2\omega & \sin 2\omega & 0 \\ 0 & -\sin 2\omega & \cos 2\omega & 0 \\ 0 & 0 & 0 & 1 \end{pmatrix} . \tag{5.29}$$

The irradiance of the ray or beam described by Stokes vector propagating in the transparent stone after several reflections can be easily calculated using the product of the corresponding Mueller matrices and rotation matrices:

$$\vec{s} = \left(\Pi_{i=N}^{1} R(-\omega_i) M_i R(\omega_i) \right) \vec{s}_0 , \tag{5.30}$$

where $R(\omega_i)$ and M_i are of the above form, corresponding to the i-th reflection. Note that one has to respect the order of the multiplication since the matrix multiplication does not commute in general.

[1] The order of arguments in this argtan is similar to the MatLab function atan2 and opposite to the Wolfram Mathematica function ArcTan.

Chapter 6

Light Path as a Graph

6.1 Motivation

A convex polyhedron stone illuminated by collimated beams constitutes a particularly simple situation. As discussed in Chapters 1 and 5, this simplification is still very close to the reality. Improvements in manufacturing technology in jewelry industry bring us even closer to this ideal. In this chapter we show how to describe the light propagation in convex polyhedron as a graph.

We assume that a convex polyhedral stone is illuminated by a single or several beams of collimated light. One can observe a certain structure in the collimated beam propagation. Let us show how to describe this structure by a graph.

Let us introduce *beam segments*. A beam segment is the subset of a beam propagating in a stone between interactions with its optical interfaces or going from one interface to infinity.

There are two effects involved in the beam formation in a stone. See Fig. 6.1. The first effect is the splitting of the beam. This effect is purely geometrical. The split occurs when a beam hits two or more facets. We can, without loss of generality, the split in the situation when a beam hits only single facet.

The second effect is the interaction of a light beam with the surface, i.e. with the facet. The reflection and refraction occurs on the facet producing reflected and refracted beams. When an incident beam hits a facet from the stone interior with the material optically denser than outside of the stone, the total reflection can occur. The incident angle is larger than the critical angle in this situation, see Sec. 5.5.2.

Both effects give rise to new beams. The split effect can create one or more beams. The reflection produces always one new beam. The refraction can produce one new beam or no new beam in the case of the total reflection.

Both effects alternate periodically during the light propagation.

6.2 Graph definition

Let us represent the beam segments by nodes in the graph.

Split, reflection, and refraction can be represented by oriented edges in the graph.

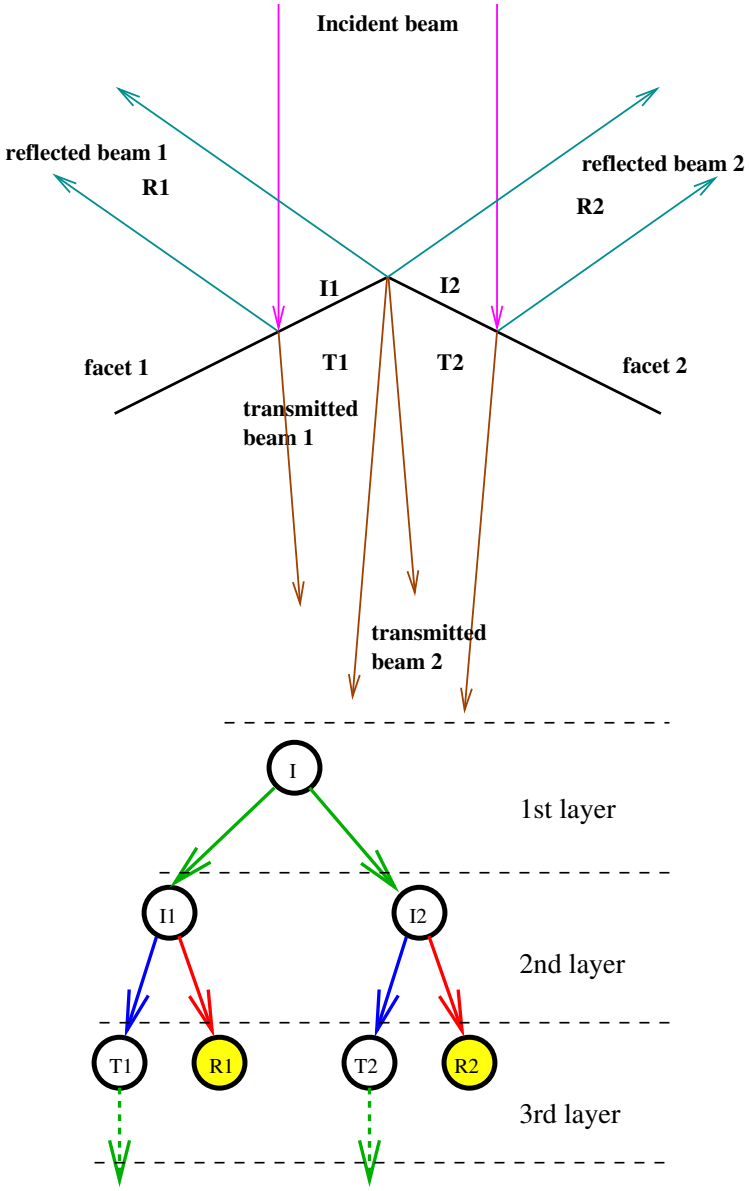

Figure 6.1: Top: Two interactions multiplying the number of collimated beams in a stone. An incident beam (magenta) illuminates two facets. The incident beam splits into two beams I_1 and I_2, illuminating facet 1 and facet 2, respectively. The beam I_1 is reflected and refracted into R_1 and T_1, respectively. The beam I_2 is reflected into R_2 and it is transmitted into T_2. Bottom: The graph representing the interaction shown above. The incident beam splits into two beams I_1 and I_2, illuminating facet 1 and facet 2, respectively. The beam I_1 is reflected and refracted into R_1 and T_1, respectively. The beam I_2 is reflected into R_2 and it is transmitted into T_2. The layers correspond to the node and edge height. The green edges represent splits, the blue edges represent refractions and red edges represent reflection. The detailed explanation of the graph is in Fig. 6.2.

Edges lead from the nodes representing incident beam segments to the nodes representing the split, reflected, or refracted beam segments.

The graph is a tree for each collimated beam illuminating the stone. The root of the tree is the illuminating beam. The tree is infinite in principle as the light can be reflected in the stone infinitely many times. The graph is always finite in computer simulations.

The beams exiting the stone are leaves of the tree. A beam can exit either because it is reflected by the stone surface when hit by a beam from outside or because it is refracted from the inside of a stone. The other nodes represent the beam segments still propagating in the stone.

The tree can be organized into odd and even layers (see Fig. 6.1 and 6.2) where edges of odd layers represent the beam splitting and edges of even layers represent refraction or reflection.

The graph can be a forest in the case of multiple illuminating beams. Each illuminating beam will produce a tree within the forest.

An *elementary beam* corresponds to a path from the root node, i.e. from the illuminating beam, to leaf node, i.e. to a beam segment exiting the stone. Each leaf corresponds to just one elementary beam.

To summarize, we have:

- A set of nodes $N = \{1, \ldots, n\},\ n \in \mathcal{N}$.

  Each node corresponds to a beam segment.

- A set of edges $E \subseteq N^2$.

  Each edge (k_i, k_j) corresponds to one of the interactions which produce the new beam segment k_j from the beam segment k_i.

- A graph $G = (N, E)$.

  The graph G describes the propagation of collimated beams of light in the stone.

- A logical function input(k) which assigns true to input illuminating beam segment and false

- A logical function exit(k) which assigns true to beam segments leaving the stone interior and false otherwise to all other beam segments.

- A set of edge attributes $\mathcal{G} = \{\mathrm{S}, \mathrm{R}, \mathrm{T}\}$, namely S for a split edge, R for a reflection edge, and T for a transmission (refraction) edge.

- A function edgetype$((k_i, k_j))$ which assigns to edges their attributes from the set $\mathcal{G}$.

- A function history(k) which assigns to the beam segment k the sequence of beam segments history$(k) = (k_1, \ldots, k_L)$:

$$\forall k \in N \quad \exists!\, \mathrm{history}(k) = (k_1, \ldots, k_L) : \\ \mathrm{input}(k_1) \ \wedge\ (\forall l \in \{1, \ldots, L-1\} : (k_l, k_{l+1}) \in E) \ \wedge\ k = k_L\,. \tag{6.1}$$

In other words, history of the beam segment k is the oriented path from the input beam k_1 to the beam segment k.

- A function elementary(k) which for each exiting beam k, exit(k) = T, assigns the path from the input beam to the exiting beam:

$$\text{elementary}(k) = \text{history}(k)\,. \tag{6.2}$$

The elementary beams are the beams we are interested in from the radiometric point of view.

- A function nodedepth(k) which assigns to the node its depth [95], that is the distance to the root. The root has a depth 1.
- A function edgedepth((k_i, k_j)) which assigns to the edge its the depth of the node the starts in.
- Each beam segment - node can be labeled by parameters of the beam such as the direction vector, the polygon of the cross-section, etc.
- Each edge can be further attributed by the label of the facet, where split, refraction, or reflection occurs.

One can make the following observations (see Fig. 6.2):

- The graph G is a forest of rooted trees. The root of each tree corresponds to the input, illuminating beam.
- Edges in odd layers have attribute split S:

$$\begin{gathered}\forall(k_i, k_j) \in E : \\ \text{edgedepth}((k_i, k_j)) = 2j - 1 \ \wedge \ j \in \mathcal{N} \ \Rightarrow \ \text{edgetype}((k_i, k_j)) = \text{S}\,.\end{gathered} \tag{6.3}$$

We defined our graph in such a way that the beam hitting the stone surface is first analyzed geometrically (splits) and then physically (refractions, reflections). This two steps repeat.

- Edges in even layers have attributes either reflect R or transmit T:

$$\begin{gathered}\forall(k_i, k_j) \in E : \\ \text{edgedepth}((k_i, k_j)) = 2j \ \wedge \ j \in \mathcal{N} \ \Rightarrow \ \text{edgetype}((k_i, k_j)) \in \{\text{R}, \text{T}\}\,.\end{gathered} \tag{6.4}$$

- Exiting beams in the third layer are reflected (they did not enter the stone):

$$\begin{gathered}\forall k \in N : \\ \text{nodedepth}(k) = 3 \ \wedge \ \text{exit}(k) \Rightarrow \exists!(k_i, k) \in E \ \wedge \ \text{edgetype}((k_i, k)) = \text{R}\,.\end{gathered} \tag{6.5}$$

The illuminating beam is incident from outside so the exiting beam is reflected. Note that the first layer represents the split of the input beam.

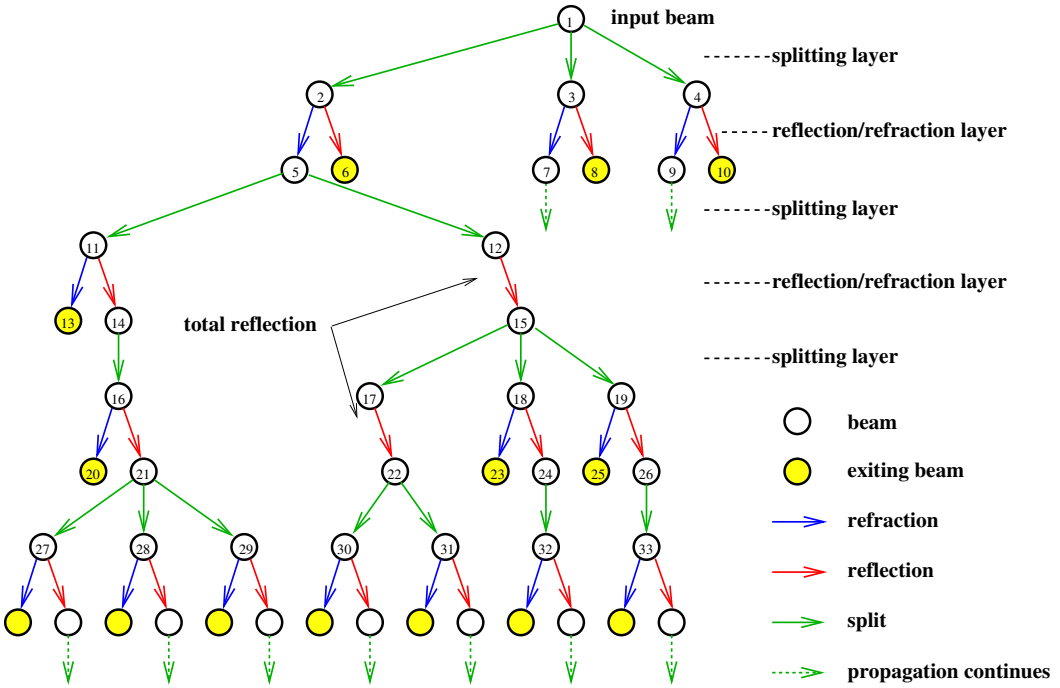

Figure 6.2: Propagation of a beam in a stone. Two main interactions are involved. A split happens when the beam hits more facets. The reflection and transmission occur on facets. The beam segments are represented by circles. The beams exiting the stone are represented by filled yellow circles. The beam hitting the facet from inside can be totally reflected, i.e. no refraction into air happens. The graph may never terminate. The numbers in the nodes indicate the node numbers.

- Exiting beams in the following odd layers are transmitted:

$$\forall k \in N : \text{nodedepth}(k) = 2j + 3 \ \wedge \ j \in \mathcal{N} \ \wedge \ \text{exit}(k) \Rightarrow \\ \exists!(k_i, k) \in E \ \wedge \ \text{edgetype}((k_i, k)) = \text{T} \, . \tag{6.6}$$

  The only way to get out of the stone is refraction.

- The beams in even layers are never exiting:

$$\forall k \in N : \text{nodedepth}(k) = 2j \ \wedge \ j \in \mathcal{N} \Rightarrow \neg \, \text{exit}(k) \, . \tag{6.7}$$

  Exiting beams are leaves of the graph G. As the stone is convex, the exiting beam cannot hit the stone anymore.

6.3 Radiometry of the beam propagation

As mentioned above in Sec. 5.5, the radiometric properties of the beam can be described by Stokes vectors. The effects on the surfaces can be described by Mueller matrices. Let us assume that the stone material is clear transparent.

We can label nodes and edges of our graph by additional attributes, with numerical values this time.

Formally let us have:

- A function $\mathrm{s}(k)$ assigning to each node k a Stokes vector $\mathrm{s}(k)$.

  The Stokes vectors for input beams are given by the user to reflect the experiment.

- A function $\mathrm{M}((k_i, k_j))$ assigning to each edge (k_i, k_j) the Mueller matrix $\mathrm{M}((k_i, k_j))$.

  Mueller matrix can be calculated using the geometry (direction vector and orientation of the coordinate system for polarization) of the beam segment and geometrical position of the facet reflecting/transmitting the beam.

- The unit Mueller matrix assigned to the split edges:

$$\forall (k_i, k_j) \in E : \mathrm{edgetype}((k_i, k_j)) = \mathrm{S} \Rightarrow \mathrm{M}((k_i, k_j)) = I\,. \tag{6.8}$$

  The matrix I is a 4×4 unit matrix. The split is only a geometrical operation. It does not influence the radiometric properties of the beam.

The Stokes vector $s(k)$ of the beam segment k with $\mathrm{history}(k) = (k_1, \ldots, k_L)$ is a product

$$\mathrm{s}(k) \quad = \quad \left(\prod_{l=L-1}^{1} \mathrm{M}((k_l, k_{l+1})) \right) \mathrm{s}(k_1)\,. \tag{6.9}$$

The sum of the (scalar) radiant fluxes of the beams in the chosen layer plus the sum of the radiant fluxes of the exiting beams in all layers above the chosen layer is equal to the sum of the radiant fluxes of all input beams. This follows from the energy conservation law as we have no light absorption in the model. This can be used, e.g., for calculating what is the radiant flux of the beam segments still in the simulation by subtracting the flux of exiting beams from the input beams.

Chapter 7

Light Propagation in Absorbing Medium

7.1 Motivation

It is desirable to model propagation of the light in color cut stones. In this chapter, we will describe a light propagation model in transparent stones, which partly absorb the propagating light. The color stones can be modeled as standard colorless transparent stones with an absorption model added. From the practical point of view the directly observable influence of the absorption is that most of the light beams exiting color stones disappear or are strongly attenuated. We are interested in calculating the radiant flux of exiting light beams.

7.2 Assumptions

Assumptions of our model are similar to the assumptions for the transparent stone modeling:

- Material is transparent. The light propagates according to the standard ray optics. The individual rays are not scattered in the medium.
- Material is absorbing. The irradiance of a ray decreases as it propagates through the medium according to Beer's law [76].
- Beams have convex polygonal cross-sections. Collimated rays remain collimated within the beam.
- Beams are reflected or refracted by planar surfaces separating optical media with different refraction indices.
- The irradiance of individual rays in the beam across of the beam cross-section is constant when entering the absorbing media. The light can be polarized.

7.3 Derivation of the model

7.3.1 Ray

Let us first study an individual ray. The power characteristic of a ray studied here is the *irradiance* (not to be confused with radiant intensity), which is defined as the derivative of the radiant flux by the area

$$E = \frac{\mathrm{d}\Phi}{\mathrm{d}S} \tag{7.1}$$

in $\mathrm{W/m^2}$ units.

Alternatively, we can use the *spectral irradiance*, which expresses dependence of the irradiance on the light wavelength λ

$$E_\lambda(\lambda) = \frac{\mathrm{d}\Phi_\lambda(\lambda)}{\mathrm{d}S} = \frac{\mathrm{d}\Phi}{\mathrm{d}\lambda\,\mathrm{d}S}\,, \tag{7.2}$$

in $\mathrm{W/m^3}$ units.

The basic formula governing the light ray attenuation in the absorbing medium is the Beer's law [76]

$$E = E_0\,\mathrm{e}^{-\beta d}\,, \tag{7.3}$$

where E_0 is the irradiance of the light ray at the start of its path through the absorbing medium and E is the ray irradiance after traveling distance d in the medium with the absorption coefficient β.

Light polarizes due to the reflection and refraction, which can be modeled by the Stokes vector. The absorbing medium attenuates all components of the polarized light equally. All Stokes vector coordinates are proportional to the irradiance. So, for the polarized light, we can write

$$\vec{s} = \mathrm{e}^{-\beta d}\,\vec{s}_0\,. \tag{7.4}$$

Let us remind that effects on the media boundary, reflection and refraction, also influence the irradiance of the reflected beam in the form

$$\vec{s} = M\,\vec{s}_0\,, \tag{7.5}$$

where M is a Mueller matrix obtained from Fresnel formulae.

The Mueller matrix M is a function of the incident angle and the refraction indices of the media. The refraction indices depend on the wavelength of the light. One can write $M_i(\theta_i, \eta_1(\lambda), \eta_2(\lambda))$. The material is the same for the whole path in our case. Thus $\eta_1(\lambda)$, $\eta_2(\lambda)$ are constant. Let us neglect the dependence on the wavelength λ in the formulae to simplify the notation.

We will not aim here at calculating the radiant flux over the whole spectrum. The dependence of the refraction index on the wavelength is rarely known analytically, so the possible integration over all used wavelengths has to be done numerically anyway

$$\vec{s} = \int_{\lambda_1}^{\lambda_2} \vec{s}_\lambda\,\mathrm{d}\lambda\,. \tag{7.6}$$

Rays can be reflected several times in a stone while their irradiance is gradually attenuated by the absorption. Assuming N reflections, each with the Mueller matrix M_i, we have $N+1$ absorbing traveling paths, before, between, and after reflections. Each traveling path has length d_i. The Stokes vector after the propagation is

$$\begin{aligned}
\vec{s} &= \mathrm{e}^{-\beta d_N} M_N \dots \mathrm{e}^{-\beta d_1} M_1 \, \mathrm{e}^{-\beta d_0} \, \vec{s}_0 = && (7.7)\\
&= \left(\prod_{i=N}^{1} \mathrm{e}^{-\beta d_i} M_i \right) \mathrm{e}^{-\beta d_0} \vec{s}_0 = && (7.8)\\
&= \left(\prod_{i=0}^{N} \mathrm{e}^{-\beta d_i} \right) \left(\prod_{i=N}^{1} M_i \right) \vec{s}_0 = && (7.9)\\
&= \mathrm{e}^{-\beta \sum_0^N d_i} \left(\prod_{i=N}^{1} M_i \right) \vec{s}_0 \,. && (7.10)
\end{aligned}$$

The order of scalar multiplications can be rearranged to obtain the attenuation of the ray along its path in the absorbing media and by a sequence of losses of the energy by the refractions of light on optical interfaces.

7.3.2 Beam

Let us turn our attention to a beam of light propagating in absorbing media.

A convex beam entering a convex polyhedron divides into many beams as a result of reflections and refractions on the individual facets. All resulting beams have convex cross-sections as a result of intersections of convex beams with convex facets. The faces of a convex polyhedron are convex facets. We call the elementary beam a maximal subset of the incident light beam, which passes through a stone without a split into smaller beams. See Chapter 6.

Technically, we propagate beams through a stone, while they are divided into sub-beams by falling onto two or more facets. We track each new sub-beam and finally we backtrack all resulting elementary beams back to the source of light. Each elementary beam is then analyzed separately. See Fig.7.1.

Let us now discuss one elementary beam (see Fig. 7.2). We are interested in the radiant flux of the beam after its propagation.

An elementary beam has a convex polygonal cross-section and can be several times reflected from the media planar boundaries. Each reflection is accompanied by a refraction, so each time the beam is reflected, the irradiance of individual rays changes. The irradiance and the Stokes vector of the light entering the absorbing media are assumed to be constant across the beam.

Mueller matrix M_i for reflections or refractions of beams of collimated rays on planar surfaces is the same for all rays in the beam since they are incident under the same angle.

The resulting beam will consist of collimated rays with different irradiances across the beam. They have the same degree of polarization which is different from the incident ray polarization in general.

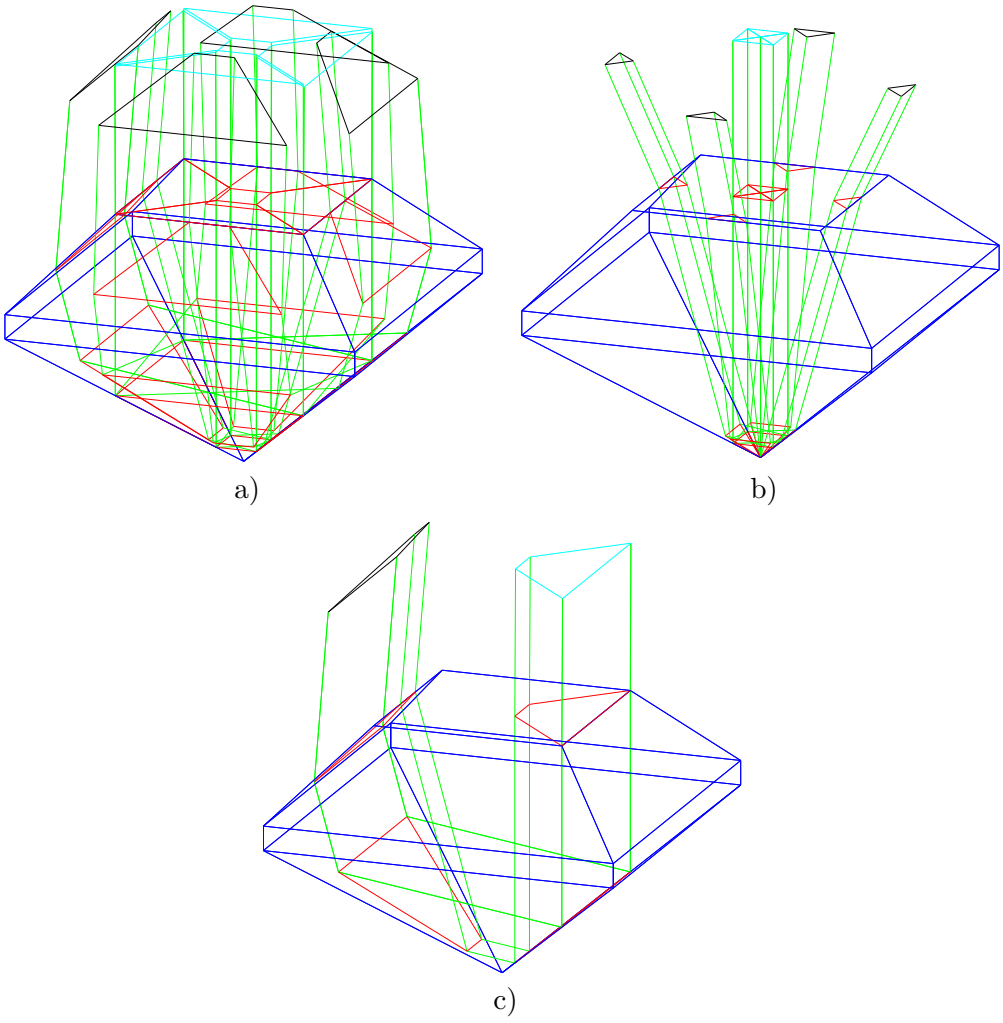

Figure 7.1: Tracking beams in the square cut stone. a) and b) The light falling onto the stone table (square facet on the stone top) forms the incident beam. The beam is two times reflected inside the stone. When a beam falls on two different facets, it splits into sub-beams. Tracking the beam splitting through all reflections allows to find elementary beams. c) A single elementary beam is shown in the second row. For this beam, we can calculate the radiant flux at the exit of the beam from the stone.

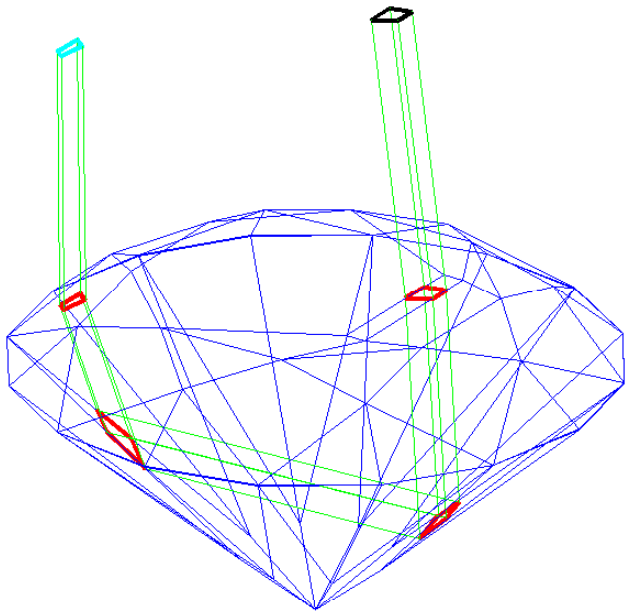

Figure 7.2: One elementary beam passing through a stone. Only one elementary output beam is tracked back to the input beam.

The beam cross-section perpendicular to the beam direction has a constant area and shape since each reflection just mirrors the cross-section shape back and forth.

A sequence of convex polyhedra can be rearranged into a single prism with the same cross-section and the base perpendicular to the sides of the prism. See Fig. 7.3.

Then, the prism can be rectified into a new rectangular prism in such a way that the perpendicular cross-section forms one new perpendicular base.

The lengths of edges perpendicular to the first base are identical to the lengths of optical path of rays in the vertices of the base. The original rays and rays in new prism have the same length of travel in absorbing media. To calculate the radiant flux of the beam at the last boundary, we can evaluate the radiant flux at the end of the new straight prism. This straight prism does not have parallel bases, though.

Let us define the following parameters (see Fig. 7.4):

x, y are the coordinates in the plane of the base of the rectified prism,

p_{ix}, p_{iy} are the coordinates of the i-th vertex of the base in the xy plane containing it,

$d(x, y)$ is the height of the prism at the coordinates (x, y),

$\vec{s_0}$ is the Stokes vector of the beam at the beginning of the light path,

β is the absorption coefficient.

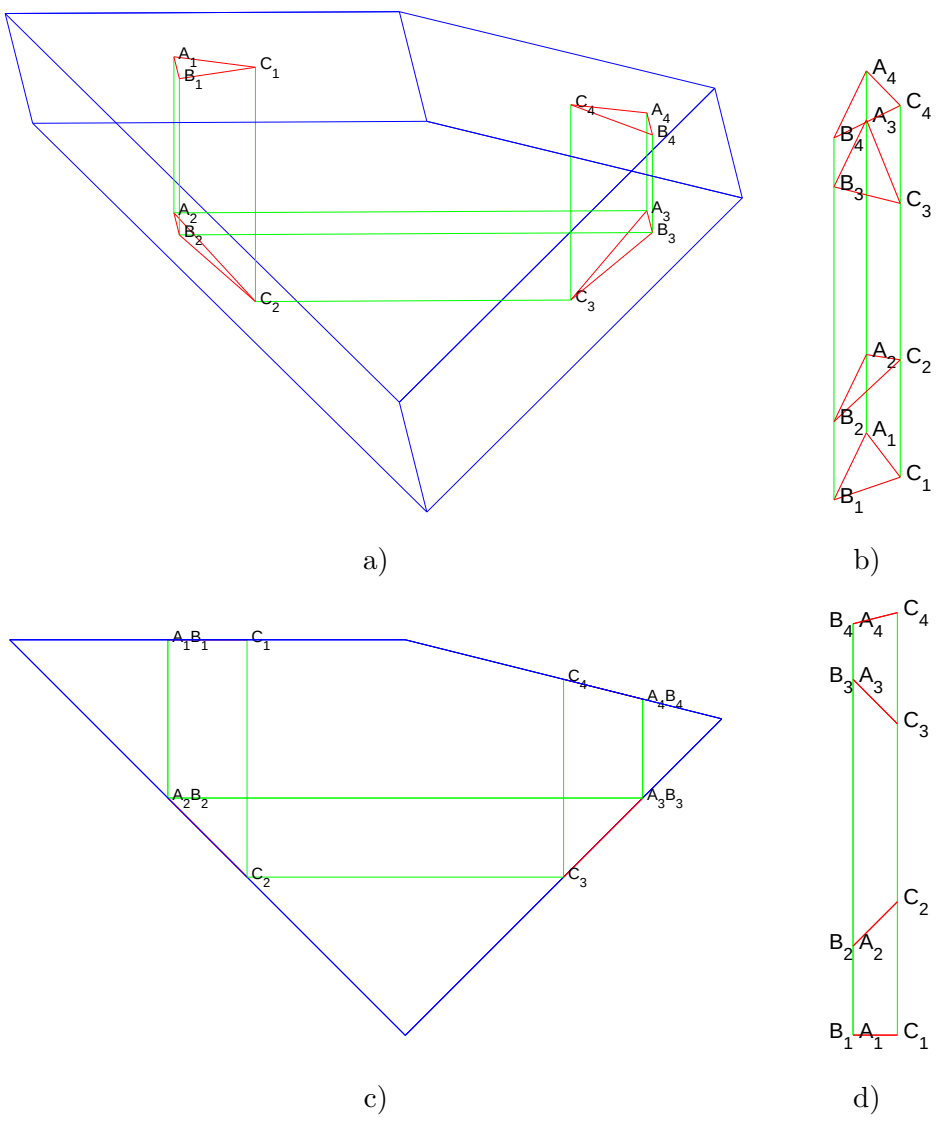

Figure 7.3: One beam (green) passing through a stone (blue). a) An oblique view of the beam in the stone, b) an oblique view on the rectified beam – prism. c) The side view of the beam in the stone, d) the side view of the rectified beam – prism. An example of a ray is the line $A_1A_2A_3A_4$. The example of a beam cross-section, not necessarily perpendicular to the beam directional vector, is the triangle $A_2B_2C_2$.

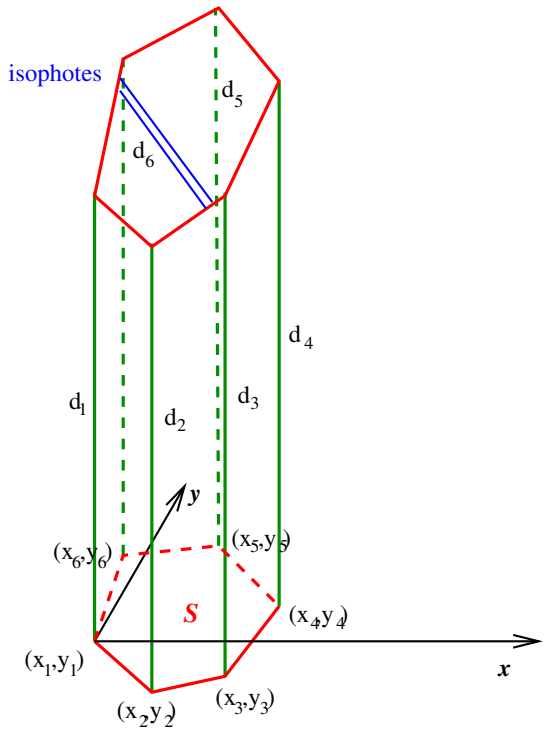

Figure 7.4: The beam after rectification. Each ray corresponds to a line parallel to the z axis. The base of the prism is in the xy plane. The other base is not parallel to the xy plane in general. The length of the ray traveled inside the stone is denoted as d_i. The isophotes, i.e. the lines of constant irradiance, are parallel to the xy plane.

As the other base of the prism is planar but not necessarily parallel to the first base, the height at the point (x, y) can be expressed as $d(x, y) = ax + by + c$, a, b, c being parameters of this linear function of two coordinates (x, y).

The problem of computing the radiant flux can be formulated as calculating the integral of the irradiance over the convex polygonal area. As the light is polarized, we use Stokes vector of the radiant flux

$$\vec{\Phi} = \iint_S \vec{s}\,\mathrm{d}S = \tag{7.11}$$

$$= \iint_S \mathrm{e}^{-\beta d(x,y)} \left(\prod_{i=N}^{1} M_i\right) \vec{s}_0\,\mathrm{d}S = \tag{7.12}$$

$$= \left(\prod_{i=N}^{1} M_i\right) \vec{s}_0 \iint_S \mathrm{e}^{-\beta d(x,y)}\,\mathrm{d}S = \tag{7.13}$$

$$= \left(\prod_{i=N}^{1} M_i\right) \vec{s}_0 \iint_S \mathrm{e}^{-\beta (ax+by+c)}\,\mathrm{d}S\,. \tag{7.14}$$

The irradiance of the incident light $\vec{s}_0$ as well as Mueller matrices M_i are indepen-

dent of the location of the ray within the beam and thus they can be moved in front of the integral.

Using Green's theorem, one can convert the integration of the irradiance over an area into the integration over the area boundary. Let us have the vector field with the components $(f(x,y), g(x,y))$, which have continuous partial derivatives. Then, the following equation holds

$$\iint_S \left(\frac{\partial g(x,y)}{\partial x} - \frac{\partial f(x,y)}{\partial y} \right) \mathrm{d}x\,\mathrm{d}y = \oint_C (f(x,y)\ \mathrm{d}x + g(x,y)\,\mathrm{d}y)\,. \tag{7.15}$$

We substitute in our case

$$\begin{aligned} g(x,y) &= 0\,, & (7.16)\\ f(x,y) &= \int -\mathrm{e}^{-\beta d(x,y)}\,\mathrm{d}y = & (7.17)\\ &= \int -\mathrm{e}^{-\beta(ax+by+c)}\,\mathrm{d}y = & (7.18)\\ &= \frac{1}{\beta b}\mathrm{e}^{-\beta(ax+by+c)} + h\,, & (7.19) \end{aligned}$$

where h is an integration constant.

The special case for $b = 0$ has to be considered. This situation happens when y axis is parallel to the lines of constant light irradiance in the rectified beam. One can cope with that either by rotating the rectified prism coordinate system in which the radiant flux is calculated around axis parallel to z axis, or by different substitution of $g(x,y)$ and $f(x,y)$, e.g. $f(x,y) = 0$ and $g(x,y) = \int \mathrm{e}^{-\beta d(x,y)}\,dx$.

Another special case is for zero absorption, i.e. when β equals zero. In this case, one has to calculate only the area of the polygon. It can be easily done by another substitution into the Green's theorem

$$\begin{aligned} P_S &= \iint_S \mathrm{d}S = & (7.20)\\ &= \frac{1}{2}\sum_{j=1}^{n}(x_j y_{j+1} - x_{j+1} y_j)\,, & (7.21)\\ \vec{\Phi} &= \left(\prod_{i=N}^{1} M_i \right) \vec{s}_0 S = & (7.22)\\ &= \left(\prod_{i=N}^{1} M_i \right) \vec{s}_0 \frac{1}{2}\sum_{j=1}^{n}(x_j y_{j+1} - x_{j+1} y_j)\,, & (7.23) \end{aligned}$$

where n is the number of vertices of the prism base and $x_{n+1} = x_1$, $y_{n+1} = y_1$. P_S is the area of the integration domain S, i.e. the area of the beam perpendicular cross-section.

The special case for $d(x,y) = c$ is trivial and corresponds to the situation when the rectified prism is right

$$\vec{\Phi} = \iint_S \vec{s}\,\mathrm{d}S = \tag{7.24}$$

$$= \left(\prod_{i=N}^{1} M_i\right)\vec{s}_0 \iint_S \mathrm{e}^{-\beta c}\,\mathrm{d}S = \tag{7.25}$$

$$= \mathrm{e}^{-\beta c} P_S \left(\prod_{i=N}^{1} M_i\right)\vec{s}_0\,. \tag{7.26}$$

The radiant flux in the regular case ($b \neq 0, \wedge \beta \neq 0$) becomes

$$\vec{\Phi} = \left(\prod_{i=N}^{1} M_i\right)\vec{s}_0 \oint_C \left(\int -\mathrm{e}^{-\beta(ax+by+c)}\,\mathrm{d}y\right)\mathrm{d}x = \tag{7.27}$$

$$= \left(\prod_{i=N}^{1} M_i\right)\vec{s}_0 \oint_C \frac{1}{\beta b}\mathrm{e}^{-\beta(ax+by+c)}\,\mathrm{d}x\,. \tag{7.28}$$

As the area is polygonal, its boundary consists of straight lines which can be parameterized by parameter t running from 0 to 1:

$$\vec{\Phi} = \frac{1}{\beta b}\left(\prod_{i=N}^{1} M_i\right)\vec{s}_0 \sum_{j=1}^{n} \int_0^1 \mathrm{e}^{-\beta(a(x_j+t(x_{j+1}-x_j))+b(y_j+t(y_{j+1}-y_j))+c)}(x_{j+1}-x_j)\,\mathrm{d}t\,, \tag{7.29}$$

$$\vec{\Phi} = \frac{\mathrm{e}^{-\beta c}}{\beta^2 b}\left(\prod_{i=N}^{1} M_i\right)\vec{s}_0 \sum_{j=1}^{n} \frac{(x_{j+1}-x_j)(\mathrm{e}^{-\beta(ax_{j+1}+by_{j+1})} - \mathrm{e}^{-\beta(ax_j+by_j)})}{(a(x_j-x_{j+1})+b(y_j-y_{j+1}))}\,. \tag{7.30}$$

The special case occurs for $a(x_j - x_{j+1}) + b(y_j - y_{j+1}) = 0$. This corresponds to the situation when one edge of the prism is parallel to the lines of constant irradiance. The integral can be then simply solved with the result

$$a(x_j - x_{j+1}) + b(y_j - y_{j+1}) = 0 \quad \Rightarrow \tag{7.31}$$

$$\int_0^1 \mathrm{e}^{-\beta(a(x_j+t(x_{j+1}-x_j))+b(y_j+t(y_{j+1}-y_j))+c)}(x_{j+1}-x_j)\,\mathrm{d}t = \tag{7.32}$$

$$= (x_{j+1}-x_j)\mathrm{e}^{-\beta(ax_j+by_j+c)}\,. \tag{7.33}$$

The absorbed light is converted into heat.

7.4 An example

The above result can be demonstrated, e.g., on the beam from the Fig. 7.3. The height of the rectified beam is 9.25 mm (rays A, B) and 9.5 mm (ray C). The area of the beam is $P_S = 1$ mm^2, as it forms the right angled triangle with legs of length $\sqrt{2}$ mm.

7.4.1 Transparent clear glass

The prism is made from glass with $\eta_2 = 1.5$. The absorption coefficient is set to 0. The Stokes vector is

$$\vec{s}_{0u} = \begin{pmatrix} E_0 \\ 0 \\ 0 \\ 0 \end{pmatrix}, \tag{7.34}$$

for unpolarized light and

$$\vec{s}_{0c} = \begin{pmatrix} E_0 \\ 0 \\ 0 \\ E_0 \end{pmatrix} \tag{7.35}$$

for circularly polarized light. The subscript u corresponds to unpolarized light, c for circularly polarized light example.

The beam incident perpendicularly to the first surface undergoes no polarization but it is slightly attenuated as the part of the light is reflected back. The amount of transmitted light is determined by the Mueller matrix for the transmitting light (Eq. 5.27)

$$M_{T1} = \begin{pmatrix} 0.960 & 0.000 & 0.000 & 0.000 \\ 0.000 & 0.960 & 0.000 & 0.000 \\ 0.000 & 0.000 & 0.960 & 0.000 \\ 0.000 & 0.000 & 0.000 & 0.960 \end{pmatrix}. \tag{7.36}$$

Note that Mueller matrices are dimensionless. The second and the third reflections are in the region of total reflection ($\theta_i = 45°$, critical angle $\theta_c = \arcsin(1/1.5) = 41.8°$). The Mueller matrices are as follows (Eq. 5.22)

$$M_{R2} = M_{R3} = \begin{pmatrix} 1.000 & 0.000 & 0.000 & 0.000 \\ 0.000 & 1.000 & 0.000 & 0.000 \\ 0.000 & 0.000 & 0.800 & 0.600 \\ 0.000 & 0.000 & -0.600 & 0.800 \end{pmatrix}. \tag{7.37}$$

The last transmission has the incidence angle $\theta_i = \arctan(1/4)$ which gives (Eq. 5.27)

$$M_{T4} = \begin{pmatrix} 0.960 & -0.008 & 0.000 & 0.000 \\ -0.008 & 0.960 & 0.000 & 0.000 \\ 0.000 & 0.000 & 0.960 & 0.000 \\ 0.000 & 0.000 & 0.000 & 0.960 \end{pmatrix}. \tag{7.38}$$

The product of all Mueller matrices is

$$M = M_{T4}M_{R3}M_{R2}M_{T1} = \begin{pmatrix} 0.921 & -0.007 & 0.000 & 0.000 \\ -0.007 & 0.921 & 0.000 & 0.000 \\ 0.000 & 0.000 & 0.258 & 0.884 \\ 0.000 & 0.000 & -0.884 & 0.258 \end{pmatrix}. \tag{7.39}$$

One can see that the unpolarized light will get slightly linearly polarized while the circularly polarized light will have all Stokes vector components nonzero (the incident light irradiance is set to 1 W/m^2 here):

$$\vec{s}_{uc} = M\vec{s}_{0u} = M\begin{pmatrix}1\\0\\0\\0\end{pmatrix} = \begin{pmatrix}0.921\\-0.007\\0.000\\0.000\end{pmatrix}\ \mathrm{W/m^2}\,, \tag{7.40}$$

$$\vec{s}_{cc} = M\vec{s}_{0c} = M\begin{pmatrix}1\\0\\0\\1\end{pmatrix} = \begin{pmatrix}0.921\\-0.007\\0.884\\0.258\end{pmatrix}\ \mathrm{W/m^2}\,. \tag{7.41}$$

$$\vec{\Phi}_{uc} = P_S M\vec{s_{0u}} = 10^{-6}\begin{pmatrix}0.921\\-0.007\\0.000\\0.000\end{pmatrix}\ \mathrm{W}\,, \tag{7.42}$$

$$\vec{\Phi}_{cc} = P_S M\vec{s_{0c}} = 10^{-6}\begin{pmatrix}0.921\\-0.007\\0.884\\0.258\end{pmatrix}\ \mathrm{W}\,. \tag{7.43}$$

The second subscript c stands for "clear" glass example.

7.4.2 Transparent absorbing glass

Let us now consider the prism with the same shape as above but made from absorbing glass with $\eta_2 = 1.5$. The absorption coefficient is set to 200 m^{-1}, which corresponds to the attenuation e^{-1} at 5 mm. The Mueller matrices are the same as for the absorbing prism.

As the area of the beam is 1 mm^2, the Stokes vector of the radiant flux of the exiting beam is according to Eq. 7.30

$$\vec{\Phi}_{ua} = 10^{-6}\begin{pmatrix}0.142\\-0.001\\0.000\\0.000\end{pmatrix}\ \mathrm{W}\,, \tag{7.44}$$

$$\vec{\Phi}_{ca} = 10^{-6}\begin{pmatrix}0.142\\-0.001\\0.137\\0.040\end{pmatrix}\ \mathrm{W}\,. \tag{7.45}$$

7.5 Applications

The color stones make a significant fraction of the total volume of stones on the market. Until recently, its modeling was not possible with the sufficient accuracy by the beam modeling software LADOK we developed in the past [145].

The formulae derived in this chapter are easy to implement and their calculation is not time consuming. The calculation of the radiant flux of collimated beams propagating in stones made from absorbing transparent materials, which we developed here, gives an accurate model of the light propagation in color stones.

It can be used to design more efficient inspection procedures and machines.

Chapter 8

Optical Effects on the Stone Edges

8.1 Motivation

One of our long term goals has been computing the CAD model parameters from measured data measured on real stone. There is a CAD model of the planned product and the actually manufactured stone. The desire is to adjust the parameters of the CAD model to fit precisely the actual stone. The obtained parameters can be used, e.g., for the production technology adjustment. This, in principle, can be achieved by our method sketched in Section 4.4.

One of the imminent problems can be discovered when comparing the simulation and the experiment in Fig. 4.4. The problem, well known in computer vision, is called the correspondence problem. We have two sets of data. The simulation gives us the azimuth, the elevation, the radiant flux, and the polarization for each beam. In the experimental part, one measures the intensities of the traces on the screen. One has to assign the right trace to each simulated beam.

This is not an easy task. In our previous work [83], we suggested to illuminate the stone by very localized narrow beams and to produce only a subset of traces at each time. This approach makes the measurement slower as many images need to be captured. In addition, this complicates the measuring machine as the narrow beam is needed and has to be manipulated in space during data acquisition.

The traditional "engineering" approach to ease the correspondence problem is to add some labels or features to the corresponding items, which facilitate the matching. We noticed that the observed traces are distinguishable neither by the shape of polygons nor as nice isolated spots with Gaussian intensity. The shape of the traces thus cannot be used as a feature supporting the matching.

We observed that the traces have often sharp protrusions. The protrusions, particularly their number and directions, can be used as additional features. See Fig. 8.1.

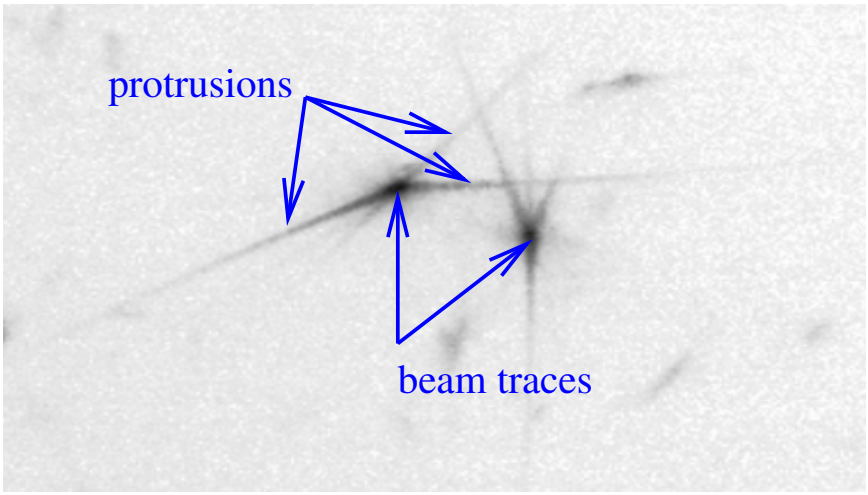

Figure 8.1: A detail of an image of beam traces for the chaton illuminated by a laser beam. The beam traces are central spots, saturated in original image. They correspond to the beams reflected and refracted from facets. The protrusions are often much weaker traces of rays reflected or refracted from edges. The direction of protrusions can be used as additional information in the correspondence search between the results of a simulation and the real experiment with a stone. The photo is a detail from Fig. 4.4. The detail was chosen to show visible protrusions from the beam traces.

8.2 Problem statement

We would like to understand how visible protrusions are formed and whether their parameters can be computed from our model.

The protrusions are caused by imperfections of the manufacturing process, mainly that the edges between facets are not perfectly sharp.

Shape of Stone Edges Let us assume the following model. We have two planar facets, which intersect in a line. We have the light beam falling on the both facets including their intersection. Let us suppose that the intersection is not sharp but it curves smoothly from one plane to the other in the cylindrical shape. We are interested in the spatial distribution of the refracted rays, which pass through small patches of the curved surface.

Mathematically, we have two planes with normals $\vec{n}_1$ and $\vec{n}_2$. The intersection has directional vector $\vec{e}$. The normals are perpendicular to the vector $\vec{e}$. The intersection of the planes, when approximated by a cylindrical surface, can be further approximated by a set of narrow planar surfaces with normals interpolated from $\vec{n}_1$ to $\vec{n}_2$. The rays falling on the facets and the intersection have a directional vector $\vec{v}_i$. The refracted rays have a directional vectors $\vec{v}_t$. The reflected rays have a directional vector $\vec{v}_r$. See Fig. 8.2.

We are going to show that the vectors $\vec{v}_t$ and $\vec{v}_r$ are lying on a conical surface of

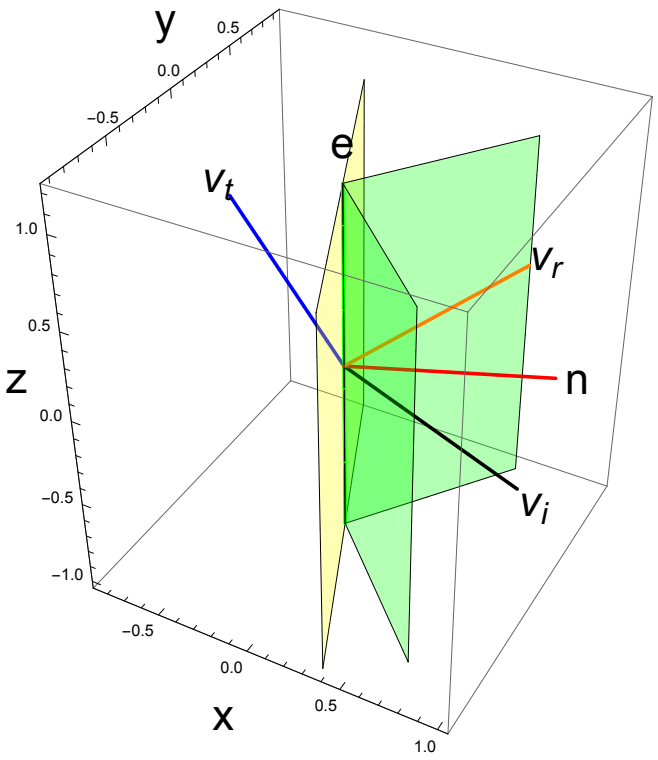

Figure 8.2: The sketch of the mathematical model of a round edge. The green planes are the facets. The yellow plane is tangent to the rounded edge surface, the red vector $\vec{n}$ is its normal. It lies in the xy plane. The black vector $\vec{v}_i$ is the incident ray, the blue vector $\vec{v}_t$ is one refracted (transmitted) ray and the orange vector $\vec{v}_r$ is one reflected ray corresponding to the shown position of the tangent plane. The directional vector $\vec{e}$ of the edge lies in the intersection of green facets.

revolution with the apex at the point of incidence of the incident ray. The axis of the cone is the intersection line of the two facets.

8.3 Solution

8.3.1 Parametrization

We locally approximate the edge by a plane tangential to the cylindrical shape of the edge.

We can always set the coordinate system in such a way that the point of incidence is in the origin of the coordinate system and $\vec{e}$ is in the z axis:

$$\vec{e} = \begin{pmatrix} 0 \\ 0 \\ 1 \end{pmatrix}, \tag{8.1}$$

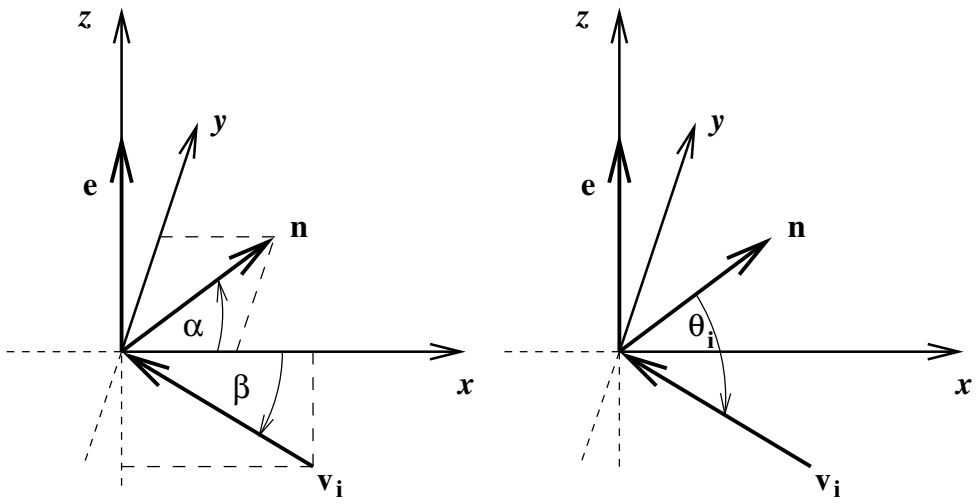

Figure 8.3: The parametrization of the incident vector $\vec{v}_i$, the tangent plane normal vector $\vec{n}$, and edge direction vector $\vec{e}$. The incident ray vector $\vec{v}_i$ is in xz plane, parameterized by angle β, the tangent plane normal vector $\vec{n}$ is in the xy plane, parameterized by the angle α. The incident angle θ_i is not coinciding with xy nor xz in the general case. Note the orientation of the incident vector $\vec{v}_i$ agrees with Fig. 5.1.

as well as the incident ray is in the xz plane. See Fig. 8.3. The directional vector of the incident ray can be written as

$$\vec{v}_i(\beta) \quad = \quad \begin{pmatrix} -\cos\beta \\ 0 \\ \sin\beta \end{pmatrix}, \tag{8.2}$$

where β is the angle between the incident ray and the directional vector of the intersection. The normal $\vec{n}(\alpha)$ of the approximating plane is

$$\vec{n}(\alpha) \quad = \quad \begin{pmatrix} \cos\alpha \\ \sin\alpha \\ 0 \end{pmatrix} \wedge \langle \alpha_1, \alpha_2 \rangle, \tag{8.3}$$

where α is from the interval $\langle \alpha_1, \alpha_2 \rangle$. The angles α_1, α_2 correspond to the normals $\vec{n}_1 = \vec{n}(\alpha_1)$ and $\vec{n}_2 = \vec{n}(\alpha_2)$ of the facets f_1, f_2, respectively. See Fig. 8.2.

Let us define $\eta_{12} = \eta_1/\eta_2$. Using Eq. 5.4, we can calculate the directional vector of the refracted ray as

$$\vec{v}_t(\alpha) \quad = \quad \begin{pmatrix} -\eta_{12}\sin^2\alpha\cos\beta + \cos\alpha\sqrt{1-{\eta_{12}}^2\sin^2\alpha\cos^2\beta - {\eta_{12}}^2\sin^2\beta} \\ \sin\alpha\left(\eta_{12}\cos\alpha\cos\beta - \sqrt{1-{\eta_{12}}^2\sin^2\alpha\cos^2\beta - {\eta_{12}}^2\sin^2\beta}\right) \\ \eta_{12}\sin\beta \end{pmatrix}. \tag{8.4}$$

The z component of the refracted ray does not depend on the parameter α. Remind that the direction vector of the edge $\vec{e}$ is $(0,0,1)^T$, see Eq. 8.1. The cosine of the angle γ between the edge directional vector $\vec{e}$ and the refracted vector $\vec{v}_t$ calculated using their dot product is

$$\cos\gamma = \vec{e}\cdot\vec{v}_t(\alpha) \quad = \quad \eta_{12}\sin\beta\,. \tag{8.5}$$

$\cos\gamma$ does not depend on the angle α which parameterizes the edge tangent plane. The cosine of the angle γ and hence the angle γ between transmitted ray $\vec{v}_t$ and edge directional vector $\vec{n}$ is constant. All transmitted rays pass through the point of incidence of the incident ray. Consequently, the refracted rays lie on the conical surface with the cone axis in the edge. See Fig. 8.4.

As the edge has a finite length, the incident rays illuminate the subset of the edge intersecting with the incident collimated beam. All the rays refracted by the edge are thus parameterized by two parameters. The first one is α running through the interval $\langle\alpha_1,\alpha_2\rangle$. The second parameter is running along the edge through the intersection of the edge and the incident beam.

We can calculate the directional vector of the reflected ray in the same way. This time, we shall set $\eta_{12}=1$ as incident and reflected rays are in the same material.

$$\vec{v}_r(\alpha) \quad = \quad \begin{pmatrix} -\sin^2\alpha\cos\beta + \cos\alpha\sqrt{1-\sin^2\alpha\cos^2\beta-\sin^2\beta} \\ \sin\alpha\left(\cos\alpha\cos\beta+\sqrt{1-\sin^2\alpha\cos^2\beta-\sin^2\beta}\right) \\ \sin\beta \end{pmatrix} \tag{8.6}$$

The refracted ray is on the conical surface with the cone axis in the edge axis. See Fig. 8.5.

Traces of edge rays exiting the beam

Let us consider the problem of estimation real stone shape parameters. The examined stone is inserted into the experimental setup shown in Fig. 4.2. The traces observed on the screen caused by beams exiting the stone are visible in Fig. 4.4. A detail is shown in Fig.8.1.

When a beam hits two neighboring facets it illuminates also the part of the edge connecting them. The beam splits into four sub-beams, two refracted out, two reflected in. Let us discuss the pair of exiting beams. The exiting beam can be reflected beam from the third layer, see Fig. 6.2. The exiting beam can be refracted beam from next odd layers as well. See Chapter 6. The reasoning is similar in both cases so we will discuss here the refracted beams.

The two refracted beams produce beam traces on the screen. The rays refracted by the edge lie on the part of a conical surface with the axis in the edge. The intersection of this cone with the screen is a trace of the edge rays.

The traces of the rays refracted by the edge connect the traces of the beams refracted by facets neighboring the edge. The edge rays traces are rarely fully visible

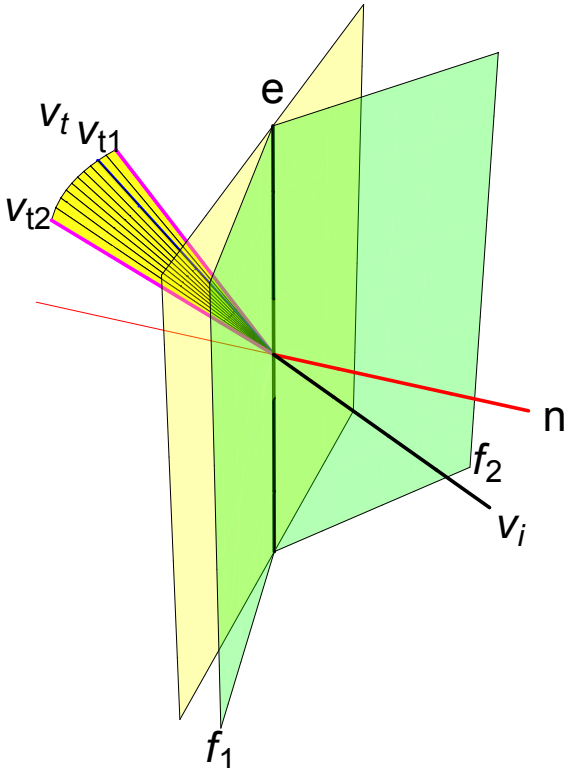

Figure 8.4: The figure shows the *refracted* rays on the smooth transition between two facets. The incident ray $\vec{v}_i$ is shown in black. f_1 and f_2 are two planes of the facets represented by the green semitransparent rectangles. Their intersection is in black and labeled $\vec{e}$. The rays refracted by the facets/planes f_1 and f_2 are shown in magenta and labeled $\vec{v}_{t1}$ and $\vec{v}_{t2}$. One particular plane tangent to the cylindrical part approximating smooth transition from the planes f_1 to f_2 is shown in the light yellow color. Its normal is labeled $\vec{n}$ and shown in red, with the thin extension to the outer environment. The ray refracted by this particular plane is shown in blue and labeled $\vec{v}_t$. All refracted rays from the smooth transition are shown by the yellow cone part.

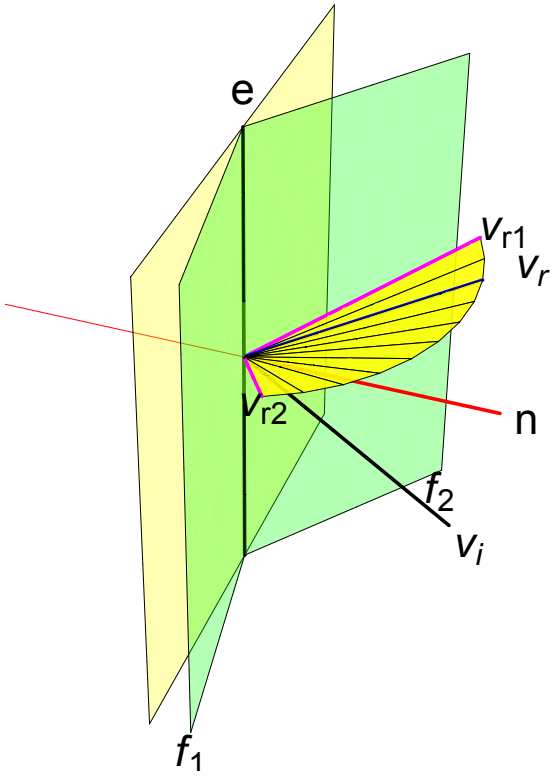

Figure 8.5: The figure shows the *reflected* rays on the smooth transition between two facets. The incident ray $\vec{v}_i$ is shown in black. f_1 and f_2 are two planes of the facets represented by the green semitransparent rectangles. Their intersection is in black and labeled e. The rays reflected by the facets/planes f_1 and f_2 are shown in magenta color and labeled $\vec{v}_{r1}$ and $\vec{v}_{r2}$. One particular plane tangent to the cylinder part approximating smooth transition from the planes f_1 to f_2 is shown in the light yellow color. Its normal is labeled $\vec{n}$ and shown in red, with the thin extension to the outer environment. The ray reflected by this particular plane is shown in blue and labeled $\vec{v}_r$. All reflected rays from the smooth transition are shown by yellow cone part.

in an image of the screen, as its central part has low intensity. We call the visible parts of the edge rays trace *protrusion*.

Rays refracted from the edge lie on a cone with circle base. We assume further the stone is small compare to the screen size and its distance to the stone. Edge rays traces shape depends on the screen shape. For hemispherical screen with the center in the stone, the shapes of the protrusion traces is a circular arc with the ends in the facet beams traces. This circular arc shape is a result of intersection of the screen sphere and the cone with the circular base and the cone apex in the sphere center. For planar screen, the protrusion trace shape is a conic. The shape is given by the intersection of the rays cone with the circular base and the screen plane. See Fig. 8.6.

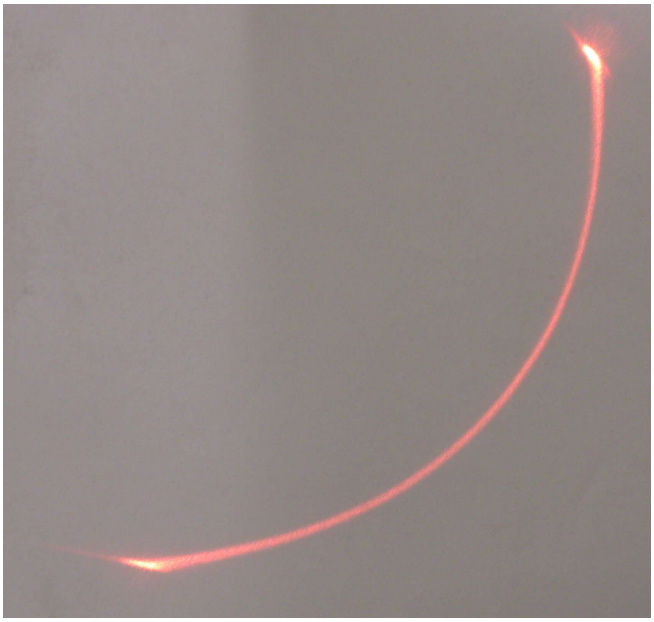

Figure 8.6: The beam trace refracted by two neighboring facets and an edge between them. The traces refracted from facets are bright spots in the lower left and upper right corner, the light refracted by a round edge is the red arc connecting them. The screen is planar in this case. The intersection of the cone and the planar screen results in a part of an ellipse. Note that this image was obtained on a very large stone with a very localized incident beam. However, this is the experimental confirmation that the protrusions are not only local features of the traces but they connect even distant traces.

One has to take into account the actual shape of the experimental setup, including the position of the stone, the position and the shape of the screen, the position and the optics of a camera. One can estimate the direction (tangent line) of the protrusion in the image from the known geometry of the experiment. The estimated direction of protrusions can be used for matching between simulated beams and detected traces in the image.

Traces of edge rays reflected or refracted into the stone

The description above deals with beam traces connected by edge rays traces when the beam exits from the stone. A similar analysis holds for beams and rays reflected back to the stone. However, the situation is more complicated here.

Let us pose the following question. Do all beam traces from a stone with round edges have protrusions? The answer is yes.

The simulated beams reflected or refracted by an edge approximated by narrow facets can be visualized in 3D, see Fig. 8.7. The reflected light from an edge into the stone is analyzed in the figure. The light refracted by the edge out of the stone is not restricted by the stone anymore. The light rays reflected and diverged by the edge into the stone can pass through the different sequence of facets than the beam reflected from the edge neighboring facets.

Let us study the solid angle, in which the light reflected from an edge propagates. We have to broaden our model a little bit for this analysis. We assume that the size of the stone is small compared to the size of the screen where we observe beam traces. Under such assumptions, we can ignore the cross-section of the beam as the beam trace is quite small compared to the size of the screen. In addition, the slight divergence of the originally collimated beam caused by non-planarity of facets blurs the shape of the beam trace on the screen.

However, rays reflected by edges diverge into a solid angle. The solid angle is large enough to contain facets which the elementary beam illuminating the studied edge is not reflected to. That means some rays reflected by edges are later on their path totally reflected or they are refracted to new directions. The diverged rays traces are reflected or refracted to new directions and the protrusion observed on the screen stops suddenly.

Thus it is important to ask, whether the cone of the divergent beam reflected from the edge intersects or is disjunctive to the 3D space occupied by collimated beam.

The former is the case because the reflection or refraction from the edge intersects the reflected or refracted original beam as shown in Fig. 8.8. One can conclude: A small part of the reflected edge rays will pass through the same sequence of the facets at least. Their trace will be partly visible at least. One can expect to see at least small protrusions for each trace and each edge. This agrees with the computer simulation as shown in Fig. 8.7.

8.4 Experimental results

We have experimented with the simulation of edges in the LADOK program package [145]. The original LADOK does not support round edges. The round edges were approximated by a sequence of narrow facets as shown in Fig. 8.9. The simulation of the beams transmitted from the stone are shown in Fig. 8.10. The implementation is described in [199].

The images of the edge rays observed on the real product are shown in Fig. 8.11 and 8.6.

We have further extended the LADOK program with the visualization of the rays

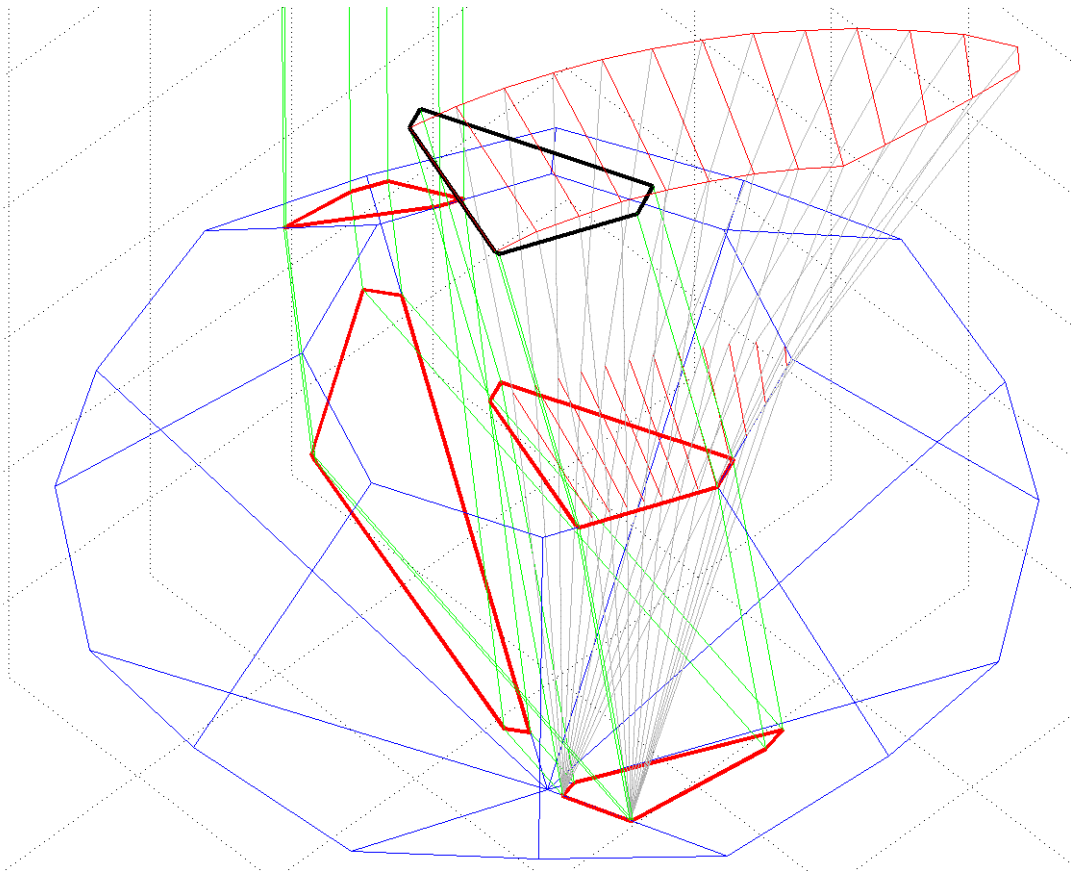

Figure 8.7: 3D visualization of a beam reflected from a single round edge. The elementary beam is shown in green. The input beam enters the upper facet. It is reflected twice by lower facets and exits the stone through the table of the stone. The round edge between two lower facets is modelled by a sequence of many narrow facets. They produce many narrow beams which are reflected up. They are next cut out partly by the table (see the right part of the exiting beams). The cross-section of the original exiting beam is shown in black. The round edge restricts bottom left side of the black polygon.

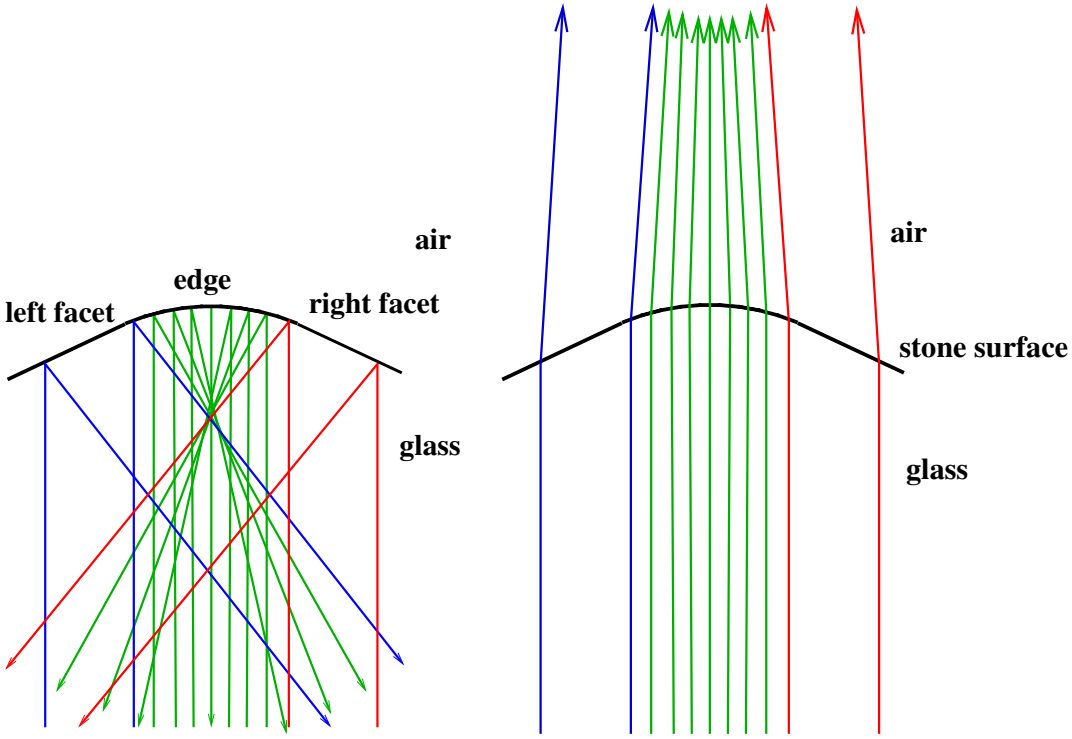

Figure 8.8: The spatial distribution of the rays reflected (left) and refracted (right) from a round edge. The beam incident and reflected/refracted from the left facet is drawn in blue, the beam interacting with the right facet is drawn in red. The rays reflected/refracted by the edge are drawn in green. The green reflected/refracted rays intersect with the area occupied by blue/red beams.

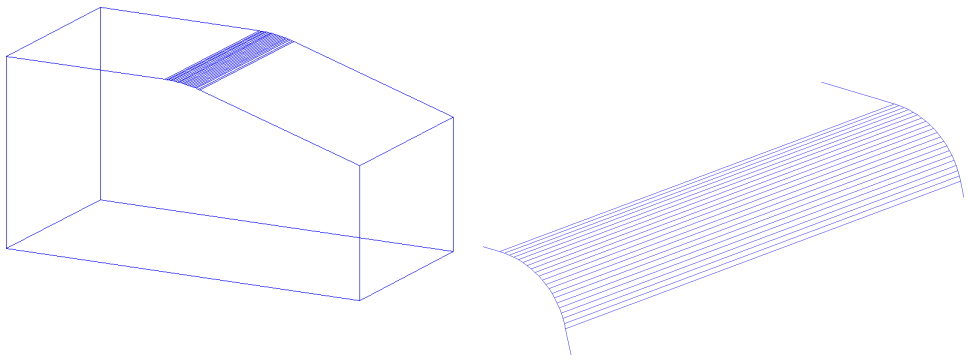

Figure 8.9: The approximation of the round edge. The round edge was approximated by several narrow planar edges on the stone (left). The detail of the edge with the larger scale of angles is shown in the right.

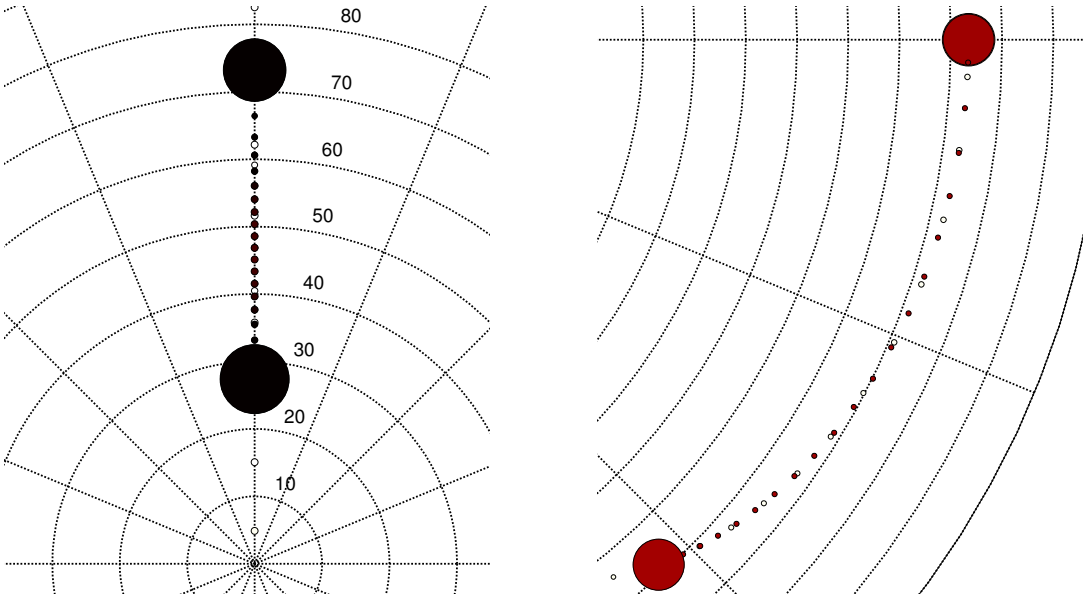

Figure 8.10: The simulation of the beams refracted by the round edges. The large circles are the beams from stone facets. Small dots correspond to the light rays refracted from the edge approximating facets and they connect the main beams. LADOK visualizes its results in polar coordinates where the radius represents the elevation and the angle represents the azimuth of the beam. The edge rays lie on the cone, which is in polar coordinates transformed into a straight line (left) or an arc (right). The small filled circles correspond to the beams refracted or reflected by approximating narrow facets. The empty circles correspond to other edges not relevant here. LADOK SW codes the area of the beam into the area of the circle and intensity of the beam into color filling the circle.

refracted on the edges. The directions of the trace protrusions were calculated and short straight lines were drawn in the simulation visualization. The lines originate in the beam traces. Their lengths are proportional to the lengths of the edges for visualization purposes. Lines in the simulation are expected to be tangent to the observed protrusions. The simulated length of the line need not correspond to the visible protrusion. The camera sensitivity and noise does not allow to detect the protrusions with low intensity.

The visualizations of edge rays by beams refracted from approximation of the edge by narrow facets and by short tangent lines are shown in Fig. 8.12. Both approximations are in a good agreement.

The scenario described in Sec. 4.4 is visualized in the Fig. 8.13. The traces of the beams including protrusions from edge rays are shown in the image top. The simulation of edge rays is shown in bottom. One can compare both images to find correspondences. Further development is intended to automate finding correspondences.

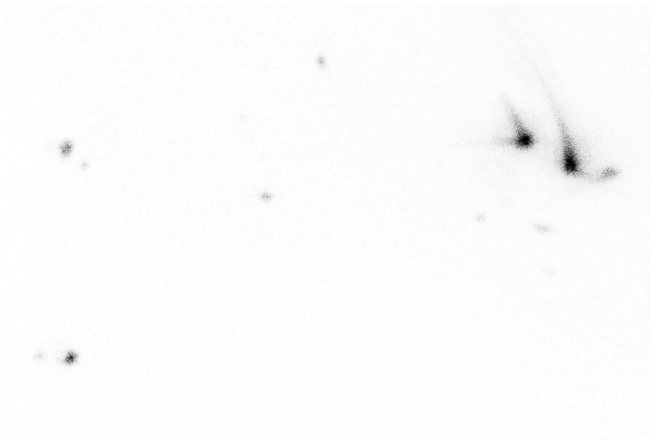

Figure 8.11: The traces of the exiting beams visible on the planar screen. They have visible protrusions, which are caused by refractions and reflections on the facet edges. The image brightness is inverted for better visibility.

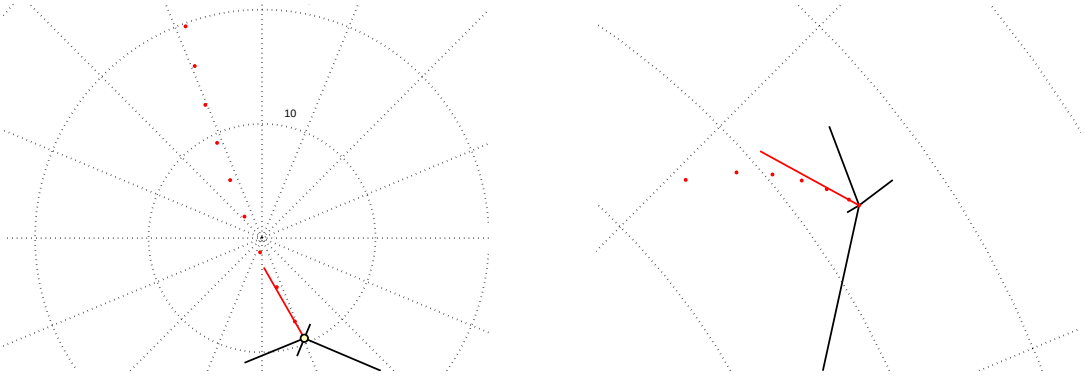

Figure 8.12: Two different visualizations of simulated protrusions. Small circles are beams refracted and reflected by narrow planar facets such as in Fig. 8.9. Lines are local tangent lines to the edge rays trace. The beams represented by small circles are shown only for red tangent line.

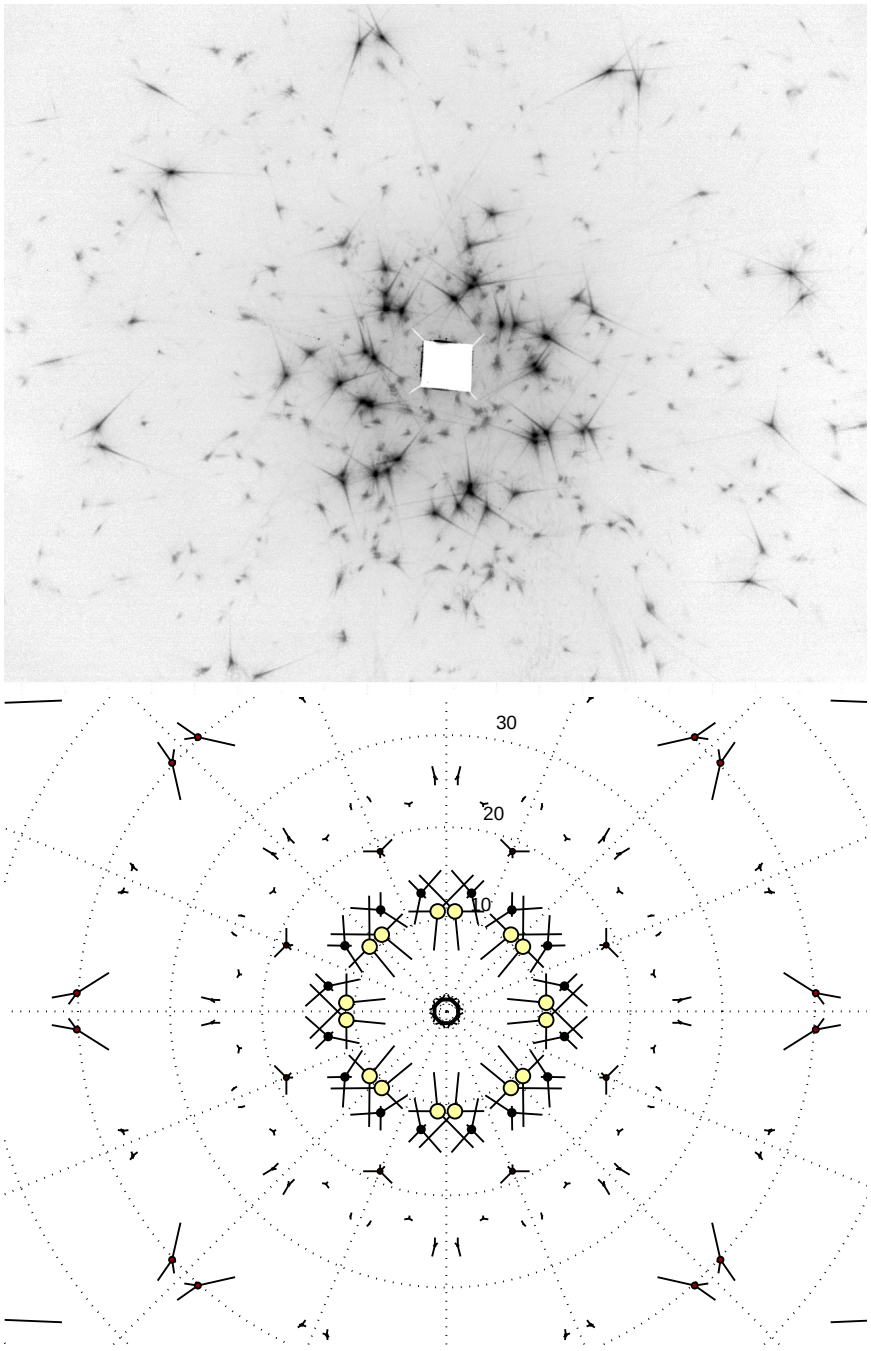

Figure 8.13: Top: An experiment with a chaton. The image shows beams coming from the chaton illuminated by a laser. The image brightness is inverted for clarity. The image is repeated from Fig. 4.4 to facilitate comparison [83]. Bottom: The visualization of the LADOK simulation with the simulated protrusions from the beam traces. The visualization corresponds to the experiment shown above. The additional information about the protrusions makes the correspondence problem easier.

We experimented with a third way how to simulate and visualize edge ray traces. A local normal $\vec{n}$ of the edge is a function of the parameter α. Angle α is from the interval $\langle \alpha_1, \alpha_2 \rangle$, see Fig. 8.3 and Eq. 8.3. The angle α was sampled in the interval $\langle \alpha_1, \alpha_2 \rangle$ and corresponding refracted or reflected rays were ray-traced until they exited the stone. This method enables modelling of edge rays traces with predefined resolution.

Edge rays traces start in the beam trace and can end up in the beam trace of the neighboring facet. The second beam trace need not exist as the incident beam can be totally reflected at neighboring facet. The sampling of the angle α stops when the incident beam is totally reflected. The situation is shown in Fig. 8.14. The beam exiting the stone produces a trace labeled by large black dot. The beam shown has a pentagonal cross-section. The cross-section sides are defined by five edges which constrain the beam during its path through the stone. Five edge rays traces are shown in Fig. 8.14. One edge rays trace finishes in the neighboring beam trace labeled by small black dot. Four other edge rays traces finish in red crosses. Red cross label the ray where critical angle for total reflection is reached or the ray reflected from the edge hits the facet different than the beam corresponding to the large black dot trace. See Section 8.3.1.

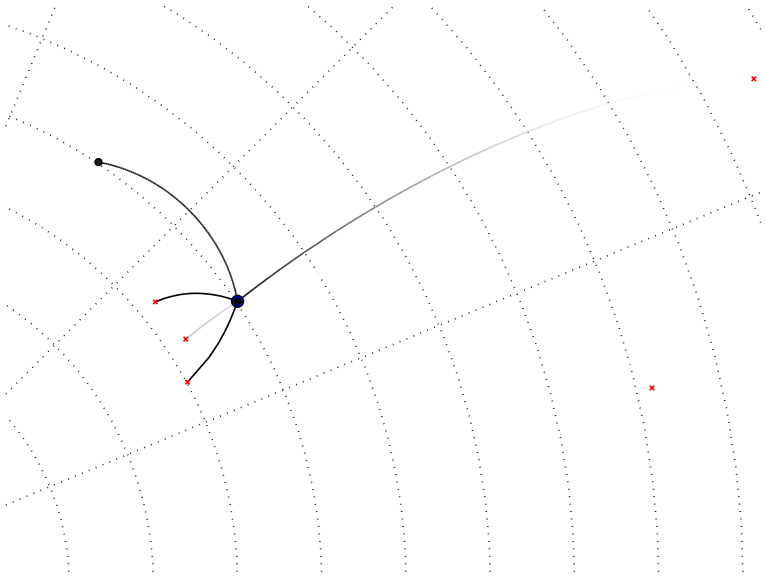

Figure 8.14: This figure shows simulated edge ray traces of rays refracted or reflected on a round edge. The large black dot corresponds to the trace of an elementary beam. The beam has pentagonal cross-section as it is restricted by five edges. The edge rays correspond to the black arcs. One arc ends up in the small black dot representing beam refracted by neighboring facet. The other four arcs end in red crosses. The edge rays corresponding to red crosses were either totally reflected so they cannot refract out from the stone or were refracted or reflected by other facets.

8.5 Applications

8.5.1 Comparison to the reality

An approximation of an edge between two facets by a smooth surface is realistic. There are several reasons why edges of the manufactured stones are round .

1. Safety: Edges are manufactured slightly rounded to avoid cutting objects interacting with stones.

2. Durability: Objects made from fragile materials are particularly vulnerable to cracks originating in sharp edges. Even a small crack at the edge can propagate through the material and may results in breaking the fragile object into pieces. Hence when objects are machined from glass and similar materials, the edges are chamfered to prevent cracking. Optical lenses, prisms, etc. are manufactured this way.

3. Technology: Sharp edges are more vulnerable to material loss during grinding and polishing. The manufacturing process thus inherently produces rounded edges between facets.

A stone with visibly rounded edges is shown in Fig. 8.15.

The resulting cylindrical shape of an edge can be described roughly as having a hyperbolic cross-section. The almost flat part of the facet starts to curve with the maximal curvature in the middle and then the curvature decreases until it reaches the second flat facet.

We are not interested in a specific edge profile in our analysis. The trace intensity corresponds roughly to the inverse curvature of the edge. Indeed, one can observe this effect in experimental data. The trace protrusions intensity is high at positions close to the traces and almost undetectable in between. See Fig. 8.11 and 8.6.

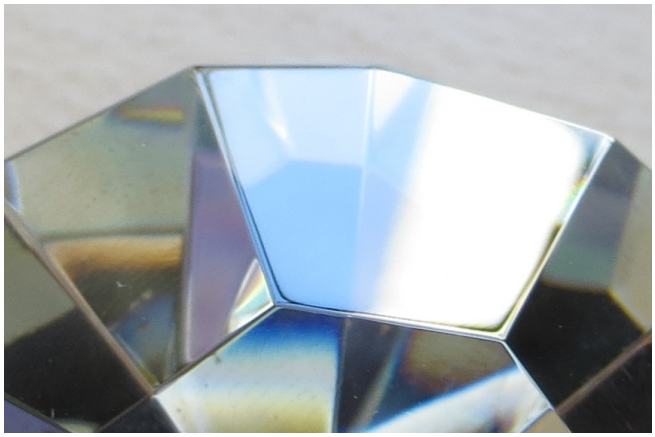

Figure 8.15: A glass stone with the round edges.

8.5.2 The fidelity of the edge mathematical model

Although one can hardly claim that the smooth transition between two edges is cylindrical with circular base, it is clear that it has a tangent plane at each point. The normal vector of the tangent plane is perpendicular to the direction of the edge. Hence we can approximate the smooth surface locally by a tangent plane whose normal vector can be written as $\vec{n} = (\cos\alpha, \sin\alpha, 0)^\top$. When passing smoothly from the plane of the facet f_1 to the plane of the facet f_2, the parameter α is not changing with the constant velocity but its change starts slowly, then it speeds up, and finally it slows down again. Our analysis relies on approximation of the edge by tangent planes but not on the particular shape of edge in form of cylinder with the circular base.

8.5.3 Comparison to observed refracted ray traces

Fig. 8.11 shows the traces coming from the facets with protrusions with very quickly decreasing intensity. The fast decrease of the intensity nicely corresponds to the physical shape of an edge with a non-constant curvature in the plane perpendicular to the edge. If the shape of the edge was cylindrical with the circular base, the intensity of the trace corresponding to the edge would be roughly constant. Under good conditions, the whole trace corresponding to the edge is visible as shown in Fig. 8.6.

Chapter 9

Reflection and Refraction on the Stone First Surface

9.1 Introduction

The amount of light returned to the upper hemisphere of the stone is one of the crucial parameters describing the stone quality. This criterion is not the only one but it falls among the most studied ones. Popular shapes of cuts of diamonds were designed using simplified calculation mainly based on this criterion [170].

9.1.1 Ray-tracing

Ray tracing [154] can be used to evaluate the amount of returned light. A user selects a configuration of light sources and position of a camera. The light sources illuminate the stone. The camera measures the amount of light returned from the stone. The ray-tracing program is used to generate the image of the illuminated stone captured by the camera. The amount of light returned to the camera from the stone is divided by the amount of light incident on the stone to get ratio which is used for assessing the quality of the stone.

The critical part of the ray tracing is the selection of right illuminating rays. The ray propagation in the stone is sensitive to input conditions. Input rays with the similar parameters can end up exiting into upper or lower hemisphere after propagation in the stone. The rays, which are used for probing the stone, are being selected from the four-dimensional space corresponding to the azimuth and elevation of the ray directional vector and spatial coordinates of some point on the ray. It is time consuming to sufficiently sample a four dimensional space.

The camera has to be selected from a two dimensional space, corresponding to the azimuth and the elevation of the optical axis. We are neglecting the camera resolution and other parameters. One could use a panoramic camera looking towards the stone center to avoid this second sampling. The open question remains whether selected ray-tracing program allows such a camera.

To conclude, ray tracing is not accurate and it is time consuming [107].

9.1.2 Beam modeling

Our previous method [145] illuminates stones by light beams defined by the azimuth, elevation, polygon of the beam cross-section, and Stokes parameters.

The beams are tracked in a stone, while they reflect, divide into sub-beams on the stone edges, and refract out of the stone. The result of modeling is a set of sub-beams exiting the stone.

The radiant flux of the light exiting into useful directions (usually to the upper hemisphere) can be computed and compared to the radiant flux of incident light.

The method is accurate for each illuminating beam (neglecting the rounding errors). One can control the accuracy required by controlling either the number of reflections allowed or the total amount of energy still in the game. Unfortunately, one still has to sample a 2D space, i.e. azimuth and elevation, of incident beams.

9.1.3 Other approaches

More general approaches, which admits more general scenes, e.g. scattering media and matte surfaces [124] or continuously varying refraction index of the media [74], are described in the literature. The optical effects taken into account in these approaches do not admit using analytic methods. Consequently, various versions of Monte Carlo [124, 86], photon mapping [74], radiosity [104] and other [168] methods are used. These methods solve a much more general problem at the cost of long computational time.

As we consider a special case with planar optically smooth surfaces and planar waves, we can use a much simpler approach.

9.2 Problem statement

We would like to answer the following question. Is there any method allowing to evaluate the whole set of possible illumination rays at once without sampling the space of rays or the space of beams?

We have found the following partial answer:

- One can calculate the amount of reflected light from the external reflection. That is the light ray coming from the air is directly reflected back. One can calculate the amount of light reflected to the upper hemisphere and to the lower hemisphere separately.
- One can calculate the amount of light, which is refracted into the stone from the air. This light undergoes further reflections and refractions. It can be returned to the upper hemisphere as well as to the lower one which results in the light loss.

Let us specify the following task:

1. The stone has the upper side, where the stone table is facing, and the lower side.

2. The illumination comes uniformly from the hemisphere corresponding to the stone upper side, see Fig. 9.1. One can model here nonuniform illumination e.g. accenting directions close to z axis.

3. The light reflected to the upper hemisphere is considered as a positive contribution to the stone quality. One can model here nonuniform sensitivity depending on the elevation.

4. The light reflected to the lower hemisphere is considered as lost and thus contributes negatively to the stone quality.

5. The light refracted into the stone is considered as positive as it can be later refracted to the upper hemisphere with possible dispersion to enhance the stone fire as well as it can be refracted to the lower hemisphere or it can be even diffused on edges or not polished parts of the stone surface.

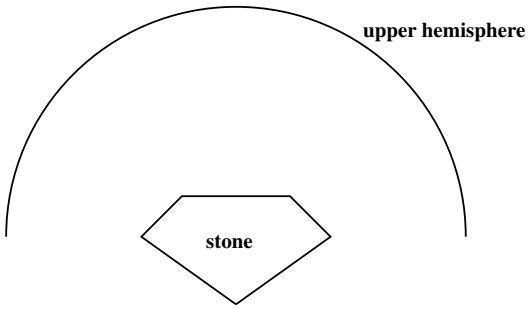

Figure 9.1: The standard assumptions about the stone illumination. The lower side of the stone is inserted into a jewel holder or attached to a surface. The stone is illuminated from above. Only light reflected or refracted to the upper hemisphere is useful. We use the hemisphere with infinite radius in our model.

9.3 Model of the light source and light return

Note that we consider only the first contact of the light with the stone surface in this model.

The light in this particular model will be modeled as coming from the hemisphere with the infinite radius. The hemisphere is the uniform source light from all directions. Each facet will be modeled independently. The facets facing down will be ignored as they are hidden in the stone holder.

Under the above conditions, one can calculate the following quantities for each facet:

- The amount of light (radiant flux) falling onto the facet Φ_{on}.
- The amount of light reflected by the facet to the upper hemisphere Φ_{up}.

- The amount of light reflected by the facet to the lower hemisphere (lost) Φ_{down}.
- The amount of light refracted into the stone via the facet Φ_{in}.

9.3.1 Incident light

The formula for calculating the incident radiant flux is

$$\Phi = \int_{\Omega}\int_{S} L \cos\theta_i \,\mathrm{d}S\,\mathrm{d}\Omega\,, \tag{9.1}$$

where θ_i is the incident angle of the ray. The double integral notation used here is

$$\int_a\int_b c\,\mathrm{d}b\,\mathrm{d}a = \int_a \left(\int_b c\ \mathrm{d}b\right)\mathrm{d}a\,. \tag{9.2}$$

Its cosine gives the area of the facet projection onto the plane perpendicular to the ray.

The radiance L expresses the amount of light radiated by the hemisphere as seen by the stone into certain solid angle and certain area. It is constant in our case. The facet is planar with the known area S. The formula simplifies to

$$\Phi_{on} = LS\int_{\Omega}\cos\theta_i(\Omega)\,\mathrm{d}\Omega\,. \tag{9.3}$$

The upper side of the stone is facing up in the direction of the z axis. The illuminating hemisphere is in the half-space with $z > 0$.

We can assume in our analysis without loss of generality that the normal of the facet is in the xz plane, since the facet can be rotated around the z axis as the illuminating hemisphere is symmetrical around the z axis. As the hemisphere has an infinite radius, the origin of the coordinate system can be located in the plane of the facet. The geometrical position of the facet is thus parameterized only by one parameter β, which is the angle between z axis and facet normal $\vec{n}$, i.e.

$$\vec{n}(\beta) \;=\; \begin{pmatrix} \sin\beta \\ 0 \\ \cos\beta \end{pmatrix}. \tag{9.4}$$

The reversed directional unit vector of the ray $\vec{e}(\alpha,\epsilon)$ is parameterized by its azimuth α and elevation ϵ:

$$\vec{e}(\alpha,\epsilon) \;=\; \begin{pmatrix} \cos\epsilon\cos\alpha \\ \cos\epsilon\sin\alpha \\ \sin\epsilon \end{pmatrix}. \tag{9.5}$$

The horizon has the elevation equal to 0, see Fig. 9.2.

The sine and cosine of the incidence angle can be calculated as

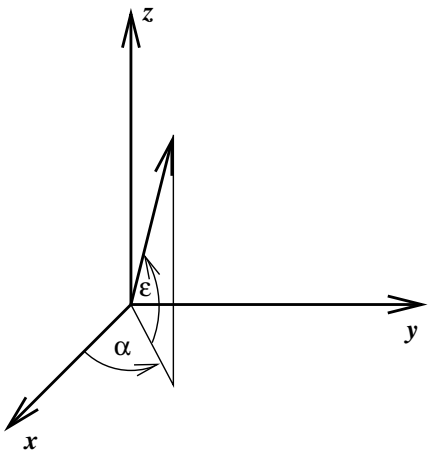

Figure 9.2: Parametrization of the incident ray by the azimuth α and the elevation ϵ. Azimuth is measured in xy plane from the x axis and the elevation is measured from xy plane towards the ray.

$$\sin\theta_i = |\vec{n}\times\vec{e}|\,, \tag{9.6}$$
$$\cos\theta_i = \vec{n}\cdot\vec{e}\,, \tag{9.7}$$

where $\times$, $\cdot$ mean cross respectively scalar product.

The radiant flux falling onto the facet Φ_{on} is proportional to the part of the hemisphere, which is above the plane of the facet, see Fig. 9.3 and Fig. 9.4. The solid angle Ω in Eq. 9.3 is defined by the hemisphere part bounded by horizontal xy plane and the facet plane passing trough y axis which has the angle β between z axis and its normal, see Fig. 9.3.

The integration is done here separately for $x > 0$ and $x < 0$ case. The integration limit ϵ_{min} is calculated by solving the equation

$$\vec{e}(\alpha,\epsilon_{min})\cdot\vec{n} = 0\,. \tag{9.8}$$

The ϵ_{min} is thus a function of α, β. The integral can be rewritten as

$$\Phi_{on} = LS\left(\int_{-\pi/2}^{\pi/2}\int_{0}^{\pi/2}\cos\theta_i\,\mathrm{d}\epsilon\,\mathrm{d}\alpha + \int_{\pi/2}^{3\pi/2}\int_{\epsilon_{min}}^{\pi/2}\cos\theta_i\,\mathrm{d}\epsilon\,\mathrm{d}\alpha\right) \tag{9.9}$$
$$\epsilon_{min} = \operatorname{argtan}(-\cos\alpha\sin\beta,\cos\beta)\,. \tag{9.10}$$

The first integral can be integrated as $2\sin\beta + \pi\cos\beta$. The second can be integrated only partially with the partial result $-2\sin\beta$. The part $\sqrt{\cos^2\alpha\sin^2\beta + cos^2\beta}$ has to be integrated numerically. Even this integral can be integrated analytically

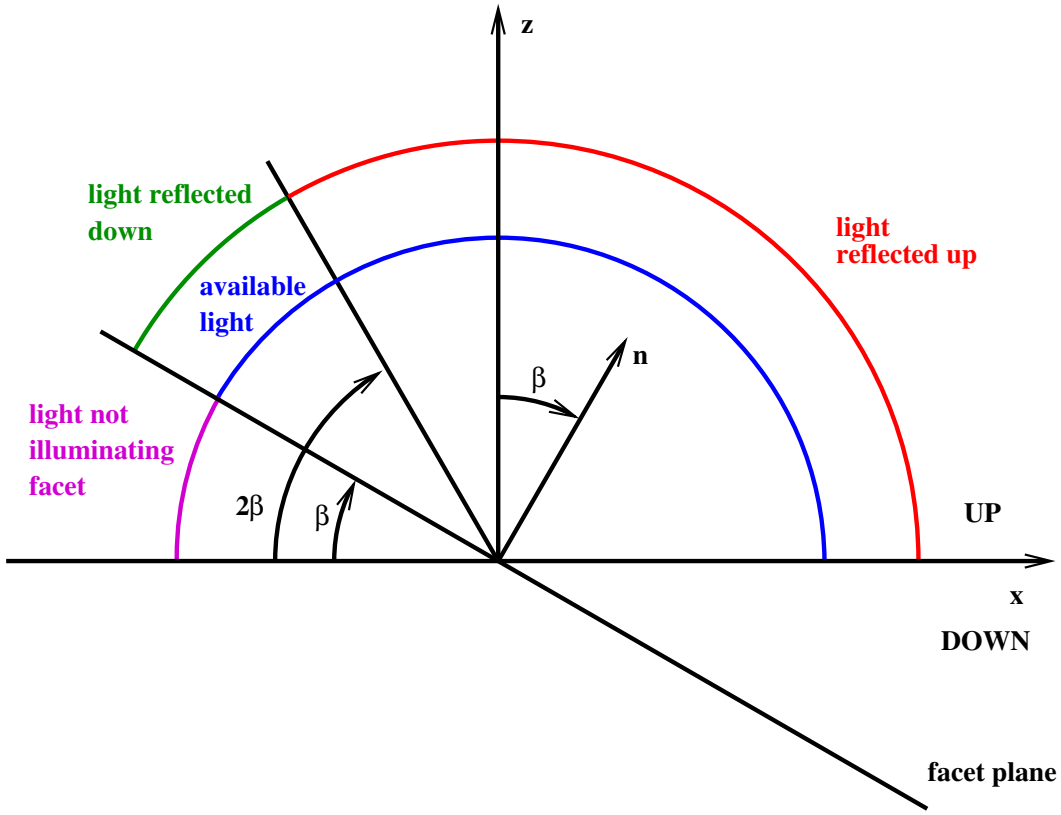

Figure 9.3: The integration of light falling onto the facet from the hemisphere. The drawing shows the xz plane cross-section of the situation with the facet tilt angle $\beta \leqq \pi/4$. The blue arc shows the part of the hemisphere from which light falls onto the facet. Some of this light is refracted into the stone, the rest is reflected. The red arc shows the part of the hemisphere from which light is reflected up. The green arc shows the part from which light is reflected down. The light from the hemisphere not illuminating the facet upper side is shown in magenta.

into a form containing elliptical functions but this is probably not better than the original integral. The integral can be simplified into the form

$$\begin{aligned} \Phi_{on} &= LS(2\sin\beta + \pi\cos\beta - 2\sin\beta + \int_{\pi/2}^{3\pi/2} \sqrt{\cos^2\alpha\sin^2\beta + cos^2\beta}\,\mathrm{d}\alpha) = \\ &= LS(\pi\cos\beta + \int_{\pi/2}^{3\pi/2} \sqrt{\cos^2\alpha\sin^2\beta + cos^2\beta}\,\mathrm{d}\alpha)\,. \end{aligned} \tag{9.11}$$

9.3.2 Reflected light

The part of the light incident onto the facet is reflected back. The amount of reflected light using Fresnel formulae 5.13 is

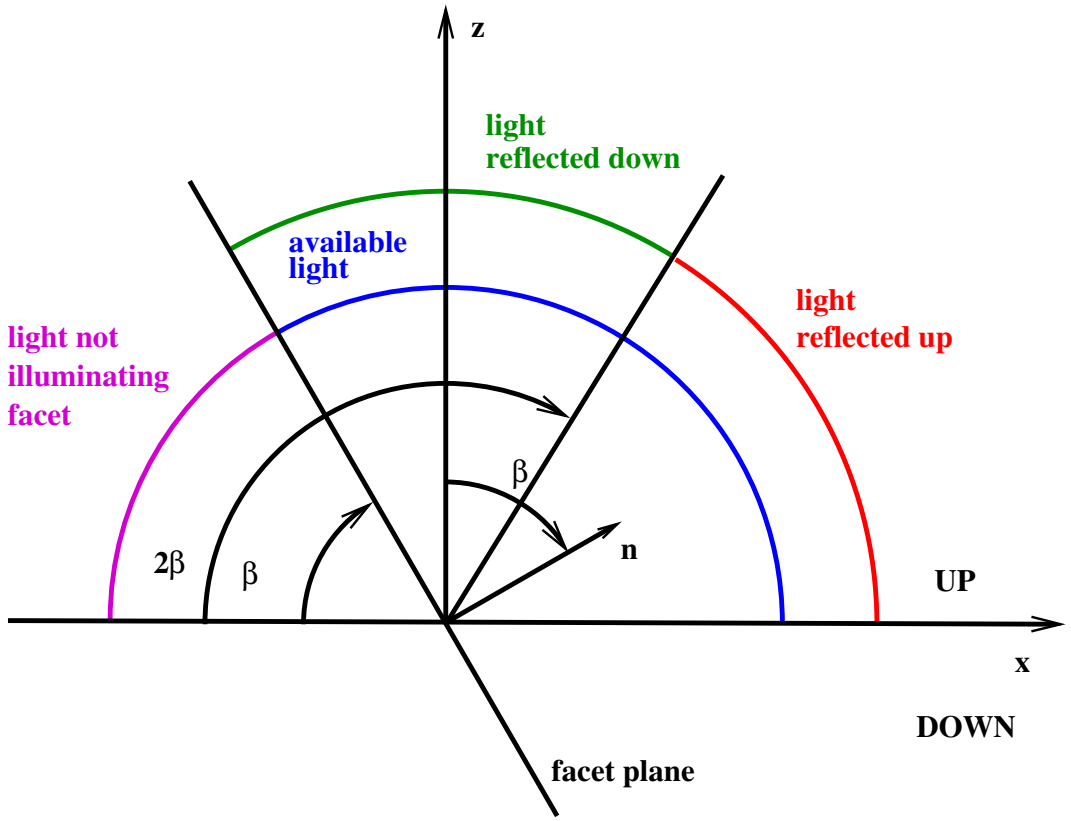

Figure 9.4: The integration of light falling onto the facet from the hemisphere. The drawing shows the xz plane cross-section of the situation with the facet tilt angle $\beta > \pi/4$. The blue arc shows the part of the hemisphere from which light falls onto the facet. Some of this light is refracted into the stone, the rest is reflected. The red arc shows the part of the hemisphere from which light is reflected up. The green arc shows the part from which light is reflected down. The light from the hemisphere not illuminating the facet upper side is shown in magenta.

$$\Phi \quad = \quad S \int_{\Omega} (|r_{\parallel}|^2 L_{\parallel} + |r_{\perp}|^2 L_{\perp}) \cos\theta_i \, \mathrm{d}\Omega \,. \tag{9.12}$$

The common assumption for evaluating stones will be that $L_{\parallel} = L_{\perp} = L/2$.

One has to stress that regarding polarization, we have two different situations:

- The incident light is indeed unpolarized in most applications of a stone. It comes from light bulbs, fluorescent tubes, wax candles etc. Although LED diodes are often used now, the chips are usually covered by luminophore, which effectively unpolarizes the light.

The stone is rarely illuminated by a laser, if so then mostly for research or inspection purposes. In the latter case, the computation with the polarized incident light is required.

- The light is polarized by reflection and refraction. Hence one has to compute beams radiometric parameters using a polarized light model. In the context of this chapter, we are not studying those reflected beams.

Light reflected up. One has to ignore the rays, which are reflected to the lower hemisphere, that is the rays bellow the plane passing through the y axis and having the angle between z axis and its normal 2β, see Fig. 9.3.

The integration is divided into two cases. When $\beta \leqq \pi/4$, the integration will be divided, similarly to the incident light case, into the two integration domains. The first one is the first quadrant in xz plane. The second is the part of hemisphere between yz plane and the plane tilted by 2β from the xy plane. For $\beta \geqq \pi/4$, the integration domain is between xy plane and the plane rotated by 2β around y axis from the xy plane, see Fig. 9.4.

$$\begin{aligned}
\Phi_{up} &= \frac{LS}{2}\int_{-\pi/2}^{\pi/2}\int_{0}^{\pi/2}(|r_{\parallel}|^2+|r_{\perp}|^2)\cos\theta_i\,\mathrm{d}\epsilon\,\mathrm{d}\alpha + \\
&\quad +\frac{LS}{2}\int_{\pi/2}^{3\pi/2}\int_{\epsilon_{min}}^{\pi/2}(|r_{\parallel}|^2+|r_{\perp}|^2)\cos\theta_i\,\mathrm{d}\epsilon\,\mathrm{d}\alpha \\
&\quad \text{for } \beta \leqq \pi/4 \text{ and} \\
\epsilon_{min} &= \operatorname{argtan}(-\cos\alpha\sin 2\beta, \cos 2\beta)\,, \qquad (9.13) \\
\Phi_{up} &= \frac{LS}{2}\int_{-\pi/2}^{\pi/2}\int_{0}^{\epsilon_{max}}(|r_{\parallel}|^2+|r_{\perp}|^2)\cos\theta_i\,\mathrm{d}\epsilon\,\mathrm{d}\alpha \\
&\quad \text{for } \pi/4 < \beta < \pi/2 \text{ and} \\
\epsilon_{max} &= \operatorname{argtan}(\cos\alpha\sin 2\beta, -\cos 2\beta)\,. \qquad (9.14)
\end{aligned}$$

The integrals have to be calculated numerically.

Light reflected down. The computation of the amount of light reflected down has to be divided again into two cases depending on β as shown in Figures 9.3 and 9.4

$$
\begin{aligned}
\Phi_{down} &= \frac{LS}{2}\int_{\pi/2}^{3\pi/2}\int_{\epsilon_{min}}^{\epsilon_{max}}(|r_{\parallel}|^2+|r_{\perp}|^2)\cos\theta_i\,\mathrm{d}\epsilon\,\mathrm{d}\alpha \\
&\quad \text{for } \beta \leqq \pi/4 \text{ and} \\
\epsilon_{min} &= \operatorname{argtan}(-\cos\alpha\sin\beta, \cos\beta) \text{ and} \\
\epsilon_{max} &= \operatorname{argtan}(-\cos\alpha\sin 2\beta, \cos 2\beta)\,, \qquad (9.15) \\
\Phi_{down} &= \frac{LS}{2}\int_{-\pi/2}^{\pi/2}\int_{\epsilon_{max}}^{\pi/2}(|r_{\parallel}|^2+|r_{\perp}|^2)\cos\theta_i\,\mathrm{d}\epsilon\,\mathrm{d}\alpha + \\
&\quad +\frac{LS}{2}\int_{\pi/2}^{3\pi/2}\int_{\epsilon_{min}}^{\pi/2}(|r_{\parallel}|^2+|r_{\perp}|^2)\cos\theta_i\,\mathrm{d}\epsilon\,\mathrm{d}\alpha \\
&\quad \text{for } \pi/4 < \beta < \pi/2 \text{ and} \\
\epsilon_{min} &= \operatorname{argtan}(-\cos\alpha\sin\beta, \cos\beta)\,, \\
\epsilon_{max} &= \operatorname{argtan}(\cos\alpha\sin 2\beta, -\cos 2\beta)\,. \qquad (9.16)
\end{aligned}
$$

The light reflected up, down, and transmitted depend on the area and tilt of the facet, and refraction index of the material. One can prepare in advance a look-up table for given material of the reflected light as a function of the angle *beta*. The optimization of even complex cut shapes can avoid numerical calculation of integrals.

9.3.3 Transmitted light

Transparent clear material. The transmitted light can be calculated using transmission Fresnel coefficients as

$$\Phi_{in} = \Phi_{on} - \Phi_{up} - \Phi_{down}\,. \qquad (9.17)$$

Transparent absorbing material. The transmitted light for highly absorbing transparent materials is almost completely absorbed. The light is reflected from the stone surface independently of their interior. The amount of light reflected up completely describes the light returned from highly absorbing stones.

Translucent material. The objects made from translucent, scattering, material with smooth specular surface are well studied in computer vision literature [167].

It is possible to extend our model for translucent objects. The reflections of light in stone interior can be neglected. The light transmitted to the stone are partially absorbed and partially scattered and refracted back. This can be well modelled by our integral approach.

9.4 Examples

9.4.1 The light incident on single planar facet

The radiant flux of the light incident from the upper hemisphere on a planar facet with orientation specified by angle β is divided into parts as discussed above. In the

following diagrams, we assume the unit area of the facet $S = 1\text{m}^2$, the uniform unit radiance $L = 1\,\text{W/sr/m}^2$ as observed from the origin of the coordinate system. Under such conditions, the radiant flux received by the facet in xy plane is 2π.

Glass. We assume the refractive index 1.5 for glass. The graphs for reflected and refracted light are shown in Fig. 9.5 and 9.6.

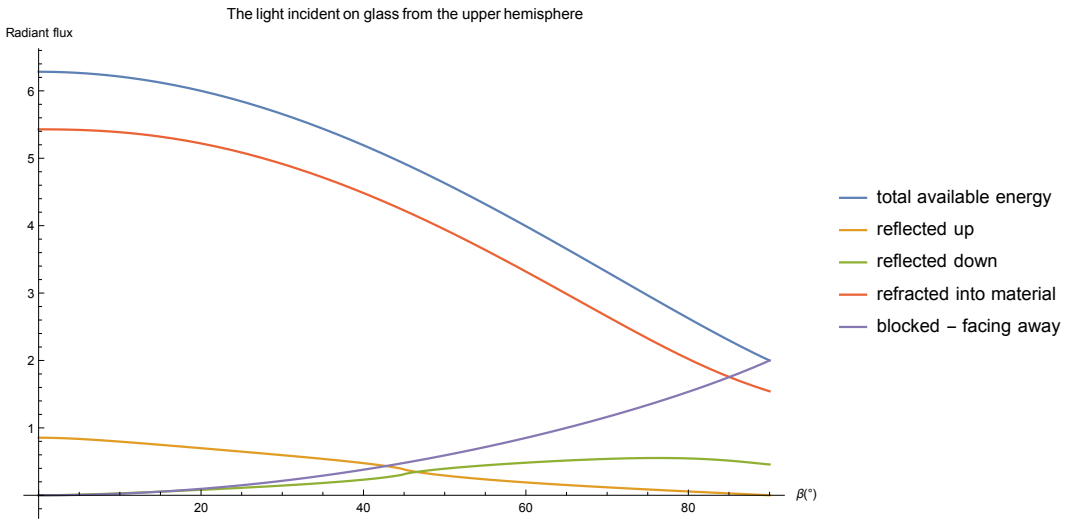

Figure 9.5: The light incident on the glass ($\eta_2 = 1.5$) facet from air. The source of light is uniformly shining hemisphere ($z > 0$) in the infinity, the facet has unit area and its angle to the xy plane is β. The figure shows the amount of light (radiant flux), which is incident on the facet, reflected up, reflected down, refracted into the material, and the light which does not illuminate the facet.

Diamond. For the diamond, we assume the refractive index 2.419. The graphs for reflected and refracted light are shown in Fig. 9.7 and 9.8.

9.4.2 The radiant flux on actual stone cuts

Let us have a stone cut called square and brilliant cut, see Fig. 9.9. The square used has upper and lower facet angle 96°, the side of the table is 0.46 of the stone side. The example of the brilliant on the dimensions are shown on the Fig. 9.10

One cannot judge the stone just by the parameters in Tab. 9.1. There are other important characteristics which are not reflected here, e.g. a stone fire, number of exiting beams etc.

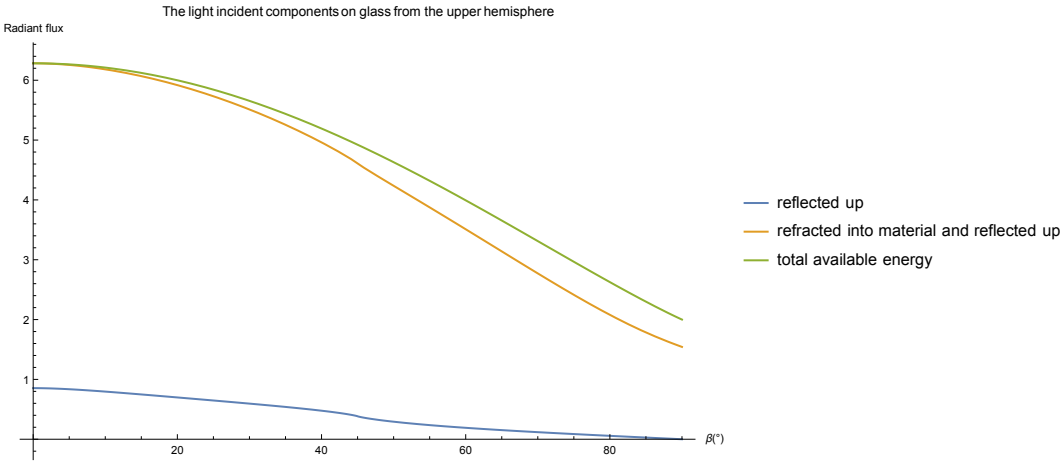

Figure 9.6: The light incident on the glass ($\eta_2 = 1.5$) facet from air. The source of light is uniformly shining hemisphere ($z > 0$) in the infinity, the facet has the unit area and its angle to the xy plane is β. The figure shows the radiant fluxes, which are total incident light, reflected up and refracted into the material, and reflected up only.

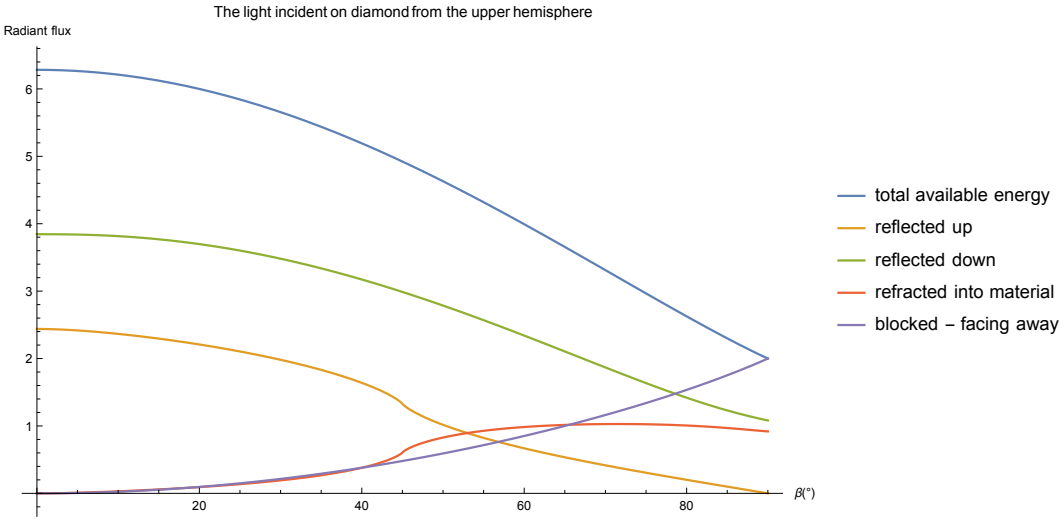

Figure 9.7: The light incident on the diamond ($\eta_2 = 2.419$) facet from air. The source of light is an uniformly shining hemisphere ($z > 0$) in the infinity, the facet has unit area and its angle to the xy plane is β. The figure shows the amount of light (radiant flux), which is incident on the facet, reflected up, reflected down, refracted into the material, and the light which does not illuminate the facet.

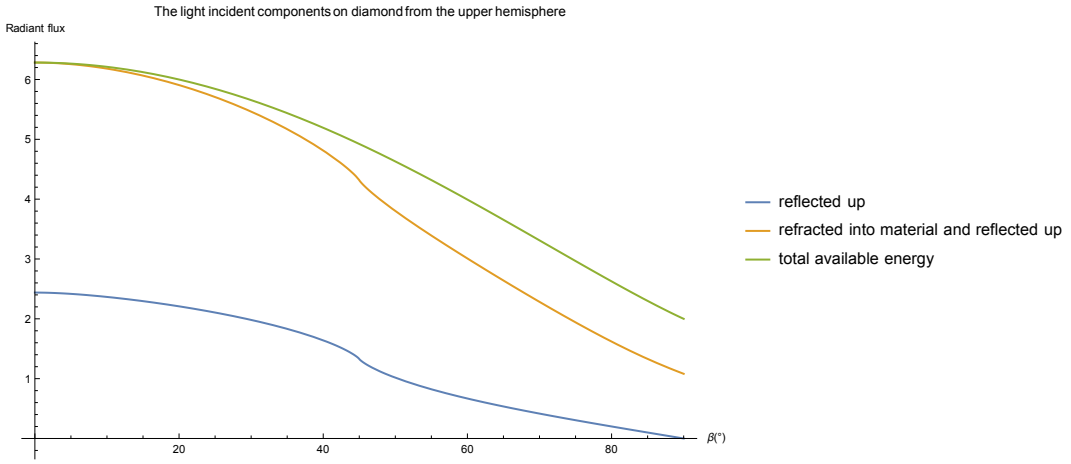

Figure 9.8: The light incident on the diamond ($\eta_2 = 2.419$) facet from air. The source of light is an uniformly shining hemisphere ($z > 0$) in the infinity, the facet has unit area and its angle to the xy plane is β. The figure shows the radiant fluxes of the all incident light, reflected up and refracted into the material, and reflected up only.

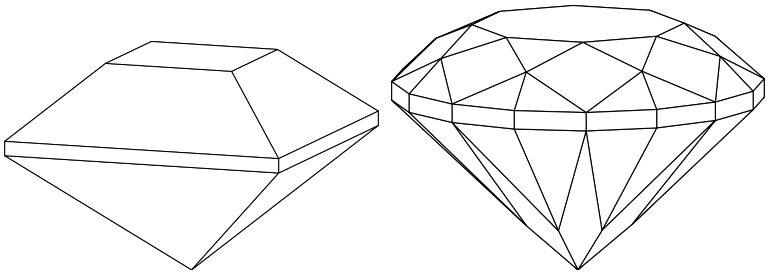

Figure 9.9: The stone cut called a square and a brilliant cut. The square is made of table, four upper facets and four lower facets. Girdle, connecting the upper and lower part, need not be always present. The brilliant cut is shown on right.

Stone shape		Flat square	Flat circle	Square	Brilliant
Total available light	Φ_{on}	3.14	4.93	2.78	4.98
Reflected up	Φ_{up}	0.43	0.67	0.28	0.55
Reflected down	Φ_{down}	0	0	0.11	0.12
Refracted in	Φ_{in}	2.71	4.26	2.40	4.32

Table 9.1: The radiant fluxes for square cut and brilliant cut made from glass. The first two columns are just rectangle and circle in the xy plane. They are presented for comparison. All shapes are normalized to have the same circumscribed sphere with the diameter 1 to simulate the situation the stone is cut from raw material of about same size. The square has lower area, so its radiant fluxes are generally lower.

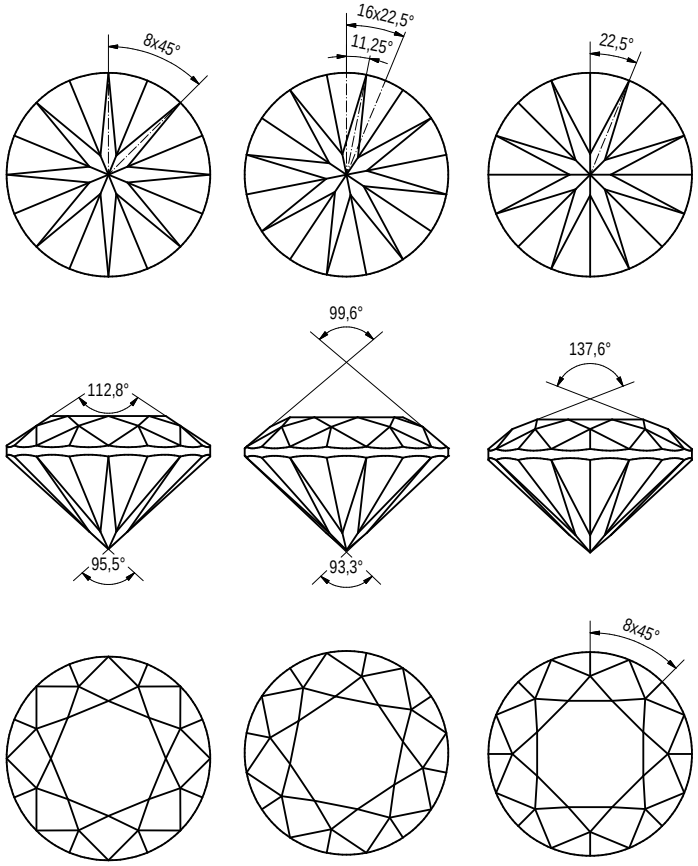

Figure 9.10: Dimensions of the brilliant cut stone. The dimensions slightly differ depending on the manufacturer, material, or product type.

9.5 Applications

This part of the contribution overcomes the major problem of returned light energy evaluation, which is sampling the incident light either as rays or as beams.

One can object that the ray/beam sampling problem has a similar nature to the problem of numerical integration, which is used to evaluate some of the integrals. On the other hand, the numerical integration is much more studied problem as it has many applications in various fields of mathematics, physics, and engineering. So one can expect that methods of numerical integration have a higher quality than ray-tracing method in general.

The proposed method offers the possibility to weigh the incident light or emitted light by a functions preferring some directions for example in the z direction and suppressing other e.g. close to xy plane. One can formulate computation of criteria like light return [93], DCLR [152] using this approach.

However, this method fills just the first step in the light modeling. To compute the split and refraction of divergent beams is more difficult compared to our previous

method [145]. Although the integrals involved in the first step are numerically solvable, the situation becomes more complicated when more reflections occur. There is clearly a space for further research. The relevant mathematics can be found in [146].

The results achieved can still be used for indication of the light returned by the stone although not calculating it completely. This information can be used for stone assessment or stone cut design.

Chapter 10

Conclusions

This thesis makes a scientific contribution to the modeling of light propagation in jewelry cut stones and its use for image-based quality assurance in the industrial context. Research summarized in the thesis was motivated by practical needs from the bijouterie industry. The thesis also benefits from extensive experience in building machines for quality assurance of jewelry cut stones.

There are several interesting tasks related to cut stones. Their shapes have to be designed according to user requirements. Cut stones have to be evaluated in the production to answer whether the product specifications are met. The already manufactured stones have to be valued and their quality has to be assessed. The image-based assessment of the cut stone also provides a feedback to improve the production itself.

In our previous work, we proposed the beam-tracing model [145, 82], that enables the simulation the propagation of collimated light beams in transparent polyhedral stones.

The contribution of this thesis to the beam-tracing model is threefold:

First, we show that the propagation of collimated light beams in polyhedral stones can be represented by a graph, see Chapter 6. The graph representation includes node and edge attributes describing radiometric and geometric properties of the propagated beams.

Second, the radiometric part of the model was extended to absorbing stone materials. The method is based on Beer's law of exponential attenuation of the light [76]. The developed method enables evaluating the radiant flux of a collimated beam reflected or refracted multiple times within a polyhedral object. The input to the procedure is the irradiance or Stokes vector of irradiances of the beam at the entrance to the absorbing media, the refraction index and the attenuation coefficient of the stone material, and geometry of the experiment. See Chapter 7. Color stones make a significant fraction of the cut stones manufactured. Incorporating absorption into the model allows to simulate the propagation in color stones.

Third, the thesis focuses on a more general geometrical model of stones. Real stones always have, for various reasons, round edges. Although from the radiometric point of view, the contribution of round edges is usually negligible and the reflections and refractions on the edges produce observable artifacts in images seen in real

experiments. The stones illuminated by collimated beams of light not only produce expected concentrated spots (traces) on the screen, but also protrusions from each spot. We provide the explanation and mathematical description of these traces in Chapter 8.

Also presented is a mathematical model of stone with rounded edges. The geometry of the rays emanating from the edge illuminated by a collimated beam is studied. The rays emanating from realistic edges lie on a conic surface with the cone axis in the edge. As the curvature of the edge is not constant, in most cases, the only visible part of ray traces on the screen, surrounding the stone, is close to the light traces for beams with sharp edges. Some light rays are reflected on the edges to the stone interior. Subsequently, light rays are reflected in the stone multiple times. The analysis shows that part of such rays passes through the same facets as the beam illuminating the edge. This subset of rays produces an observable protrusion trace on the screen.

The mathematical model explains the experimental data. We illuminate the stone by the a collimated beam in the physical experiment. The beams emanating from the stone fall onto the screen whose image is captured by a camera. Besides theoretical understanding of the appearance of screen images from such experiments, the main contribution of this observation is its use in the inverse problem [83]. The inverse problem aims at reconstructing the stone proportions based on observing the collimated beams emanating from the stone after its illumination by a collimated beam. Until now the main obstacle in solving the inverse problem was the correspondence problem. One has to correspond the physically observed trace matches to the simulated beams in the computer model. The protrusions and their orientations are visible in the screen photos and also can be simulated in the extension of the original LADOK program package [145].

The novel approach presented in Chapter 9 avoids ray-tracing [152] and beam-tracing [145] altogether. The stone design maximizes a mixture of characteristics, many of them radiometric. Both ray-tracing and beam-tracing can, up to some degree, calculate radiometric characteristics like light return [93], DCLR [152]. The tracing methods are time consuming and can be inaccurate due to problems with sampling the ray or beam space. Our approach suggests to use methods motivated by integral calculus where radiant flux is calculated by integrals. The thesis presents a solution for the first optical interface only, but the methodology can be used for multiple interfaces as well.

Appendix A

Author's Publications

Publications related to the thesis

Patents

1. Smutný, V. and I. Bodlák (2007). "System and Method of Measurement of the Shape of Transparent object, Particularly Cut Stones". CZ298071 (Prague, Czech Republic). C. T. U. in Prague
. http://worldwide.espacenet.com/publicationDetails/biblio?FT=D&CC=CZ&NR=298071B6.

Other publications

Impacted journals articles

2. Dostálová, T., E. Tauferová, Z. Teuberová, M. Seydlová, V. Smutný, J. Racek, and M. Bartoňová (2006). Shape and Size of Dental Arch, A Five-year Prospective Study. *Methods of Information in Medicine* **45**(2), 191–194. ISSN: 0026-1270.
3. Dostálová, T., J. Racek, E. Tauferová, and V. Smutný (2004). Average Arch Widths and Associated Changes between Initial, Post-treatment and Post-retention Measurements. *Brazilian Dental Journal* **15**(3), 204–208. ISSN: 0103-6440.
4. Soldánová, M., O. Lešetický, L. Komárková, T. Dostálová, V. Smutný, and M. Špidlen (2012). Effectiveness of Treatment of Adult Patients with the Straightwire Technique and the Lingual Two-Dimensional Appliance. *European Journal of Orthodontics* **34**(6), 674–680. ISSN: 0141-5387.

Peer-reviewed journals articles

5. Dostálová, T., V. Smutný, and R. deKanter (1998). Obrazová informace ve stomatologii jako základ zdravotní dokumentace. In Czech. *Praktické zubní lékařství* **46**(5). In Czech, 149–54. ISSN: 0032-6720.

6. Hippmann, R., T. Dostálová, M. Bartoňová, M. Peterka, K. Morong, and V. Smutný (2005). Počítačová kontrola tvaru zubního oblouku u pacientů s rozštěpem. In Czech. *Praktické zubní lékařství* **53**(5), 100–107. ISSN: 0032-6720.
7. Smutný, V., T. Pajdla, V. Hlaváč, and P. Palatka (1999). Měření a inspekce s pomocí digitálního profilprojektoru. In Czech. *Jemná mechanika a optika* **44**(3). Ed. by J. Nevřala, 72–73. ISSN: 0447-6441.

Other journals articles

8. Hlaváč, V., K. Hanton, P. Křízek, V. Smutný, J. Bernát, and D. Hanuschová (2003). Několik inovací pro inspekci kanalizačního potrubí televizními inspekčními systémy. In Czech. *SOVAK, časopis oboru vodovodů a kanalizací* **12**(6), 11–13. ISSN: 1210-3039.
9. Lejčková, K., M. Polívka, J. Rataj, V. Smutný, and J. Volf (2001). Prezentace ČVUT na 43. ročníku mezinárodního strojírenského veletrhu a 1.ročníku mezinárodního veletrhu dopravy a logistiky Transport a Logistika v Brně ve dnech 24.-28. září 2001. Czech. *Pražská technika* **2001**(5), 16–18. ISSN: 1213-5348.
10. Pajdla, T., P. Palatka, and V. Smutný (2003). Rozpoznávání Brailleova písma. Czech. *Softvarové noviny* **XIV**(6), 91–91. ISSN: 1210-8472.
11. Smutný, V., R. Šára, P. Krsek, and V. Zýka (2002). Trojrozměrné měření reliéfu dlaždic. Czech. *Automa* **8**(8-9), 28–29. ISSN: 1210-9592.

Patents

12. Farkavec, P. and V. Smutný (2012). "Robot for cleaning and inspection of conduits and its control unit". WO Patent App. PCT/CZ2010/000,080. `https://www.google.com/patents/WO2011009420A3?cl=en`.
13. Farkavec, P. and V. Smutný (2012). "Robot for cleaning and inspection of conduits and its control unit". US Patent App. 13/386,868. `https://www.google.com/patents/US20120197440`.
14. Farkavec, P. and V. Smutný (2012). "Robot for cleaning and inspection of conduits and its control unit". EP Patent App. EP20,100,765,934. `https://www.google.com/patents/EP2456578A2?cl=en`.
15. Smutný, V. and P. Farkavec (2010). "Robot pro čištění a inspekci potrubí a ovládací jednotka pro jeho řízení". CZ302170. `http://isdv.upv.cz/portal/pls/portal/portlets.pts.det?xprim=1413277`.
16. Smutný, V. and R. Šára (2005). "Method and a system for measuring joint trajectory, particularly mandibular joint trajectory". CZ296088. `http://isdv.upv.cz/portal/pls/portal/portlets.pts.det?xprim=277990`.

Publications excerpted by WOS

17. Dostálová, T., V. Hlaváč, T. Pajdla, R. Šára, and V. Smutný (1994). Three computer vision applications in dentistry. In: *Physiology and Function from Multidimensional Images*. (Newport Beach, California). Ed. by R. S. A. Eric A. Hoffman.

SPIE Proceedings Series 2168. SPIE - The International Society for Optical Engineering. Bellingham, Washington: SPIE - The International Society for Optical Engineering, pp.416–424. ISBN: 0-8194-1463-8.

18. Dostalova, T. and V. Smutny (1997). Orthoscope - Digital images in dentistry and dermatology. English. In: *ITAB '97 - Information Technology Applications in Biomedicine*. Ed. by Eck, V and Krekule, I. Prague, Czech Republic. New York, USA: IEEE, pp.88–89. ISBN: 0-7803-4318-2.
19. Dostálová, T. and V. Smutný (1997). Dental Archives Based on Images. In: *Medical Imaging 97*. Ed. by S. Horii and G. J. Blaine. Vol. 3035. Newport Beach, California: SPIE, pp.301–308.
20. Hanton, K., V. Smutný, V. Franc, and V. Hlaváč (2003). Alignment Of Sewerage Inspection Videos for Their Easier Indexing. In: *ICVS2003 : Proceedings of the Third International Confernece on Vision Systems*. (Graz, Austria). Ed. by J. Crawley, J. Piater, M. Vincze, and L. Paletta. Vol. 2626. Lecture Notes in Computer Science. Berlin, Germany: Springer-Verlag, pp.141–150. ISBN: 3-540-00921-3.
21. Hlaváč, V. and V. Smutný (1992). Robust Curve Approximation for 3-D Model-Based Vision. In: *Image Processing and Its Application*. London, UK: IEE, pp.429–432.
22. Šára, R., V. Smutný, M. Veverková, and J. Čumpelík (2002). A Photogrammetric Method for Measuring Breathing Movements. In: *Analysis of Biomedical Signals and Images, Proceedings of 16th Biennial International EURASIP Conference BIOSIGNAL 2002*. (Brno, Czech Republic). Ed. by J. Jan, J. Kozumplík, and I. Provazník. Brno University of Technology, Brno, Czech Republic: VUTIUM Press, pp.329–331. ISBN: 80-214-2120-7.
23. Smutný, V., V. Hlaváč, and T. Pajdla (1998). Vision-based Sensors for Production Control — The Experience Gathered in Applications. In: *Intelligent Systems for Manufacturing*. (Prague, Czech Republic). Ed. by L. M. Camarinha-Matos, H. Afsarmanesh, and V. Marik. IFIP. Boston, USA: Kluwer Academic Publisher, pp.525–32. ISBN: 0-412-84670-5.
24. Smutný, V., V. Hlaváč, and P. Palatka (1998). High Precision Measurements of Small Backlit Objects in Mechanical Engineering. In: *IECON'98 : Proceedings of the 24th Annual Conference of the IEEE Industrial Electronics Society*. (Aachen, Germany). Ed. by P. Drews. Vol. 2. IEEE Industrial Electronics Society. Piscataway, USA: Institute of Electrical and Electronics Engineers, pp.1226–1229. ISBN: 0-7803-4503-7.
25. Smutný, V., J. Čech, R. Šára, and T. Dostálová (2002). Estimation of the Temporomandibular Joint Trajectory by Photogrammetry. In: *Analysis of Biomedical Signals and Images, Proceedings of 16th Biennial International EURASIP Conference BIOSIGNAL 2002*. (Brno, Czech Republic). Ed. by J. Jan, J. Kozumplík, and I. Provazník. Brno University of Technology, Brno, Czech Republic: VUTIUM Press, pp.271–273. ISBN: 80-214-2120-7.

Conference papers

26. Dostálová, T., V. Hlaváč, T. Pajdla, R. Šára, and V. Smutný (1994). Computer Vision Aplications in Dentistry. In: *Biomedical Engineering and Biotechnology*. Praha, Czech Republic: Czech Technical University, pp.11–12.
27. Dostálová, T., V. Hlaváč, T. Pajdla, R. Šára, and V. Smutný (1994). Three Computer Vision Applications in Dentistry. In: *Physiology and Function from Multidimensional Images*. Ed. by E. A. Hoffman and R. S. Acharya. Vol. 2168 of SPIE proceedings series. Newport Beach, California, pp.416–424.
28. Dostálová, T., J. Racek, E. Tauferová, and V. Smutný (2004). Shape and Size of Dental Arch, a 5 Years Prospective Study. In: *Abstract book of 28th Annual Conference of the European Prosthodontic Association*. (Izmir, Turkey). Vol. 28. London, United Kingdom: European Prosthodontic Association, pp.77–78.
29. Dostálová, T., M. Rousalová, V. Smutný, and R. deKanter (1998). Diastemic Closure – a case report. In: *Novel biomaterials in prosthodontics and implantology and clinically relevant aspects on occlusion*. (Turku, Finland). Berlin, Germany: European Prosthodontic Association, pp.74.
30. Dostálová, T. and V. Smutný (1997). Diagnostic Control the Shape and Size of Dental Arch during Prosthetic Rehabilitation of Patients. In: *The Proceedings of the European Prosthodontic Association*. (Copenhagen, Denmark). Berlin, Germany: European Prosthodontic Association, pp.50–51.
31. Hlaváč, V., T. Dostálová, V. Smutný, and R. Šára (1994). 3D Surface Reconstruction and its Application in Dentistry. In: *Proceedings of the Czech Technical University Workshop*. Prague, Czech Republic: CTU Publishing House, pp.101–102.
32. Hlaváč, V., R. Mařík, M. Meloun, T. Pajdla, R. Šára, and V. Smutný (1992). Model-based Computer Vision. In: *IBM Academic Initiative Projects Seminar*, pp.67–74.
33. Hlaváč, V. and V. Smutný (1992). Curve Approximation Using Conic Segments. In: *Pattern Recognition 1992*. Ed. by W. G. K. H. Bischof. Wien, Austria: R. Oldenbourg, pp.161–170.
34. Hlaváč, V. and V. Smutný (1992). Robust Curve Approximation for 3-D Model-Based Vision. In: *Image Processing and Its Application*. London, UK: IEE, pp.429–432.
35. Hlaváč, V., V. Smutný, and R. Šára (1995). Medicínské aktivity Laboratoře počítačového vidění. In Czech. In: *Sborník pracovního setkání: "Výuka a výzkum v oblasti biomedicínského inženýrství a biotechnologii na FEL ČVUT v Praze"*. (Prague, Czech Republic). Vol. 2. Czech Technical University. Prague, Czech Republic: Czech Technical University, pp.73.
36. Hlaváč, V., R. Mařík, M. Meloun, V. Smutný, and R. Šára (1993). New Image Analysis Algorithms. In: *Proc. Workshop CTU Prague*. (Prague, Czech Republic). Vol. A. Czech Technical University in Prague. Prague, Czech Republic: Czech Technical University in Prague, pp.67–68.
37. Král, L., J. Čapek, V. Smutný, and V. Hlaváč (1995). Autonomous Mobile Platform. In: *Proceedings of the Czech Technical University and TU Brno Workshop*. Prague, Czech Republic: CTU Publishing House, pp.141–142.

38. Král, L., B. Sládek, V. Smutný, and V. Hlaváč (1995). Autonomous vehicle motion control. In: *Proceedings of the 3rd Symposium on Intelligent Robotics Systems'95*. Ed. by C. Colombo and J. Crowley. Pisa, Italy, pp.83–90.
39. Kraus, S., J. Fisher, and V. Smutný (1995). Enhancing Radiometric Possibilities of the CCD Camera. In: *Workshop 95, Part I.* Prague, Czech Republic: CTU Prague and TU Brno, pp.177–178.
40. Kukelova, Z., P. Krsek, V. Smutny, and T. Pajdla (2013). Groebner basis solutions to satellite trajectory control by pole placement. In: *Proceedings of the Advanced Maui Optical and Space Surveillance Technologies Conference*. (Maui, USA). on-line proceedings. Kihei, US: Maui Economic Development Board, pp.748–757.
41. Pajdla, T., V. Smutný, V. Hlaváč, and P. Palatka (1999). Contour Segmentation for Precise Measurement in Back-light Illumination. In: *Robust Vision for Industrial Applications, 23-rd ÖAGM-Workshop*. (Steyr, Austria). Vienna, Austria: Austrian Association for Pattern Recognition, pp.147–154.
42. Palatka, P. and V. Smutný (2002). Kamerové systémy pro přesné měření a kontrolu kvality v průmyslu. In Czech. In: *Pragoregula - Elexpo 2002*. (Prague, Czech Republic). Ed. by B. Šulc. Praha, Czech Republic: Masarykova akademie práce, pp.65–70. ISBN: 80-902131-8-9.
43. Dostálová, T., V. Hlaváč, R. Šára, and V. Smutný (1994). Capturing and Visualization of the Tooth Occlusion. In: *Proc. Conf. Biosignal'94*. (Brno, Czech Republic). Ed. by J. Rozman. Brno, Czech Republic: Electrical Engineering Society, FEECS Division, Technical University Brno, pp.175–177. ISBN: 80-02-00999-1.
44. Hlaváč, V., R. Šára, V. Smutný, and T. Dostálová (1994). Computer Vision Applications in Dentistry – is it Robotics? In: *Proc. Int. Symposium Intelligent Robotic Systems '94*. (Grenoble, France). Ed. by A. Borkowski and J. L. Crowley. Grenoble, France: LIFIA-IMAG, pp.246–254.
45. Smutný, V., V. Hlaváč, and P. Palatka (1999). High Precision Dimensions and Shape Measurements of Small Objects. In: *Proceedings of the First International Conference on Advanced Engineering Design*. (Prague, Czech Republic). Ed. by P. Fiala and S. cek Ladislav. Prague, Czech Republic: CTU Publishing House, pp.116. ISBN: 80-01-02055-X.
46. Smutný, V., V. Hlaváč, and P. Palatka (1998). High Precision Measurements of Small Backlit Objects in Mechanical Engineering. In: *IECON'98 : Proceedings of the 24th Annual Conference of the IEEE Industrial Electronics Society*. (Aachen, Germany). Ed. by P. Drews. Vol. 2. IEEE Industrial Electronics Society. Piscataway, USA: Institute of Electrical and Electronics Engineers, pp.1226–1229. ISBN: 0-7803-4503-7.
47. Smutný, V. (1995). Optimization of color filter for rainbow range finder. In: *CTU Workshop 95*. CTU. Prague, Czech Republic: CTU Publishing House, pp.173–174.
48. Smutný, V. (1993). Analysis of Rainbow Range Finder Errors. In: *1st Czech Pattern Recognition Workshop*. Ed. by V. Hlaváč and T. Pajdla. Temešvár u Písku, Czech Republic: Czech Pattern Recognition Society, pp.59–66.
49. Smutný, V. (1997). Industrial Applications of Computer Vision. In: *Czech Pattern Recognition Workshop '97*. Ed. by T. Pajdla. Prague, Czech Republic: Czech Pattern Recognition Society, pp.131–138.

50. Smutný, V., J. Čech, R. Šára, and T. Dostálová (2002). Estimation of the Temporomandibular Joint Position. In: *Proceedings of the CVWW'02*. (Bad Aussee, Austria). Ed. by H. Wildenauer and W. Kropatsch. Wien, Austria: Pattern Recognition & Image Processing Group, Vienna University of Technology, pp.306–314.
51. Smutný, V., T. Dostálová, J. Dušková, and V. Hlaváč (1993). Evaluation of Plaque Formation - Surface Reflectance Measurement. In: *Computer Analysis of Images and Patterns 93*. Ed. by W. G. K. D. Chetverikov. Springer Verlag, pp.679–686.
52. Smutný, V., M. Friedl, P. Tax, and P. Píša (1996). Counting of Healds and Dents by Optical Method. In: *CTU Workshop 96*. CTU. Prague, Czech Republic: CTU Publishing House, pp.177–178.
53. Smutný, V. and J. Klaus (1997). Software for P1394 Digital Camera. In: *CTU Workshop 97*. CTU. Prague, Czech Republic: CTU Publishing House, pp.183–184.
54. Smutný, V., P. Prášek, P. Palatka, and T. Pajdla (2007). 3-D Reconstruction of Langweil's Model of Prague: Data Acquisition. In: *EVA 2007 Berlin: Electronische Bildverarbeitung und Kunst, Kultur, Historie*. (Berlin, Germany). Ed. by A. Bienert, G. Stanke, J. Hemsley, and V. Cappellini. EVA Conferences International. Rudower Chaussee 30, 12489, Berlin, Germany: Gesellschaft zur Förderung angewandter Informatik e. V., pp.101–107. ISBN: 3-9809212-8-X.
55. Smutný, V., P. Palatka, and V. Hlaváč (1998). Computer Vision in Industry, Practice in the Czech Republic. In: *Proceedings of the Scientific Conference Artificial Intelligence in Industry 1998*. (High Tatras, Slovakia). Ed. by J. Sarnovský, P. Sinčák, M. Mach, and M. Hatala. Košice, Slovakia: Technical University of Košice, pp.329–38. ISBN: 80-88786-83-5.
56. Vydržel, J., V. Smutný, T. Pajdla, and V. Hlaváč (1997). Improvement of Rainbow Range Finder Calibration. In: *Proceedings of the Czech Pattern Recognition Workshop '97*. (Milovy, Czech Republic). Prague, Czech Republic: Czech Pattern Recognition Society, pp.77–81.
57. Vydržel, J., V. Smutný, T. Pajdla, and V. Hlaváč (1997). Rainbow Range Finder Calibration. In: *9. Aachener kolloquium "Signaltheorie" Bild- und Sprachsignale*. Aachen, Germany: RWTH Aachen, Lehrstühle der Fakultät für Elektrotechnik.
58. Werner, T., R. D. Hersch, V. Hlaváč, and V. Smutný (1995). Rendering Real World Objects Without 3-D Model. In: *Proceedings of the Czech Technical University and TU Brno Workshop*. Prague, Czech Republic: CTU Publishing House, pp.179–180.

Edited conferences

59. Clabian, M., V. Smutný, and G. Stanke, eds. (2004). *Applications of Computer Vision '04*. (Czech Technical University, Prague, Czech Republic). Prague, Czech Republic: Czech Technical University, Faculty of Electrical Engineering, p. 130. ISBN: 80-01-02977-8.
60. Clabian, M., V. Smutný, and G. Stanke, eds. (2006). *Applications of Computer Vision '06*. (Graz, Austria). Prague, Czech Republic: Czech Technical University, Faculty of Electrical Engineering, p. 154. ISBN: 80-01-03477-1.

Citations of author's work

61. Batlle, J., E. Mouaddib, and J. Salvi (1998). Recent progress in coded structured light as a technique to solve the correspondence problem: A survey. English. *PATTERN RECOGNITION* **31**(7), 963–982. ISSN: 0031-3203.
62. Caspi, D., N. Kiryati, and J. Shamir (1998). Range imaging with adaptive color structured light. *Pattern Analysis and Machine Intelligence, IEEE Transactions on* **20**(5), 470–480. ISSN: 0162-8828.
63. Dalessandri, D., E. Lazzaroni, M. Migliorati, M. G. Piancino, I. Tonni, and S. Bonetti (2013). Self-ligating fully customized lingual appliance and chair-time reduction: a typodont study followed by a randomized clinical trial. English. *EUROPEAN JOURNAL OF ORTHODONTICS* **35**(6), 758–765. ISSN: 0141-5387.
64. Dostalova, T., M. Kasparova, M. Seydlova, P. Kriz, and H. Patockova (2010). Orthodontic patient - Growth of somatic structures including implants insertion - 3D longitudinal reconstruction. In: *Proceedings of the IEEE/EMBS Region 8 International Conference on Information Technology Applications in Biomedicine, ITAB.*
65. Gkantidis, N. and M. Sanoudos (2013). Lower Anterior Crowding Correction by a Convenient Lingual Method. English. *JOURNAL OF ESTHETIC AND RESTORATIVE DENTISTRY* **25**(2), 96–100. ISSN: 1496-4155.
66. Horn, E. and N. Kiryati (1999). Toward optimal structured light patterns. *Image and Vision Computing* **17**(2), 87–97. ISSN: 0262-8856.
67. Kasparova, M., A. Prochazka, L. Grajciarova, M. Yadollahi, O. Vysata, and T. Dostalova (2014). Evaluation of dental morphometrics during the orthodontic treatment. *BIOMEDICAL ENGINEERING ONLINE* **13**. ISSN: 1475-925X.
68. Long, H., Y. Zhou, U. Pyakurel, L. Liao, F. Jian, J. Xue, N. Ye, X. Yang, Y. Wang, and W. Lai (2013). Comparison of adverse effects between lingual and labial orthodontic treatment A systematic review. English. *ANGLE ORTHODONTIST* **83**(6), 1066–1073. ISSN: 0003-3219.
69. Marson, F. C., L. G. Sensi, L. C. C. Vieira, and E. Araujo (2008). Clinical evaluation of in-office dental bleaching treatments with and without the use of light-activation sources. *Operative dentistry* **33**(1), 15–22.
70. Rosseto, M. C., F. M. C. Palma, R. I. Ferreira, A. Pinzan, and F. Vellini-Ferreira (2009). Comparative study of dental arch width in plaster models, photocopies and digitized images. *Brazilian Oral Research* **23**(2), 190–195.

Bibliography

71. Abramowitz, M. and I. Stegun (1964). *Handbook of Mathematical Functions: With Formulas, Graphs, and Mathematical Tables*. Applied mathematics series. Dover Publications. ISBN: 9780486612720
. http://books.google.de/books?id=MtU8uP7XMvoC.
72. Agarwal, S., S. P. Mallick, D. Kriegman, and S. Belongie (2004). On refractive optical flow. In: *Proc. ECCV04*, pp.483–494.
73. Alt, N., P. Rives, and E. Steinbach (2013). Reconstruction of transparent objects in unstructured scenes with a depth camera. In: *Image Processing (ICIP), 2013 20th IEEE International Conference on*, pp.4131–4135.
74. Ament, M., C. Bergmann, and D. Weiskopf (2014). Refractive Radiative Transfer Equation. *ACM Trans. Graph.* **33**(2), 17:1–17:22. ISSN: 0730-0301.
75. Atcheson, B., I. Ihrke, D. Bradley, W. Heidrich, M. Magnor, and H.-P. Seidel (2007). Imaging and 3D tomographic reconstruction of time-varying, inhomogeneous refractive index fields. In: *SIGGRAPH '07: ACM SIGGRAPH 2007 sketches*. San Diego, California: ACM, pp.32.
76. Bass, M., E. W. Van Stryland, D. R. Williams, and W. L. Wolfe, eds. (1995). *Handbook of Optics*. 2-nd. Vol. 1: Fundamentals, Techniques and Design. McGraw-Hill Inc. ISBN: 0-07-047740-X.
77. Ben-Ezra, M. and S. Nayar (2003). What does motion reveal about transparency? In: *Proceedings. Ninth IEEE International Conference on Computer Vision, 2003.* Vol. 2, pp.1025–1032.
78. Blais, F. (2004). Review of 20 years of range sensor development. *Journal of Electronic Imaging* **13**(1), 231–243.
79. Blodgett, T., R. Geurts, A. Gilbertson, B. Green, T. Hemphill, and T. Moses (2009). "System and method for gemstone cut grading". US Patent 7,571,060. http://www.google.com.br/patents/US7571060.
80. Blodgett, T., R. Geurts, A. Gilbertson, B. Green, T. Hemphill, and T. Moses (2012). "System and method for gemstone cut grading". US Patent 8,239,143. https://www.google.com/patents/US8239143.
81. Blodgett, T., R. Geurts, A. Gilbertson, B. Green, T. Hemphill, and T. Moses (2012). "System and method for gemstone cut grading". US Patent 8,095,325. https://www.google.com/patents/US8095325.
82. Bodlák, I. (2004). *Rozšíření toolboxu LADOK*. Supervisor: Vladimír Smutný, In Czech. Prague, Czech Republic: Faculty of Electrical Engineering, Czech Technical University in Prague.

83. Bodlák, I. (2005). “Modelování a analýza broušeného kamene”. Supervisor: Vladimír Smutný, In Czech. Master thesis. Prague, Czech Republic: Czech Technical University in Prague.
84. Bonfort, T., P. Sturm, and P. Gargallo (2006). “General Specular Surface Triangulation”. In: *Computer Vision - ACCV 2006*. Ed. by P. Narayanan, S. Nayar, and H.-Y. Shum. Vol. 3852. Lecture Notes in Computer Science. Springer Berlin / Heidelberg, pp.872–881. http://dx.doi.org/10.1007/11612704%5C_87.
85. Born, M. and E. Wolf (1980). *Principles of Optics. Electromagnetic Theory of Propagation, Interference and Diffraction of Light*. 6-th. Cambridge University Press. ISBN: 0-521-63921-1.
86. Csebfalvi, B. (1997). *A Review of Monte Carlo Ray Tracing Methods*. http://www.cescg.org/CESCG97/csebfalvi/.
87. Davis, J., D. Nehab, R. Ramamoorthi, and S. Rusinkiewicz (2005). Spacetime stereo: a unifying framework for depth from triangulation. *IEEE Transactions on Pattern Analysis and Machine Intelligence,* **27**(2), 296–302. ISSN: 0162-8828.
88. Davis, P. J. and P. Rabinowitz (2007). *Methods of numerical integration*. Courier Dover Publications.
89. Donoho, D. (2006). Compressed sensing. *IEEE Transactions on Information Theory* **52**(4), 1289–1306. ISSN: 0018-9448.
90. Eren, G., O. Aubreton, F. Meriaudeau, L. Sanchez Secades, D. Fofi, A. Naskali, F. Truchetet, and A. Ercil (2009). “A 3D Scanner for Transparent Glass”. In: *Image Analysis and Processing - ICIAP 2009*. Ed. by P. Foggia, C. Sansone, and M. Vento. Vol. 5716. Lecture Notes in Computer Science. Springer Berlin / Heidelberg, pp.519–527. http://dx.doi.org/10.1007/978-3-642-04146-4%5C_56.
91. Eren, G., O. Aubreton, F. Meriaudeau, L. S. Secades, D. Fofi, A. T. Naskali, F. Truchetet, and A. Ercil (2009). Scanning from heating: 3D shape estimation of transparent objects from local surface heating. *Opt. Express* **17**(14), 11457–11468.
92. Ferraton, M., C. Stolz, and F. Meriaudeau (2008). Surface Reconstruction of Transparent Objects by Polarization Imaging. In: *SITIS ’08. IEEE International Conference on Signal Image Technology and Internet Based Systems, 2008*, pp.474–479.
93. Froehlich, M., K. Eder, and G. Blasbichler (2012). “Gemstone with a chaton cut”. Pat. Nr. US20120227444. http://www.google.com/patents/US20120227444.
94. Goldstein, D. and D. Goldstein (2003). *Polarized Light, Revised and Expanded*. Optical engineering. Taylor & Francis. ISBN: 9780203911587. http://books.google.cz/books?id=aWX5jj603PoC.
95. Gross, J. L. and J. Yellen (2004). *Handbook of Graph Theory*. CRC Press. ISBN: 1-58488-090-2.
96. Gu, J., S. Nayar, E. Grinspun, P. Belhumeur, and R. Ramamoorthi (2008). “Compressive Structured Light for Recovering Inhomogeneous Participating Media”. In: *Computer Vision - ECCV 2008*. Ed. by D. Forsyth, P. Torr, and A. Zisserman. Vol. 5305. Lecture Notes in Computer Science. Springer Berlin / Heidelberg, pp.845–858. http://dx.doi.org/10.1007/978-3-540-88693-8%5C_62.
97. Hasinoff, S. and K. Kutulakos (2008). “Light-Efficient Photography”. In: *Computer Vision - ECCV 2008*. Ed. by D. Forsyth, P. Torr, and A. Zisserman. Vol. 5305. Lecture Notes in Computer Science. Springer Berlin / Heidelberg, pp.45–59. http://dx.doi.org/10.1007/978-3-540-88693-8%5C_4.

98. Hasinoff, S. and K. Kutulakos (2007). Photo-Consistent Reconstruction of Semi-transparent Scenes by Density-Sheet Decomposition. *Pattern Analysis and Machine Intelligence, IEEE Transactions on* **29**(5), 870–885. ISSN: 0162-8828.
99. Hata, S., Y. Saitoh, S. Kumamura, and K. Kaida (1996). Shape extraction of transparent object using genetic algorithm. In: *Proceedings of the 13th International Conference on Pattern Recognition, 1996*. Vol. 4, pp.684–688.
100. Henze, I. and G. Stanke (1998). Precise optical measurement of the shape of a class of opaque and transparent objects using special scene structuring. In: *IECON '98. Proceedings of the 24th Annual Conference of the IEEE Industrial Electronics Society, 1998*. Vol. 4, pp.2428–2430.
101. Ihrke, I., B. Goidluecke, and M. Magnor (2005). Reconstructing the geometry of flowing water. In: *ICCV 2005. Tenth IEEE International Conference on Computer Vision, 2005*. Vol. 2, pp.1055–1060.
102. Ihrke, I., K. N. Kutulakos, H. P. A. Lensch, M. Magnor, and W. Heidrich (2008). *State of the Art in Transparent and Specular Object Reconstruction*. EUROGRAPHICS 2008 STAR.
103. Ihrke, I., K. N. Kutulakos, H. P. A. Lensch, M. Magnor, and W. Heidrich (2010). Transparent and Specular Object Reconstruction. *Computer Graphics Forum*. ISSN: 1467-8659.
104. Immel, D. S., M. F. Cohen, and D. P. Greenberg (1986). A Radiosity Method for Non-diffuse Environments. *SIGGRAPH Comput. Graph.* **20**(4), 133–142. ISSN: 0097-8930.
105. Iwasaki, K., F. Yoshimoto, Y. Dobashi, and T. Nishita (2004). A rapid rendering method for caustics arising from refraction by transparent objects. In: *2004 International Conference on Cyberworlds*, pp.39–44.
106. Klank, U., D. Carton, and M. Beetz (2011). Transparent object detection and reconstruction on a mobile platform. In: *Robotics and Automation (ICRA), 2011 IEEE International Conference on*, pp.5971–5978.
107. Košina, J. (2004). *Modelování diamantu pomocí raytracingového programu*. Supervisor: Vladimír Smutný, In Czech. Prague, Czech Republic: Semestral project, Faculty of Electrical Engineering, Czech Technical University in Prague.
108. Košina, J. (2005). "3–D měření výrobků". Supervisor: Vladimír Smutný, In Czech. Master thesis. Prague, Czech Republic: Czech Technical University in Prague.
109. Kutulakos, K. N. and E. Steger (2008). A Theory of Refractive and Specular 3–D Shape by Light-Path Triangulation. *Int. J. Comput. Vision* **76**(1), 13–29. ISSN: 0920-5691.
110. Kutulakos, K. and E. Steger (2005). A theory of refractive and specular 3–D shape by light-path triangulation. In: *ICCV 2005. Tenth IEEE International Conference on Computer Vision, 2005*. Vol. 2, pp.1448–1455.
111. Lambda Research Corporation. *OSLO optical design software* . `http://www.lambdares.com/software%5C_products/oslo/`.
112. Lysenkov, I., V. Eruhimov, and G. R. Bradski (2012). Recognition and Pose Estimation of Rigid Transparent Objects with a Kinect Sensor. In: *Robotics: Science and Systems*.

113. Ma, C., X. Lin, J. Suo, Q. Dai, and G. Wetzstein (2014). Transparent Object Reconstruction via Coded Transport of Intensity. In: *Proceedings of Conference on Computer Vision and Pattern Recognition, CVPR2014*.
114. Ma, L. and Q. Duan (2009). Image-based rendering of transparent object with caustic shadow. In: *YC-ICT '09. IEEE Youth Conference on Information, Computing and Telecommunication, 2009*, pp.538–541.
115. Maltezos, G. and A. Scherer (2011). "Gemstones and methods for controlling the appearance thereof". US Patent 8,069,688. `https://www.google.com/patents/US8069688`.
116. Maltezos, G., A. Scherer, and J. Witzens (2011). "Enhancing the optical characteristics of a gemstone". US Patent 8,033,136. `https://www.google.com/patents/US8033136`.
117. Maltezos, G., A. Scherer, and J. Witzens (2013). "Enhancing the optical characteristics of a gemstone". US Patent 8,479,538. `https://www.google.com/patents/US8479538`.
118. Manabe, Y., M. Tsujita, and K. Chihara (2004). Measurement of shape and refractive index of transparent object. In: *ICPR 2004. Proceedings of the 17th International Conference on Pattern Recognition, 2004*. Vol. 2, pp.843–846.
119. McHenry, K., J. Ponce, and D. Forsyth (2005). Finding glass. In: *CVPR 2005. IEEE Computer Society Conference on Computer Vision and Pattern Recognition, 2005.* Vol. 2, pp.973–979.
120. Meriaudeau, F., R. Rantoson, K. Adal, D. Fofi, and C. Stolz (2012). Non Conventional Imaging Systems for 3D Digitization of Transparent Objects. Shape from polarization in the IR and shape from visible Fluorescence induced UV. In: *3rd International Topical Meeting on Optical Sensing and Artificial Vision: OSAV'2012*.
121. Miyazaki, D. and K. Ikeuchi (2005). Inverse polarization raytracing: estimating surface shapes of transparent objects. In: *CVPR 2005. IEEE Computer Society Conference on Computer Vision and Pattern Recognition, 2005.* Vol. 2, pp.910–917.
122. Miyazaki, D. and K. Ikeuchi (2007). Shape Estimation of Transparent Objects by Using Inverse Polarization Ray Tracing. *Pattern Analysis and Machine Intelligence, IEEE Transactions on* **29**(11), 2018–2030. ISSN: 0162-8828.
123. Miyazaki, D., M. Kagesawa, and K. Ikeuchi (2003). Polarization-based transparent surface modeling from two views. In: *Proceedings of Ninth IEEE International Conference on Computer Vision, 2003*, pp.1381–1386.
124. Modest, M. (2003). *Radiative Heat Transfer*. Elsevier Science. ISBN: 9780080515632. `http://books.google.cz/books?id=VLpjQbjSUCIC`.
125. Morris, N. and K. Kutulakos (2005). Dynamic refraction stereo. In: *ICCV 2005. Tenth IEEE International Conference on Computer Vision, 2005.* Vol. 2, pp.1573–1580.
126. Morris, N. and K. Kutulakos (2007). Reconstructing the Surface of Inhomogeneous Transparent Scenes by Scatter-Trace Photography. In: *IEEE 11th International Conference on Computer Vision, 2007. ICCV 2007*, pp.1–8.
127. Morris, N. and K. Kutulakos (2011). Dynamic Refraction Stereo. *Pattern Analysis and Machine Intelligence, IEEE Transactions on* **33**(8), 1518–1531. ISSN: 0162-8828.

128. Murase, H. (1990). Surface shape reconstruction of an undulating transparent object. In: *Proceedings, Third International Conference on Computer Vision, 1990*, pp.313–317.
129. Murase, H. (1992). Surface shape reconstruction of a nonrigid transport object using refraction and motion. *IEEE Transactions on Pattern Analysis and Machine Intelligence* **14**(10), 1045–1052. ISSN: 0162-8828.
130. Narasimhan, S. and S. Nayar (2003). Contrast restoration of weather degraded images. *IEEE Transactions on Pattern Analysis and Machine Intelligence* **25**(6), 713–724. ISSN: 0162-8828.
131. Narasimhan, S. and S. Nayar (2003). Shedding light on the weather. In: *Proceedings. 2003 IEEE Computer Society Conference on Computer Vision and Pattern Recognition, 2003.* Vol. 1, pp.665–672.
132. Narita, D. and M. Baba (2005). Measurement of 3-D Shape and Refractive Index of a Transparent Object using Laser Rangefinder. In: *IMTC 2005. Proceedings of the IEEE Instrumentation and Measurement Technology Conference, 2005.* Vol. 3, pp.2247–2252.
133. Narita, D. and M. Baba (2006). Measurement of the 3-D Shape and Refractive Index of a Transparent Object by a Laser Rangefinder. In: *International Joint Conference SICE-ICASE, 2006*, pp.1974–1979.
134. Narita, D., M. Baba, and K. Ohtani (2003). Three-dimensional shape measurement of a transparent object using a rangefinding approach. In: *IMTC '03. Proceedings of the 20th IEEE Instrumentation and Measurement Technology Conference, 2003.* Vol. 2, pp.1022–1027.
135. Narita, D., M. Baba, and K. Ohtani (2003). Three-dimensional shape measurement of transparent objects by triangulation approach. In: *SICE 2003 Annual Conference.* Vol. 1, pp.813–817.
136. Nayar, S. and S. Narasimhan (1999). Vision in bad weather. In: *The Proceedings of the Seventh IEEE International Conference on Computer Vision, 1999.* Vol. 2, pp.820–827.
137. Neovision s.r.o. *GlassDrop*. `http://www.neovision.cz/sols/gdrop.html`.
138. Neovision s.r.o. *Helios*. `http://www.neovision.cz/sols/helios.html`.
139. Neovision s.r.o. *MesCut*. `http://www.neovision.cz/sols/mescut.html`.
140. Neovision s.r.o. *SortCut*. `http://www.neovision.cz`.
141. Ni, Y., W. Yu-tian, L. Jiang-tao, and L. Huan-huan (2009). Research on Thickness Measurement of Transparent Object Based on CCD Vision System. In: *ICMTMA '09. International Conference on Measuring Technology and Mechatronics Automation, 2009.* Vol. 1, pp.113–116.
142. Ohara, K., M. Mizukawa, K. Ohba, and K. Taki (2003). 3D modeling of micro transparent object with integrated vision. In: *MFI2003. Proceedings of IEEE International Conference on Multisensor Fusion and Integration for Intelligent Systems,* pp.107–112.
143. Ohara, K., M. Mizukawa, K. Ohba, and T. Tanikawa (2003). How to grasp micro transparent object with integrated vision. In: *IROS 2003. Proceedings. 2003 IEEE/RSJ International Conference on Intelligent Robots and Systems, 2003.* Vol. 2, pp.1889–1894.

144. O'Toole, M., R. Raskar, and K. N. Kutulakos (2012). Primal-dual Coding to Probe Light Transport. *ACM Trans. Graph.* **31**(4), 39:1–39:11. ISSN: 0730-0301.
145. Pohl, P. (2002). "Simulace průletu paprsků transparentním objektem". Supervisor: Vladimír Smutný, In Czech. Master thesis. Prague, Czech Republic: Czech Technical University in Prague.
146. Pottmann, H. and J. Wallner (2001). *Computational Line Geometry*. English. Mathematics and Visualization. Springer Berlin Heidelberg. ISBN: 978-3-642-04017-7.
147. POV-Ray. *Persistance of Vision Raytracer*. http://www.povray.org/.
148. Preciosa a.s. *Fine Jewelery Stones catalogue*. In Czech. http://www.preciosa.com/cs/komponenty/sperkove-kameny/.
149. Preciosa a.s. *Star cut*. http://www.preciosa.com/redakce/index.php?lanG=en&clanek=70&slozka=31&xsekce=60&.
150. Randa, J., N. I. of Standards, and T. (U.S.) (2008). *Recommended Terminology for Microwave Radiometry*. NIST technical note. U.S. Department of Commerce, National Institute of Standards and Technology. http://books.google.cz/books?id=jH3cPgAACAAJ.
151. Rantoson, R., C. Stolz, D. Fofi, and F. Meriaudeau (2012). Optimization of transparent objects digitization from visible fluorescence ultraviolet induced. *Optical Engineering* **51**(3), pages.
152. Reinitz, I., M. Johnson, J. Shigley, and T. Hemphill (2007). "Systems and methods for evaluating the appearance of a gemstone". Patent Nr. US20070083382. US Patent App. 11/515,161. https://www.google.com/patents/US20070083382.
153. Reinitz, I. M., M. L. Johnson, T. S. Hemphill, A. M. Gilbertson, R. H. Geurts, B. D. Green, and J. E. Shigley (2001). Modelling the appearance of the round brilliant cut: An analysis of fire and more about brilliance. *Gems&Gemology* **37**(3). Ed. by G. I. of America, 174–197. ISSN: 0016-626X.
154. Reinitz, I., M. Johnson, J. Shigley, and T. Hemphill (2007). "System and methods for evaluating the appearance of a gemstone". US Patent 7,260,544. https://www.google.com.br/patents/US7260544.
155. Reinitz, I., M. Johnson, J. Shigley, and T. Hemphill (2010). "Systems and methods for evaluating the appearance of a gemstone". US Patent 7,834,987. https://www.google.com/patents/US7834987.
156. Saito, M., Y. Sato, K. Ikeuchi, and H. Kashiwagi (1999). Measurement of surface orientations of transparent objects using polarization in highlight. In: *IEEE Computer Society Conference on Computer Vision and Pattern Recognition, 1999.* Vol. 1, pp.386.
157. Sasian, J., J. Caudill, and P. Yantzer (2008). "Methods, apparatus, and systems for evaluating gemstones". US Patent 7,372,552. https://www.google.com/patents/US7372552.
158. Sasian, J., J. Caudill, and P. Yantzer (2008). "Methods, apparatus, and systems for evaluating gemstones". US Patent 7,420,657. https://www.google.com/patents/US7420657.
159. Sasian, J., J. Caudill, and P. Yantzer (2008). "Methods, apparatus, and systems for evaluating gemstones". US Patent 7,382,445. https://www.google.com/patents/US7382445.

160. Sasian, J., J. Caudill, and P. Yantzer (2008). “Methods, apparatus, and systems for evaluating gemstones”. US Patent 7,336,347. https://www.google.com/patents/US7336347.
161. Schechner, Y., S. Nayar, and P. Belhumeur (2007). Multiplexing for Optimal Lighting. *IEEE Transactions on Pattern Analysis and Machine Intelligence* **29**(8), 1339–1354. ISSN: 0162-8828.
162. Seitz, S. M., Y. Matsushita, and K. N. Kutulakos (2005). A Theory of Inverse Light Transport. In: *ICCV ’05: Proceedings of the Tenth IEEE International Conference on Computer Vision*. Washington, DC, USA: IEEE Computer Society, pp.1440–1447. ISBN: 0-7695-2334-X-02.
163. Sivovolenko, S. (2014). “Method and system for improved optical modeling of gemstones”. US Patent 8,639,479. https://www.google.com/patents/US8639479.
164. Smutný, V. (2011). *Effect of Laser Marking on the Brilliance of Cut Stones*. Research Report K333–44/11, CTU–CMP–2011–07. Prague, Czech Republic: Department of Cybernetics, Faculty of Electrical Engineering Czech Technical University in Prague.
165. Stabo-Eeg, F. (2009). “Development of instrumentation for Mueller matrix ellipsometry”. PhD thesis. Norwegian University of Science and Technology. http://www.diva-portal.org/smash/get/diva2:210447/FULLTEXT02.
166. Steger, E. (2006). “Reconstructing transparent objects by refractive light-path triangulation”. MA thesis. University of Toronto.
167. Szeliski, R. (2011). *Computer vision algorithms and applications*. http://dx.doi.org/10.1007/978-1-84882-935-0.
168. Tan, Z.-M. and P.-F. Hsu (2002). Transient radiative transfer in three-dimensional homogeneous and non-homogeneous participating media. *Journal of Quantitative Spectroscopy and Radiative Transfer* **73**(2-5). Third International Symposium on Radiative Transfer, 181–194. ISSN: 0022-4073.
169. Tarini, M., H. P. Lensch, M. Goesele, and H.-P. Seidel (2005). 3D acquisition of mirroring objects using striped patterns. *Graphical Models* **67**(4), 233–259. ISSN: 1524-0703.
170. Tolkowsky, M. (1919). *Diamond Design, A Study of the Reflection and Refraction of Light in a Diamond*. London: E. & F. N. Spon, Ltd. http://www.folds.net/diamond_design/.
171. Trifonov, B., D. Bradley, and W. Heidrich (2006). Tomographic reconstruction of transparent objects. In: *SIGGRAPH ’06: ACM SIGGRAPH 2006 Sketches*. Boston, Massachusetts: ACM, pp.55. ISBN: 1-59593-364-6.
172. Verboven, M. and T. Blodgett (2013). “Method and system for providing a clarity grade for a gem”. US Patent 8,402,066. https://www.google.com/patents/US8402066.
173. Verboven, M., T. Blodgett, and D. Nuyts (2010). “Automated system and method for clarity measurements and clarity grading”. US Patent App. 12/287,186. https://www.google.com/patents/US20100086179.
174. Wikipedia. *Diamond cut*. http://en.wikipedia.org/wiki/Diamond_cut.
175. Yamazaki, M., S. Iwata, and G. Xu (2007). “Dense 3D Reconstruction of Specular and Transparent Objects Using Stereo Cameras and Phase-Shift Method”. In: *Computer Vision - ACCV 2007*. Ed. by Y. Yagi, S. Kang, I. Kweon, and H.

Zha. Vol. 4844. Lecture Notes in Computer Science. Springer Berlin / Heidelberg, pp.570–579. http://dx.doi.org/10.1007/978-3-540-76390-1%5C_56.
176. ZEMAX Development Corporation. *ZEMAX optical design software*. http://www.zemax.com/.
177. Zygo Corporation. *3–D optical surface profilers*. http://www.zygo.com/?/met/profilers/.